Critical Reviews in Solid State and Materials Sciences, 30:71–124, 2005
Copyright © Taylor and Francis Inc.
ISSN: 1040-8436 print
DOI: 10.1080/10408430590952523

Taylor & Francis
Taylor & Francis Group

Electrical Scanning Probe Microscopy: Investigating the Inner Workings of Electronic and Optoelectronic Devices

S. B. Kuntze*
Edward S. Rogers Sr. Department of Electrical and Computer Engineering at the University of Toronto, 10 King's College Road, Toronto, Ontario, M5S 3G4, Canada

D. Ban
Institute for Microstructural Sciences at the National Research Council of Canada, 1200 Montreal Road, Ottawa, Ontario, K1A OR6, Canada

E. H. Sargent
Edward S. Rogers Sr. Department of Electrical and Computer Engineering at the University of Toronto, 10 King's College Road, Toronto, Ontario, M5S 3G4, Canada

St. J. Dixon-Warren
Chipworks Inc., 3685 Richmond Road, Suite 500, Ottawa, Ontario, K2H 5B7, Canada

J. K. White and K. Hinzer
Bookham Inc., 1-10 Brewer Hunt Way, Kanata, Ontario, K2K 2B5, Canada

Semiconductor electronic and optoelectronic devices such as transistors, lasers, modulators, and detectors are critical to the contemporary computing and communications infrastructure. These devices have been optimized for efficiency in power consumption and speed of response. There are gaps in the detailed understanding of the internal operation of these devices. Experimental electrical and optical methods have allowed comprehensive elaboration of input–output characteristics, but do not give spatially resolved information about currents, carriers, and potentials on the nanometer scale relevant to quantum heterostructure device operation. In response, electrical scanning probe techniques have been developed and deployed to observe experimentally, with nanometric spatial resolution, two-dimensional profiles of the electrical resistance, capacitance, potential, and free carrier distribution, within actively driven devices. Experimental configurations for the most prevalent electrical probing techniques based on atomic force microscopy are illustrated with considerations for practical implementation. Interpretation of the measured quantities are presented and calibrated, demonstrating that internal quantities of device operation can be uncovered. Several application areas are examined: spreading resistance and capacitance characterization of free carriers in III-V device structures; acquisition of electric potential and field distributions of semiconductor lasers, nanocrystals, and thin films; scanning voltage analysis on diode lasers—the direct observation of the internal manifestations of current blocking breakdown in a buried heterostructure laser, the effect of current spreading inside actively biased ridge waveguide lasers, anomalously high series resistance encountered in ridge lasers—as well as in CMOS transistors; and free-carrier measurement of working lasers with scanning differential spreading techniques. Applications to emerging fields of nanotechnology and nanoelectronics are suggested.

Keywords electrical scanning probe microscopy, atomic force microscopy, electrostatic force microscopy, scanning capacitance microscopy, scanning spreading resistance microscopy, scanning voltage microscopy, nanopotentiometry, scanning differential spreading resistance microscopy, scanning probe artifacts, semiconductor characterization, diode lasers, optoelectronic devices, nanocomposite devices, nanocrystals

*E-mail: scott.kuntze@utoronto.ca

INTRODUCTION

Imagine if a medical doctor could probe her patient only through static structural data such as X-ray images. Give her no access to internal information about blood flow, sugar levels, constricted aorta, benign and malignant cells. Permit her to open up the patient, but only in the autopsy once the patient has died from the hitherto unrevealed internal disease. In fact, medicine today relies on techniques such as magnetic resonance imaging (MRI), which produce high-quality images of the inside of the human body at work. This imaging allows three-dimensional mapping of the inside of the human anatomy, probing tissues and tumors without perturbing the patient. Functional MRI, in which the flow of blood, glucose, and so on, can be monitored spatially and in real time, enables imaging of the key inner processes and mechanisms working in concert. Dynamic examination of the living organisms allows doctors to determine the inner origins of externally manifested symptoms.

Nanotechnology is in a state analogous to that of the medical doctor prior to the development of a host of functional imaging techniques. Insight into the inner functioning and malfunctioning of the patient—be it a multi-quantum-well laser, a resonant tunneling transistor, or a hybrid quantum dot-conducting polymer device—has come through external outputs (e.g., light–current–voltage), static structural information through destructive techniques (e.g., transmission electron microscopy image of a cut and lapped device), and incompletely validated theoretical models.

Realizing fully the vision of engineering physics-into-function demands new experimental means by which to nanoscopically probe the internal behaviors of devices in active operation. This work is motivated by the need to probe the internal behavior of active nanodevices, such as the high-performance semiconductor laser devices required by the new generation of optical communication systems. Until recently, attempts at characterizing such devices were mainly related to static structural information or input–output behaviors and were limited in scope. Internal phenomena and external performance measures were seldom linked through compelling experimental observation. Many failures and degradations of device operation remained puzzling as a result. For example, a lack of direct quantitative profiling of carriers within the active region of operating lasers impeded understanding of the underlying mechanisms for degraded efficiency and increased threshold current.

The present review connects internal mechanisms with external measurements in nanophotonic devices. It aims to demonstrate and evaluate enabling tools for research and development in quantum microscopic and nanoscopic physics. The article describes work that depends on a range of atomic force microscopy (AFM) techniques for the characterization of actively driven nanostructure-based devices. These tools allow us to answer critically important questions regarding the internal origins of the observed performance. With these tools, the key inner workings inside operating nanodevices—potential profiles and carrier densities—are measured on the nanometer scale. These results, in combination with external performance measurements, connect structural physics with functional performance in nanostructures, opening up possibilities of engineering novel materials and devices with unprecedented properties.

The article begins by reviewing the operation of the atomic force microscope in the next section. Selection of conductive probes for electronic measurement is considered in the third section. Advances in quantitative dopant profiling through single-probe scanning spreading resistance microscopy (SSRM) are reviewed in the fourth section. The fifth and sixth sections examine the closely related electrostatic force (EFM) and scanning capacitance microscopies (SCM) in which no contact is made between the conductive probe and sample; a wealth of internal data can be obtained. The seventh through the tenth sections review progress in scanning voltage microscopy (SVM) through its operating principles, application to transistor characterization, application to diode laser characterization, and identification of sources of artifact, respectively. A hybrid technique, scanning differential spreading resistance microscopy (SDSRM), is described in the eleventh section. The twelfth section looks forward to the application of various AFM techniques to nanoscale electronics and photonics. Finally, the last section compares each technique reviewed in terms of function and performance, and summarizes the authors' findings.

ATOMIC FORCE MICROSCOPY

With the invention of atomic force microscopy (AFM) in 1986 by Binnig, Quate, and Geber[1] a means of probing devices was provided with spatial resolution commensurable with the ever-shrinking micron and sub-micron feature sizes (Binnig won the Nobel prize in 1986 for the earlier invention of the scanning tunneling microscope). Two aspects make AFM ideally suited for electron and optoelectronic device characterization: first, AFM works well from the atomic scale through to tens or hundreds of micrometers; second, AFM can be adapted in many different ways depending on the desired measured quantity, as the following survey will show.

AFM employs three-dimensional piezo-mechanical drivers to achieve precise sub-nanometer positioning in all directions. The drivers hold micromachined cantilevers with pyramidal probe tips at the very end, as illustrated schematically in Figure 1. A laser beam is reflected off the end of the cantilever and is detected by a grid of photodetectors; by means of this "optical lever" small deflections of the probe tips are tracked by relatively large deflections of the laser on the detector array. A feedback loop allows accurate control of the tip, either by moving the sample or the probe. Additionally, an optical microscope aids coarse positioning of the tip. Data is captured by onboard electronics and is sent to collection and processing software.

Deflection of the tip can be caused by friction, surface interactions, noncontact electrostatic or electrodynamic interactions. In *contact mode*, the tip is simply dragged across the sample

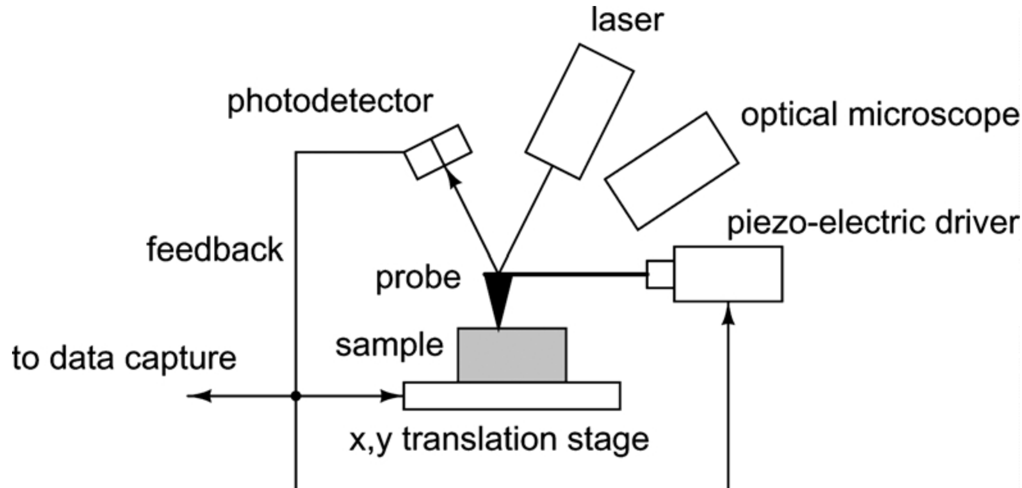

FIG. 1. Schematic of the atomic force microscope.

surface at a known and fixed tip–sample force. Alternatively, the tip may be floated or tapped across the surface at a known oscillation frequency and deviations to this frequency interpreted as sample-induced interactions. In these *noncontact modes*, scanning techniques may be less destructive or even entirely nondestructive to the sample. Tip deflections as small as ∼10 pm or as large as ∼100 nm can be detected routinely, providing great dynamic range unobtainable by tunneling current methods.[2]

AFM on its own can be used to characterize semiconductor devices beyond simple topographic mapping. For example, selective chemical etching can be used[3] to remove materials of certain composition or doping concentration and the resulting topography can be measured by AFM, from which the doping and composition is inferred over the device surface.

Augmenting the basic AFM with electronic characterization capability greatly expands the range of observable device parameters. For example, experimental and theoretical investigations on ridge waveguide (RWG) and buried heterostructure (BH) lasers provide vast amounts of information about laser performance, operation, and their controlling factors; however, the understanding of the internal behavior of these devices is insufficient in many cases. Many internal physical phenomena, including the current spreading effect, the impact of different barrier layer bandgaps, the effects of interfaces or heterobarriers, current leakage, and nonuniform carrier distribution, are difficult to observe via direct experiments. This lack of direct observation prevents conclusive identification of the key mechanisms responsible for performance degradation or improvement. The internal operating parameters are required in two dimensions to delineate quantitatively the cross-sectional electronic structure of operating complex two-dimensional devices such as buried heterostructure multi-quantum-well (MQW) lasers. Scanning probe microscopy (SPM), which includes atomic force microscopy and related AFM-based techniques, provides spatial resolution on the nanometer scale and therefore holds the best chance of meeting all the challenges.

CONDUCTIVE PROBE SELECTION

Probe selection is important for electrical AFM techniques. Monocrystalline chemical vapor deposited (CVD) diamond tips for scanning tunneling microscopy (STM) were first fabricated in 1992.[4] Prior to that, thin platinum–iridium or tungsten wires were pulled and clipped to produce atomically sharp conductive needles (Pt/Ir and W tips are still used in STM applications). However, such a process produces a tip of random geometry (one hopes for an atomic point) that may contain extra protrusions that cause imaging artifacts. For example, a tip with two protrusions of similar height will produce double images when scanning a small, singular object—one image for the pass of each tip. Other tip-induced artifacts may not be so easy to identify. Polished diamonds of known shape could also be made conductive by ion-implantation doping. Diamond is ideal for electrical contact AFM because it is both very hard and chemically inert (i.e., it does not oxidize).[4]

In their first realization,[4] CVD diamond tips were grown epitaxially on (110) diamond seed layers, grown to layer thicknesses of some 5 μm and doped with boron to impurity concentrations of 6×10^{20} cm^{-3}. The tips were then polished to fine points. Resistivity varied from $\sim 10^{-4}$ $\Omega \cdot$m at room temperature to ~ 5 $\Omega \cdot$m at 4.2 K.

Electronic transport properties of CVD diamond and boron-doped CVD diamond have been well characterized.[5–10] Electron and hole mobilities are each on the order of 10^3 cm$^2/(\mathrm{V} \cdot \mathrm{s})$.[5] CVD diamond may have a *negative* electron affinity depending on orientation and surface termination, placing its conduction band *above* the vacuum energy level.[6] Its bandgap is 5.5 eV.[7] Hydrogen-terminated (100) and (111) surfaces have a

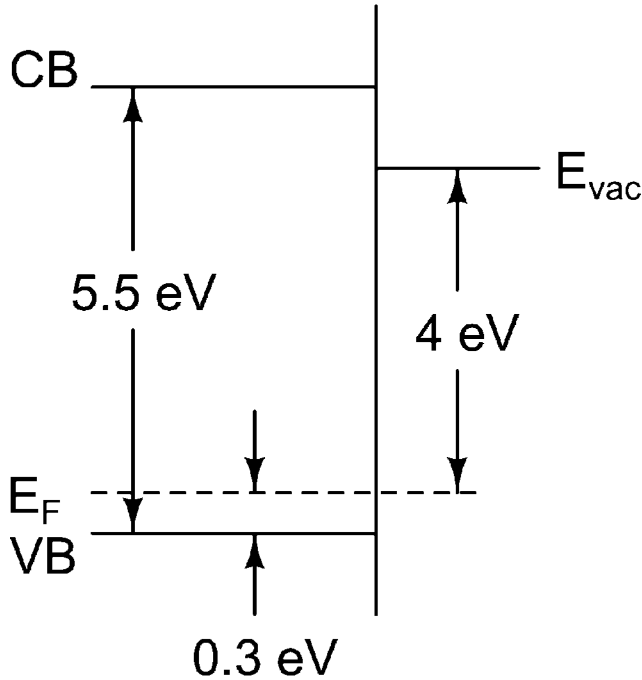

FIG. 2. Band structure for H-terminated B-doped CVD diamond (100) and (111).[7] The electron affinity is negative, placing the conduction band above the vacuum level and giving rise to a work function that is less than the bandgap.

work function of ∼4 eV;[7,10] a typical band structure is plotted in Figure 2 for a boron concentration of 10^{16} cm^{-3}. Because the conduction band is energetically far from the valence band and Fermi level, heavily boron-doped CVD diamond films may be modeled as a metal.[8]

CVD diamond is grown on silicon cantilevers[11] with spring constants ranging from 0.1 to 100 N/m,[12] suitable for tip–sample forces on the order of micronewtons.[11] Cantilevers are produced en masse in wafers by a combination of anisotropic etching and micromachining followed by diamond film deposition.[12]

Various tips have been characterized for use in electrical contact-mode operation.[11,13–15] Trenkler and coworkers systematically evaluated nanoscopic boron-doped CVD diamond-coated silicon tips[11,13,14] for use in SSRM and SVM; these tips consistently outperformed metallic, doped silicon, and ion-implanted solid diamond tips, both in terms of electrical and mechanical properties. For example, solid diamond tips were found to be too bulky mechanically,[11] whereas metallic and silicon tips failed to track a simple square wave input.[14] Comparison of triangular and rectangular cantilevers shows that rectangular cantilevers are mechanically more robust.[16]

A wide variety of probes are now commercially available for scanning probe measurements. SSRM and SCM require the use of conductive probes with good material hardness and electrical conductivity. Previously reported results on III–V compound semiconductor samples[17] revealed that the probes that yield the best quantitative correlation between SSRM and SCM measurements and secondary ion mass spectrometry (SIMS) results are commercially available boron-doped (p-type) diamond-coated cantilever tips (Digital Instruments, spring constant = 40 N/m). Figure 3 shows a scanning electron microscope (SEM) image of a probe of this type. One can observe the sharpness of the tip point of this probe: its radius is normally below 10 nm.

The short 125 μm cantilever probes with a 320 kHz resonant frequency and a 42 N/m force constant give the best results. Typically the diamond-coated probe can last for several hours to several days of measurements before the probe becomes unacceptable. Best results (highest sensitivity and finest spatial resolution) are obtained by using a fresh probe. In the authors' experience, the conductive layer of CVD tips tends to fail catastrophically at very high sample biases due to direct heating from the sample surface being scanned.

SCANNING SPREADING RESISTANCE MICROSCOPY

In scanning spreading resistance microscopy (SSRM), the electrical resistance is measured between the conductive probe tip and a current-collecting back contact while the probe is scanned in contact mode across the cross-section of the semiconductor device under test. The measured resistance is in principle inversely proportional to the local carrier concentration underneath the probe–device contact point. The measurement thereby yields a profile in two dimensions of the local carrier density.

Principles of Operation

In typical SSRM, a known voltage is placed across the grounded sample from probe tip to ground and the resulting current is measured—the ratio gives the spreading resistance. The schematic of SSRM is shown in Figure 4.

In practice, a sensitive six-decade (1 mA–1 nA) logarithmic amplifier is used to measure the electric current flowing from the tip through the sample and to the sample chuck as a function of the AFM tip position. The SSRM measurements are performed under contact mode AFM feedback conditions. The tip is scanned at 0.25–4 μm/s with forces in the range of 2–5 μN. The applied force enables the tip to penetrate insulating native oxide layers at the semiconductor surface. The applied DC bias between the probe and the sample is varied from +0.5 to 3.5 V.

Because the sample is grounded, the carrier concentration and doping level at each scan location can be inferred. According to Ohm's law, the measured current I is given by

$$I = \frac{V}{R} = V(4\sigma a) = 4Vqa(n\mu) \propto n\mu, \qquad [1]$$

where $R = 1/(4\sigma a)$ is the spreading resistance, $\sigma = qn\mu$, is the local conductivity, a is the radius of the probe, n is the local free carrier concentration, and μ is the carrier mobility. Equation 1 shows the measured current is proportional to the local carrier

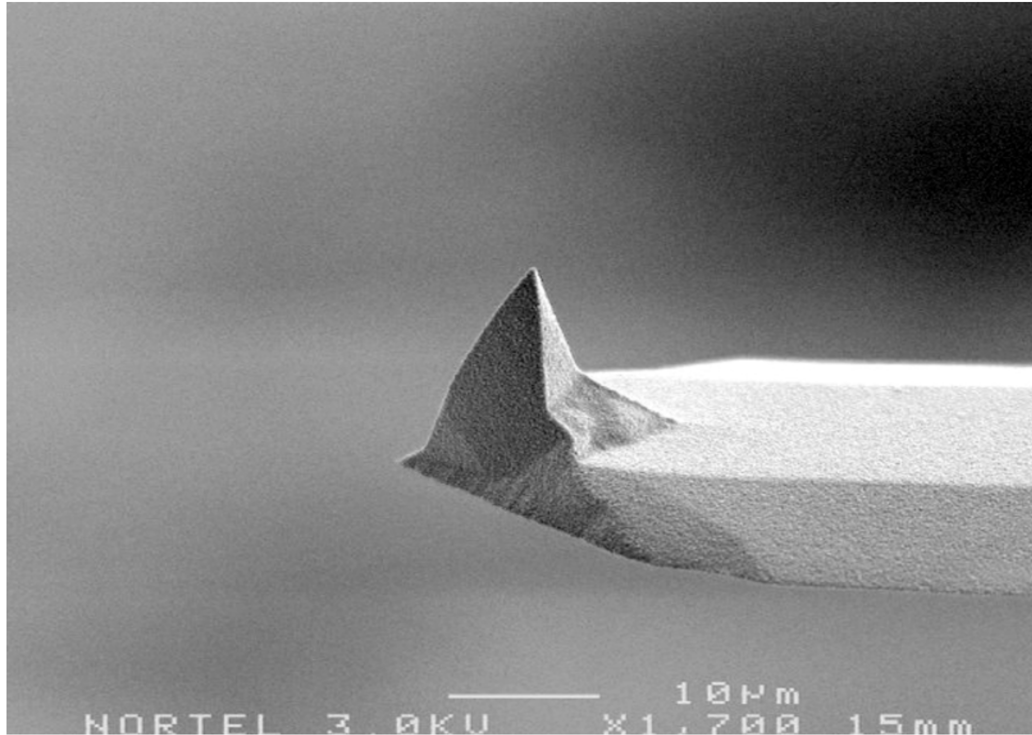

FIG. 3. Scanning electron microscope image of a conductive diamond-coated silicon probe.

density and the mobility. Variations in the tip-surface contact resistance must also be considered in certain circumstances.[18]

Because spreading resistance is a compound quantity, calibration is required. SSRM data for doped InP has been correlated to trusted SIMS data and calibration curves have been produced.[19–22] Exhaustive calibration on InP and GaAs of typical optoelectronic device n- and p-type doping concentrations was performed to SIMS data,[18,23] along with interface analysis. A Schottky barrier model was fitted to the tip–sample interface with CVD diamond tips on these III–V semiconductors.

SSRM of III–V Semiconductor Laser Diodes

Scanning spreading resistance microscopy was used to examine the cross-section of a buried heterostructure (BH) multi-quantum-well (MQW) laser structure. BH diode lasers used for these SSRM experiments were grown by organic chemical vapor deposition (MOCVD). The mesa of the BH laser is buried by a four layer thyristor structure with alternating doping type (n- or p-doped) and concentration. The quantum wells are separated by barrier layers. BH laser samples are metallized with ohmic contacts and then mounted with the cleaved edges facing upward.

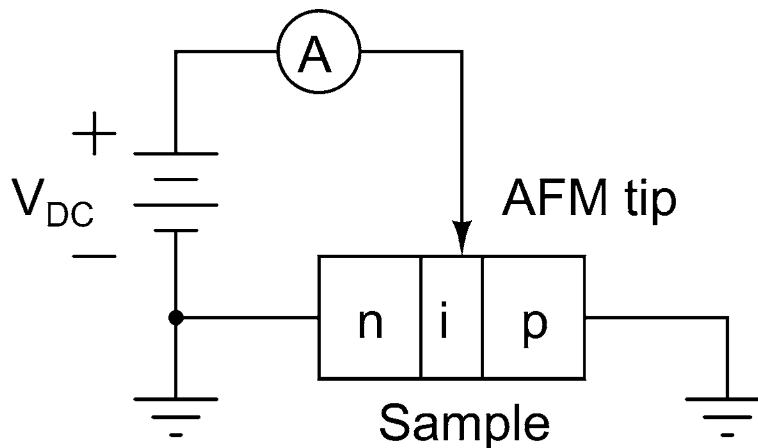

FIG. 4. Schematic of SSRM circuit.

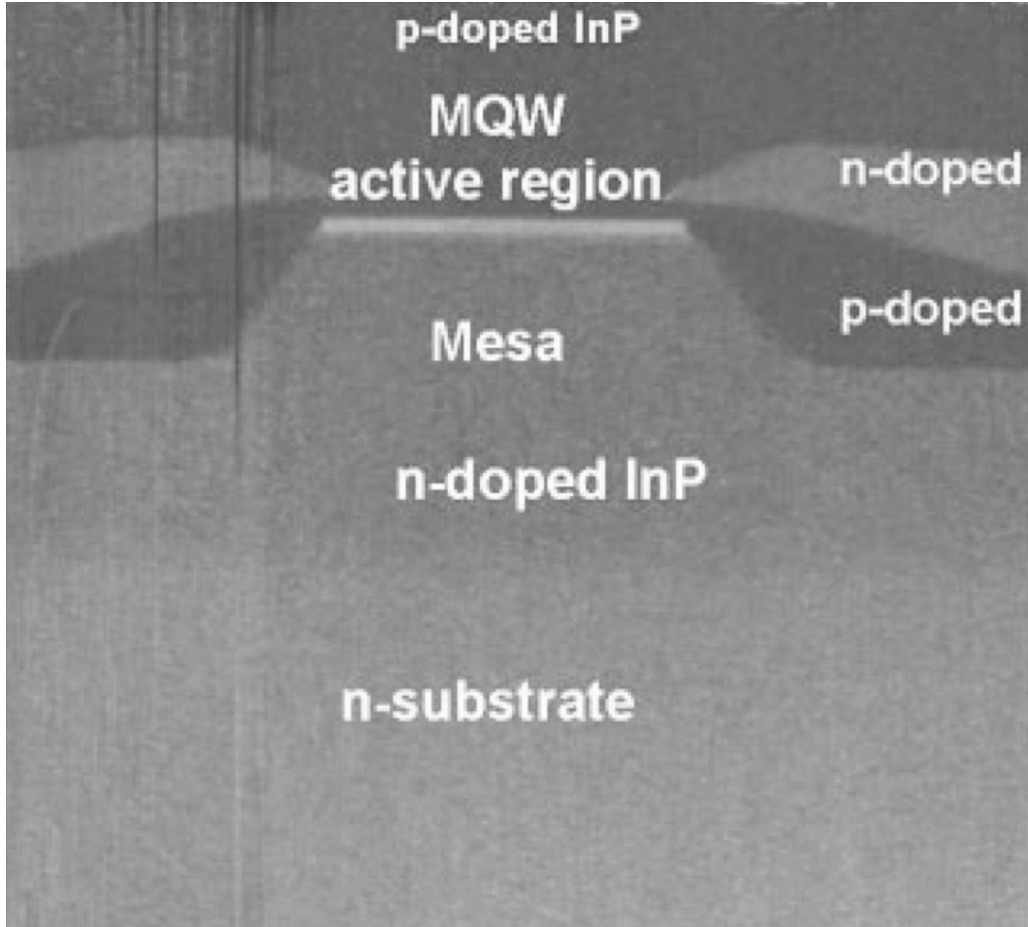

FIG. 5. SSRM image of buried heterostructure MQW laser in cross section. Tip bias was 0.5 V and the scan rate was 0.25 Hz. MQW active region (bright, narrow bar near the center of the image) is clad by p-doped (top) and n-doped (bottom) material. The image is approximately 5×5 μm. (Reprinted with permission from Ref. 24, Copyright 2002, AVS The Science & Technology Society.)

Figure 5 shows a typical SSRM current image obtained on the uncoated facet of the laser device. The bias voltage was 0.5 V and the tip scan rate was 0.25 Hz. The n^+ substrate is the bright region at the bottom. The buried mesa structure is clearly resolved in the SSRM image. The narrow, bright strip around the center of the image is the MQW active region, which is clad by p- and n-doped layers above and below it. Individual quantum well–barrier periods can be resolved by slowing down the SSRM scan. At the left and right sides of the active region are the symmetric p–n–p–n current blocking structures. A topographic AFM image of the BH laser, obtained simultaneously with the SSRM data, showed no perceptible features during the scan. Neglecting any dependence of tip-to-sample contact resistance on tip position, the measured current is expected to be proportional to $n\mu$, the product of local carrier concentration and mobility.

This SSRM image, Figure 5, may be compared with the known nominal carrier density of the p–n–p–n thyristor structure of the BH laser. The first layer (p-doped) at the top has a higher doping concentration than the third layer (also p-doped), and therefore is brighter in contrast (higher current under the same DC bias voltage). Similar contrast can be observed between the second (n-type, lower doping concentration) and the fourth (n-type substrate, higher doping concentration) layers.

Figure 6a shows a high-resolution SSRM image of the transverse cross-section of the MQW active region. Shown in the inset is a transmission electron microscope image of the quantum well region (lateral cross section). Tip bias was 0.5 V and the scan rate was 0.25 Hz. Individual quantum wells and barriers are resolved in the SSRM image. The intrinsic active quantum well region of the device appears to be brighter than both the n-doped region (below) and p-doped region (above). This effect has been attributed[17] to the smaller bandgap, higher intrinsic carrier concentration, and higher carrier mobility of the InGaAsP quantum wells that make up the active region.

Figure 6b shows the SSRM current, measured at a DC tip bias voltage of 0.5 V, as a function of depth below the device surface.

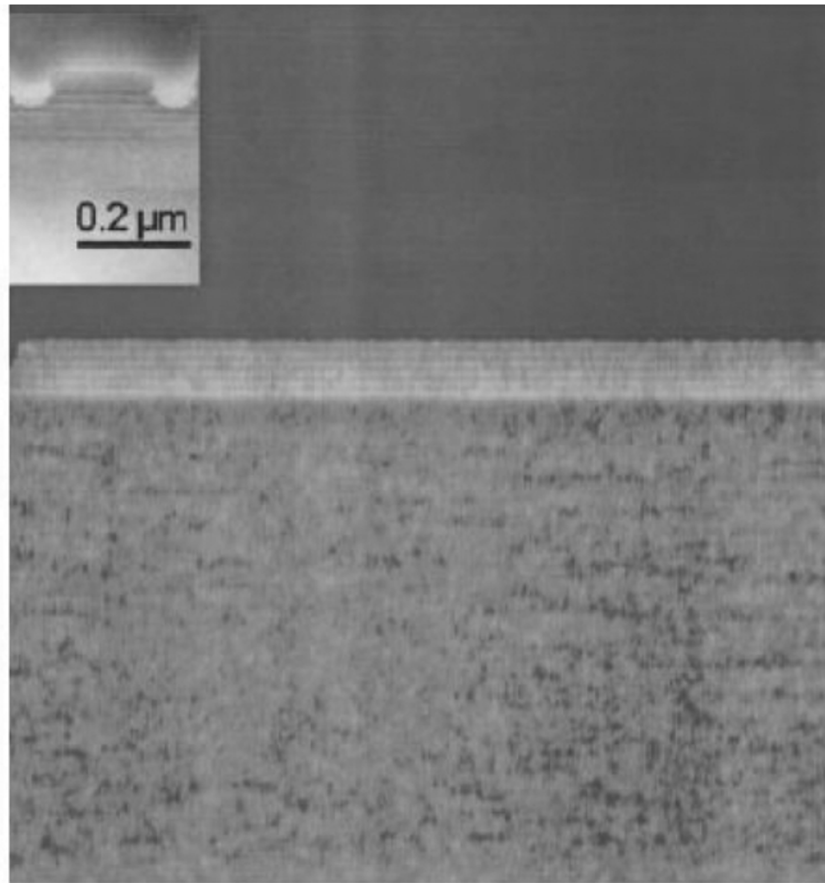

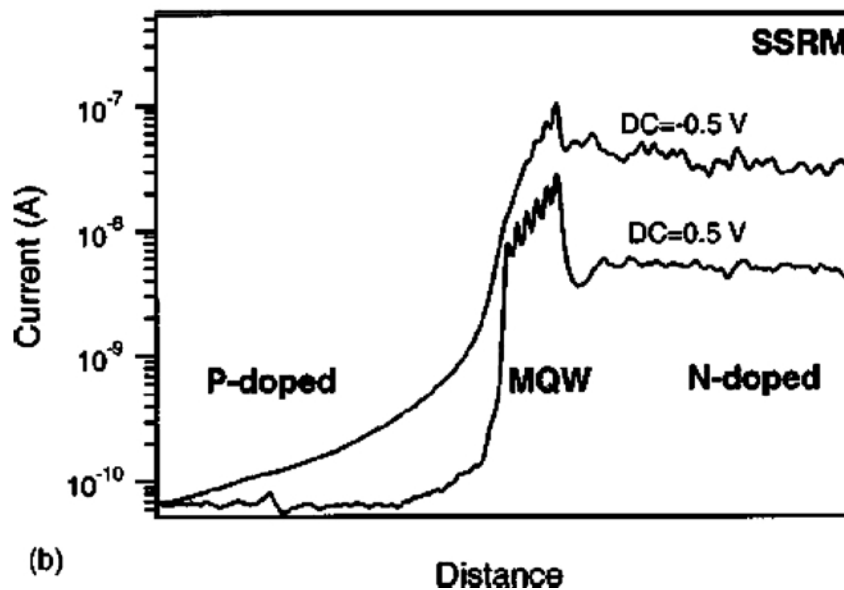

FIG. 6. (a) High-resolution SSRM image showing the quantum well structure in the active region of the BH laser. A single quantum-well–barrier period is resolved. The tip bias was 0.5 V and the scan rate was 0.25 Hz. A transmission electron microscope image of the quantum-well region is also shown in the inset. The image is approximately 1.5×1.5 μm. (b) Cross-sectional SSRM current at DC bias voltages of +0.5 and −0.5 V throughout the MQW region. (Reprinted with permission from Ref. 25, Copyright 2002, AVS The Science & Technology Society.)

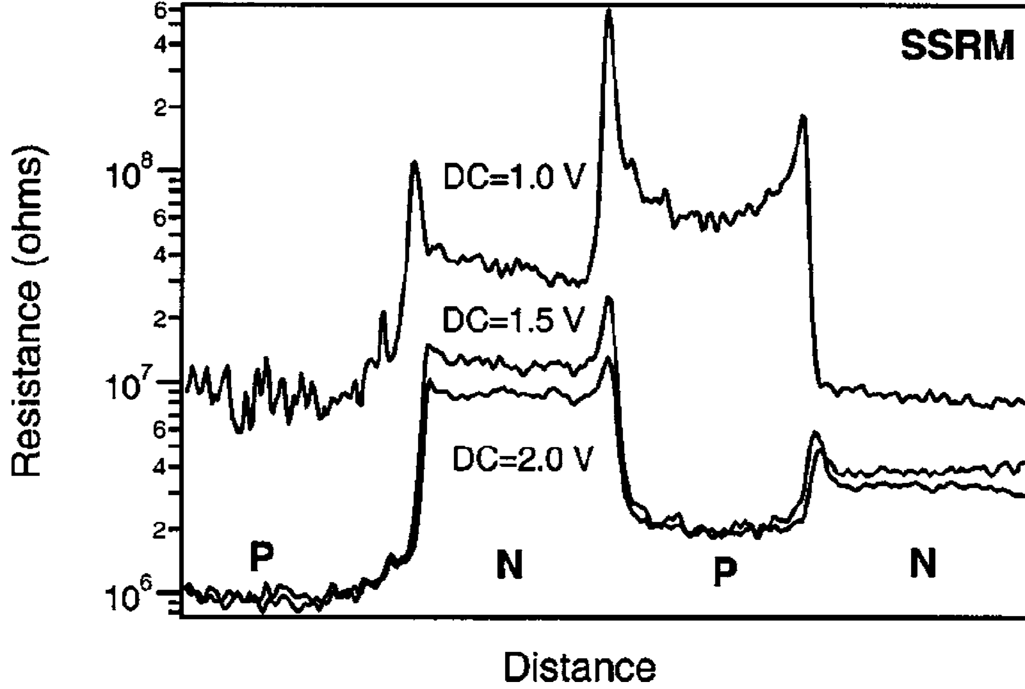

FIG. 7. Cross-sectional SSRM resistance of the *p–n–p–n* current-blocking structure of a BH laser device. The tip bias is shown on the graph for each curve; the scan rate was 0.5 Hz. (Reprinted with permission from Ref. 25, Copyright 2002, AVS The Science & Technology Society.)

The cross-sectional curve is obtained by averaging the line scans that make up Figure 6a. Also shown is the current obtained at a reverse bias of −0.5 V. Strong contrast in SSRM current among quantum wells and barrier layers is obtained only at forward DC bias (0.5 V), indicating a strongly nonlinear dependence of the SSRM current on the sample bias.[17] An upward slope in the SSRM current in the active region can be observed in both curves; this behavior may be a consequence of the potential drop in the MQW active region (up to around 1 V) due to the built-in electrical field across the *p–i–n* junction.

Figure 7 shows the averaged spreading resistance as a function of depth below the device surface in the *p–n–p–n* structure region. The SSRM resistance profile is measured at three DC bias voltages. The measured resistance of every region decreases as the DC bias increases from 1.0 V to 2.0 V in 0.5 V increments, indicating a bias-dependence to the SSRM resistance. The effect is attributable to the establishment of a Schottky contact between the probe tip and sample surface.[18]

SSRM results also shed light on the characteristics of the depletion region formed at *p–n* junctions. The depletion regions are expected to have lower conductivity, resulting in the peaks in the SSRM resistance profiles of Figure 7. The expected width of the depletion region is approximated by:

$$W = \left[\frac{2\epsilon_r\epsilon_0 k_B T}{q^2}\ln\left(\frac{N_a N_d}{n_i^2}\right)\left(\frac{N_a + N_d}{N_a N_d}\right)\right], \qquad [2]$$

where $\epsilon_r = 12.56$ for InP, ϵ_0 is permittivity of free space, q is the electronic charge, k_B is Boltzmann's constant, T is the temperature, and n_i is the intrinsic carrier concentration, which for InP at 300 K is 1.2×10^8 cm^{-3}. N_a and N_d are the donor and acceptor concentrations of the materials making up the *p–n* junction. The depletion region width at the *p–n* junction between the second and third layers from the top of Figure 7 is 70 nm. This result agrees well with the calculated value $W = 66$ nm using the known nominal doping concentrations $N_d = 1 \times 10^{18}$ cm^{-3} and $N_a = 6 \times 10^{17}$ cm^{-3}.

Averaged SSRM resistances at each blocking layer of the *p–n–p–n* structure, taken from the mean value of the resistance curve in each corresponding region of Figure 7, ranges from 1×10^6 to 6×10^7 Ω, depending on the DC bias voltage and the local carrier density. These measured resistances, correlated with the SIMS calibration curves (Figure 8), can be used to derive the local carrier density of each doped layer in the *p–n–p–n* structure for a given SSRM bias.

ELECTROSTATIC AND KELVIN PROBE FORCE MICROSCOPY

Electrostatic force microscopy (EFM) was first presented in 1987 by IBM researchers Martin, Williams, and Wickramasinghe.[2] They used optical heterodyne detection to measure frequency changes in a vibrating AFM probe cantilever caused by normal electric field components of surface charges and potentials. Knowing the spring constant and geometry of

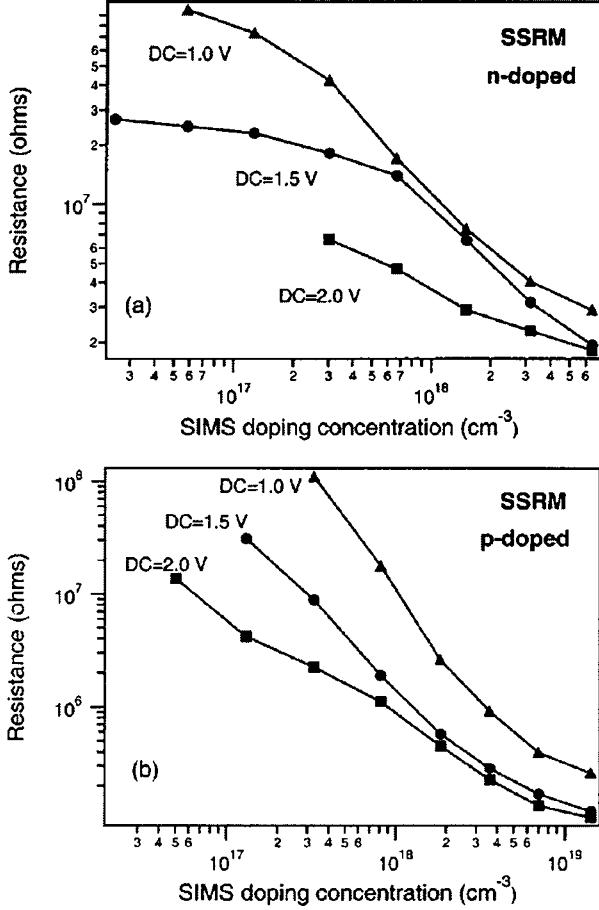

FIG. 8. SSRM resistance vs. SIMS dopant concentration for Si-doped (a) and Be-doped (b) InP epitaxial layers separated by undoped InP and grown by MBE on an n^+-InP substrate. Calibration measurements were performed at three DC bias voltages: 1.0, 1.5, and 2.0 V. (Reprinted with permission from Ref. 25, Copyright 2002, AVS The Science & Technology Society.)

the cantilever, the gradient of the probe tip–sample force can be induced as a function of the tip–sample distance, and the absolute force derived.[2] It is possible to derive capacitance and electric potential from the force gradient,[26] expanding AFM into the realm of electronic measurement. Surface charge can also be recovered[27] with a sensitivity of tenths of a unit electron charge.[28]

EFM Principles of Operation and Interpretation

The electrostatic force between the AFM tip and the sample separated by a distance z is given by Ref. 29

$$F = \frac{1}{2}\frac{dC}{dz}V^2, \qquad [3]$$

where C is the tip–sample capacitance and V is the total voltage difference. This voltage can be decomposed into a sum of the contact potential V_{cp}, the induced voltage V_{ind} related to the local sample potential, and the DC and AC voltages applied to the tip, V_{dc} and $V_{ac}\sin\omega t$, respectively.[29] Writing $V_{stat} = V_{cp}+V_{ind}+V_{dc}$ as the total static potential, the force can be written

$$F = \frac{1}{2}\frac{\partial C}{\partial z}\left(V_{stat}^2 + 2V_{stat}V_{ac}\sin\omega t + V_{ac}^2\sin^2\omega t\right) \qquad [4a]$$

$$= \frac{1}{2}\frac{\partial C}{\partial z}\left[V_{stat}^2 + 2V_{stat}V_{ac}\sin\omega t + V_{ac}^2\left(\frac{1}{2} - \frac{1}{2}\cos 2\omega t\right)\right] \qquad [4b]$$

from which the DC force component can be easily extracted,

$$F_{dc} = \frac{1}{2}\frac{\partial C}{\partial z}\left(V_{stat}^2 + \frac{1}{2}V_{ac}^2\right), \qquad [5]$$

the first harmonic,

$$F_\omega = \frac{\partial C}{\partial z}V_{stat}V_{ac}\sin\omega t, \qquad [6]$$

and the second harmonic,

$$F_{2\omega} = -\frac{1}{4}\frac{\partial C}{\partial z}V_{ac}\cos 2\omega t. \qquad [7]$$

The first harmonic F_ω is linear in the sample voltages V_{cp} and V_{ind} and so sample voltage profiles can be obtained at a fixed scan distance z using a lock-in amplifier at ω.[29] Furthermore, a closed-loop controller can be incorporated to keep $F_\omega = 0$ by setting V_{dc} such that $V_{dc} = -(V_{cp} + V_{ind})$, and changes in V_{cp} or V_{ind} can be detected in the error signal of the controller; this mode of operation is called Kelvin operation[29] or Kelvin probe force microscopy (KPFM). Surface charge Q present on the sample can be extracted by replacing sample voltage term V_{ind} with a Coulombic term,[29]

$$F_\omega = \left[\frac{\partial C}{\partial z}(V_{cp} + V_{dc}) - \frac{QC}{4\pi\epsilon_0 z^2}\right]V_{ac}\sin\omega t, \qquad [8]$$

and the sign and magnitude of Q can be determined at a given scan location.

The second harmonic $F_{2\omega}$ given by Eq. 7 is linear in the capacitive coupling $\partial C/\partial z$ so variation in the sample dielectric constant (C is a function of ϵ) can be imaged at a fixed scan distance[26,28] using a lock-in amplifier at the frequency 2ω.

Maintaining constant tip–sample distance is realized by either single-pass or double-pass scans. In single-pass, the tip is operated in the Kelvin mode [29] where the force is kept at zero and topological images are obtained through the force controller error signal; Kelvin operation ensures that the DC forces on the tip are suppressed and constant tip–sample distance is maintained. In double-pass, two scan lines over the same sample region are acquired. The first pass is performed in AFM tapping mode to obtain the physical topology of the surface. During the second pass, the tip is retracted and driven into oscillation. Changes in the force due to voltages or charges can be isolated by comparison with the topological image.

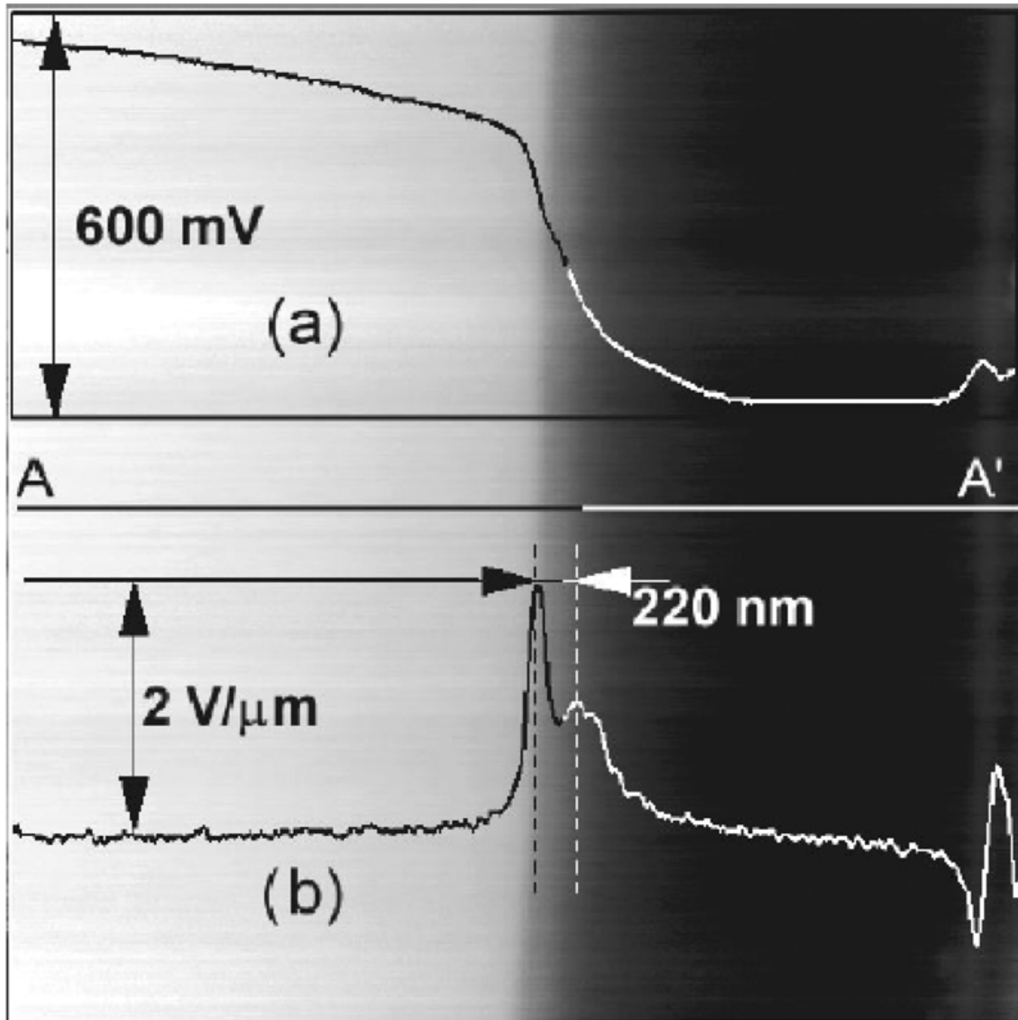

FIG. 9. Electric potential (a) and field (b) obtained across a laser diode at equilibrium (*n* on the left, *p* on the right). (Reprinted with permission from Ref. 30, Copyright 2000, American Institute of Physics.)

EFM on Semiconductor Laser Diodes

Using the Kelvin operational mode, EFM was used to measure potential and field profiles of InP/InGaAsP laser diodes.[30] A laser sample was oriented light-emitting facet upward for easy exposure to the tip. The actual laser structure studied was grown entirely by MOCVD and consisted of *n*- and *p*-type InP layers (nominal doping 10^{-18} cm^{-3}) cladding a single-layer InGaAsP active region 220 nm thick. A two-dimensional potential scan captured over the light-emitting facet at constant tip height (double-pass) is shown in Figure 9 with one-dimensional potential and field profiles superimposed. The built-in profile from *n* (left) to *p* (right) drops 0.6 V, which is roughly half the theoretical drop from simulation; surface states of the native oxide were found to be the cause of disagreement and good agreement was obtained after updating the simulation with surface effect corrections.[30] The electric field profile exhibits a peak active region field of 2 MV/m.

Analysis of biased GaAlSbAs mid-infrared (2.36 μm) diode lasers featuring 7-nm-wide quantum wells employed a similar configuration.[31] A heavily doped silicon tip 20 nm wide at the apex allowed 50 nm spatial resolution. In Figure 10, the measured EFM potential is plotted for reverse and forward bias (*n* is on the left, *p* on the right). The active region appears between the cladding regions but due to the coarse spatial resolution the quantum wells are invisible.

The power of EFM as a diagnostic tool is evident from the analysis of failure conditions of a InAs/AlSb/GaSb quantum cascade laser.[32,33] An otherwise healthy laser exhibited a sudden and drastic decrease in series resistance as the bias voltage was increased, leading to a current surge and loss of light emission. By scanning over the actively biased laser, a sharp potential drop at the edge of an active region was observed above breakdown bias voltages, illuminating the source of current surge and informing the next iteration of design.

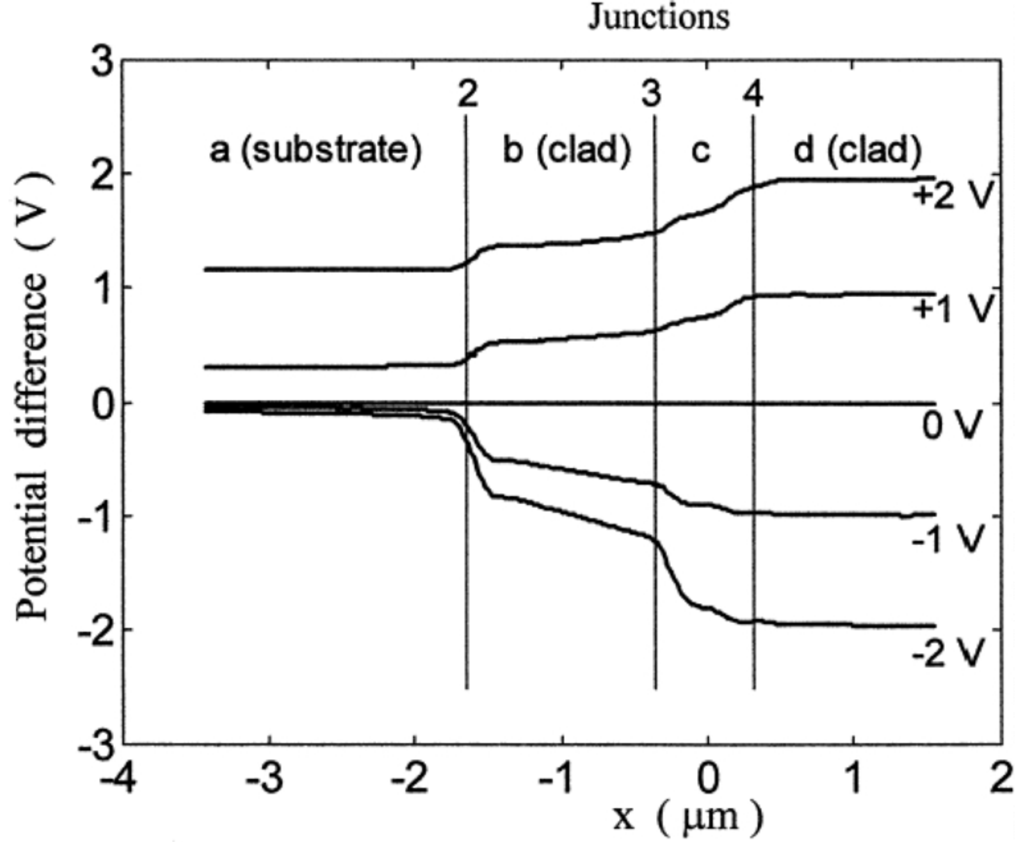

FIG. 10. Electric potential traces across an actively biased laser diode for various bias points (n on the left, p on the right with the active region between lines 3 and 4). (Reprinted from Ref. 31, Copyright 2000, with permission from Elsevier.)

EFM on Individual Semiconductor Nanocrystals

Semiconductor nanocrystals are nanometer-sized crystalline collections of approximately 100 atoms. Their shape is roughly spherical and their sizes range from 2 nm to 50 nm. They have attracted great interest over the last decade because they offer three-dimensional quantum confinement that can be exploited in optical, electronic, and optoelectronic applications.

It is critical to understand the charge and electric field structure of individual nanocrystals because they influence oscillator strength, carrier lifetimes, electron–phonon coupling, and capacitance,[28] and understanding these properties enables design of nanocrystal-based devices. For example, photoluminescent spontaneous blinking of nanocrystals has been observed and is attributed to nanocrystal charging and discharging; charged nanocrystals may inhibit carrier injection in optoelectronic applications.[34]

The first application of EFM to the study of individual nanocrystals examined CdSe nanocrystals with diameter ∼5 nm.[28] CdSe nanocrystals encapsulated with trioctylphosphine oxide were deposited onto an insulating layer above a conductive substrate. Image charges appearing in the substrate and tip due to the presence of the sample charge Q can be incorporated into Eq. 8, yielding[28]

$$F_{\omega} = \left(\frac{\partial C}{\partial z}(V_{\mathrm{dc}} + V_{\mathrm{cp}}) + \frac{QC}{4\pi \epsilon_0 z^2} + \frac{Q_1 C}{4\pi \epsilon_0 (z + 2h/\epsilon_1)^2} + \frac{\partial C}{\partial z}\frac{Q_2}{C} \right) V_{\mathrm{ac}}, \quad [9]$$

where Q_1 and ϵ_1 are the image charge and dielectric constant of the substrate, respectively, and Q_2 is the image charge appearing in the tip; h is the thickness of the insulating layer.

Because the slow-scan occurs over a period of time, it provides a time-evolution image. Remarkably, the nanocrystal in Figure 11a turns off (blinks) halfway down the F_{ω} scan, indicating spontaneous charging. The nanocrystal is still present below the turn-off point as can be seen in the dielectric constant image ($F_{2\omega}$) of Figure 11b. As detected by EFM, the bright top portion of the image corresponds to a positive charge that is neutralized in the bottom portion, likely from thermal charge transfer of an electron to the nanocrystal.[28,35]

The CdSe nanocrystals were photoexcited with laser light above their bandgap. Figure 12 shows before (left) and after

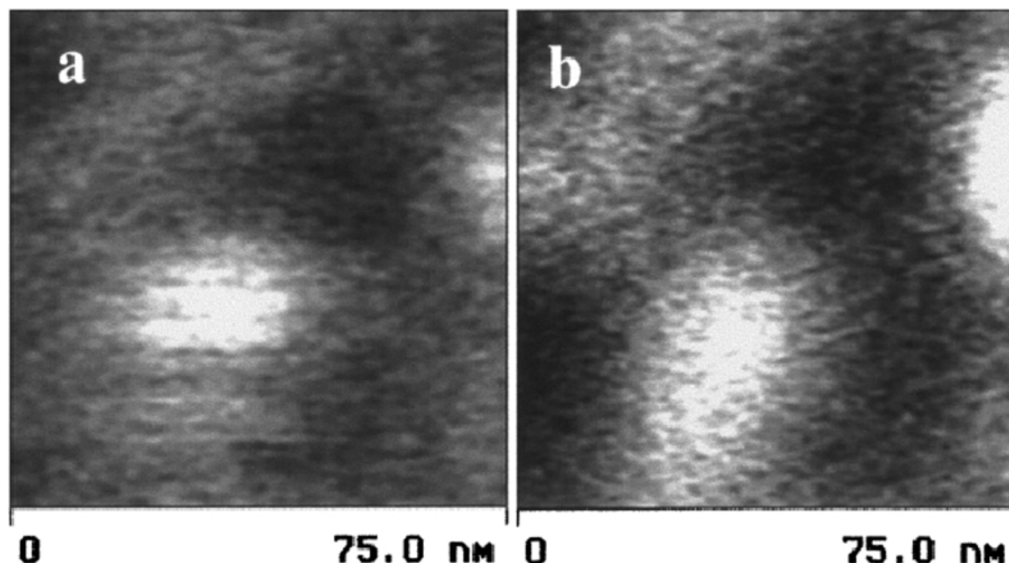

FIG. 11. Nanocrystal charge (a) and dielectric constant (b). In the slow-scan direction (top to bottom), the central nanocrystal becomes neutralized by an electron and "blinks off." (Reprinted figure with permission from Ref. 28, Copyright 1999, American Physical Society.)

(right) photoexcitation: with photoexcitation, more than 50% of the nanocrystals become positively charged (bright spots). Such charging does not occur when laser light below the CdSe bandgap is used. It is hypothesized that photoexcitation increases the probability of an electron to tunnel through the insulating ligand cap to delocalize[28,35] (electrons have a lower energy barrier to surmount from CdSe through the ligands than do holes).

EFM on Semiconductor Nanocrystal Films

Assembling nanocrystals into arrays and devices may provide electronic and optoelectronic functions such as light emission,[34,36–38] light detection,[39,40] and photovoltaic power generation.[41,42] EFM was adapted in a novel way[43] to measure the diffusion coefficient D and resistance R of a nanocrystal monolayer film: rather than applying an AC voltage to the tip,

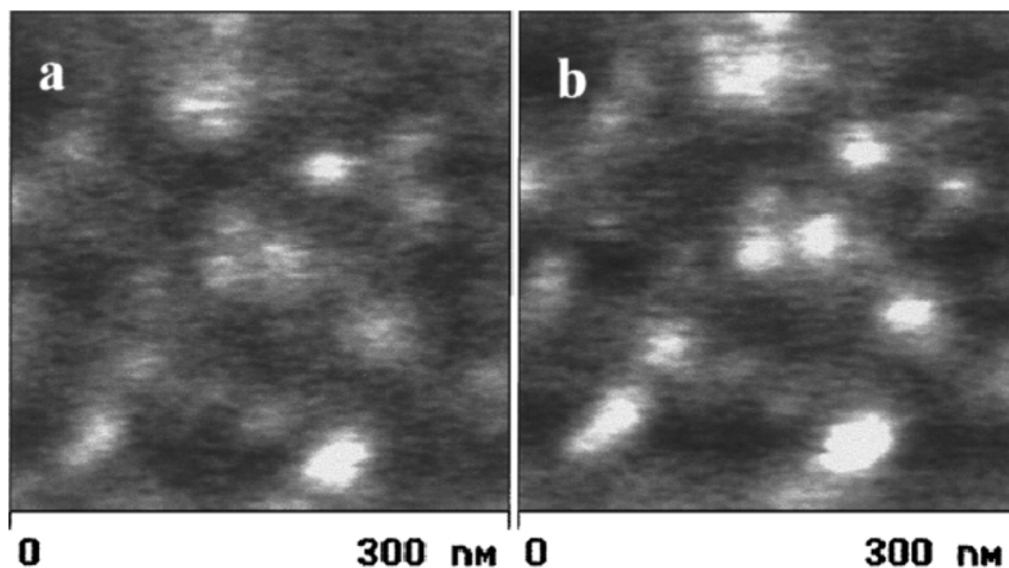

FIG. 12. Nanocrystal charge before (a) and after (b) photoexcitation above the bandgap; photoexcitation enhances electron delocalization, leaving positively charged nanocrystals. (Reprinted figure with permission from Ref. 28, Copyright 1999, American Physical Society.)

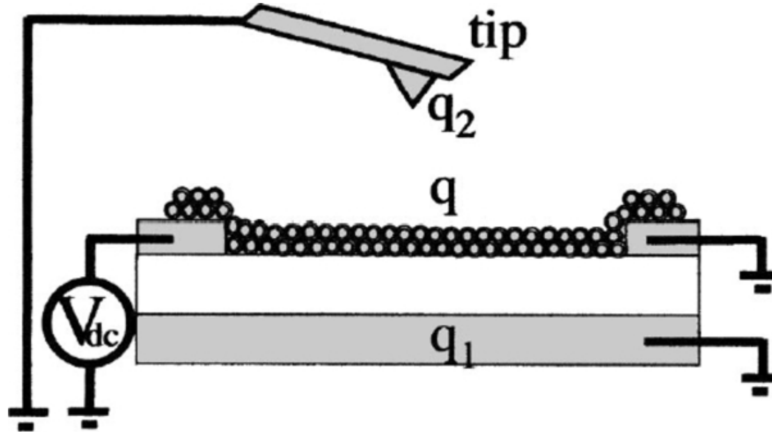

FIG. 13. MOS experimental configuration for nanocrystal thin film. (Reprinted with permission from Ref. 43, Copyright 2003, American Institute of Physics.)

the sample was excited and EFM tip oscillations were used to image the sample charge diffusion. Because the film contained a continuous distribution of charge instead of a point source, lateral spatial resolution was reduced to ~400 nm.[43]

CdSe nanocrystals (nominal diameter 6.1 nm) were dispersed onto a FET structure (see Figure 13); the source electrode was excited to −40 V for up to four hours. Constant height (double-pass) measurements showed charge spreading over time as illustrated in Figure 14a—the bottom image in (a), taken 40 minutes after the first, shows more charge around the source electrode (delineated at the top of each sub-image). Due to the strong electrostatic force around the source electrode, EFM could not obtain a correct topographic image on the first scan of the double-pass so constant height could not be maintained; estimated error was subtracted out of the image.[43]

After complete charging of the film, the source was returned to ground and charge diffused back to equilibrium; Figure 14b shows nine minutes elapsed between top and bottom images and the charge can be seen to have spread out. Moreover, repeated scans were taken over time at along the x-axis for a fixed y position and the results plotted in Figure 15. By simultaneously fitting the charge profile

$$Q_{\rm ch}(x,t) = Q_0\left[1 - \mathrm{erf}\left(\frac{x}{2\sqrt{Dt}}\right)\right], \qquad [10]$$

the best fit was obtained for $D = (2.8 \pm 0.2) \times 10^{-3}\ \mu\mathrm{m}^2/\mathrm{s} = (2.8 \pm 0.2) \times 10^{-11}\ \mathrm{cm}^2/\mathrm{s}$; this is a minute diffusion coefficient compared to bulk semiconductors with $D \sim 25\ \mathrm{cm}^2/\mathrm{s}$. Plotting the peak charge distribution against time (inset of Figure 15) gives the same value of D.[43]

Resistance was calculated using $R = 1/DC$ where $C = \epsilon/z \approx 10^{-16}\ \mathrm{F}/\mu\mathrm{m}^2$, giving $R \sim 10^{16}\ \Omega$ for the geometry of the device. This implies a current of 10^{-15} A at −40 V that could not have been measured by other means.[43] This modified EFM technique could be used to characterize other highly resistive thin films.

SCANNING CAPACITANCE MICROSCOPY

In scanning capacitance microscopy (SCM), the sample under test is normally covered with a thin dielectric layer. The tip–sample contact forms a metal–insulator–semiconductor (MIS) capacitor whose capacitance–voltage (C–V) behavior is determined by the local carrier concentration of the semiconductor sample.

Principles of Operation

In SCM mode, an ultra-high-frequency resonant capacitance sensor detects the capacitance at the conductive probe tip via a transmission line. A sinusoidal bias is applied to the sample, driving the semiconductor surface at the point of contact back and forth repetitively from accumulation to depletion of charge carriers. The resulting change in capacitance is detected by a shift in the center frequency or phase of the resonance circuit that includes the sensor, the transmission line, probe and semiconductor sample. The SCM $\mathrm{d}C/\mathrm{d}V$ signal is acquired as the tip scans over the semiconductor surface. The magnitude of the SCM signal is related to the local free carrier concentration in the sample.

Four parameters define the SCM operating point: the AC bias modulation voltage, the modulation frequency, the DC offset voltage, and the capacitor sensor probing voltage. A DC offset voltage is used to compensate the C–V curve flatband shift caused by charge trapped in the dielectric layer and Fermi level variation. This DC voltage is adjusted to maximize the change in differential capacitance signal (maximum C–V curve slope) prior to each SCM scan over the entire sample. Data are acquired in two different SCM modes: (i) $\mathrm{d}C/\mathrm{d}V$, in which either the amplitude or phase of the capacitance variation is obtained for a given voltage modulation on the sample; and (ii) feedback, wherein the AC voltage is adjusted to maintain a constant capacitance (depletion depth) throughout the image. As with SSRM,

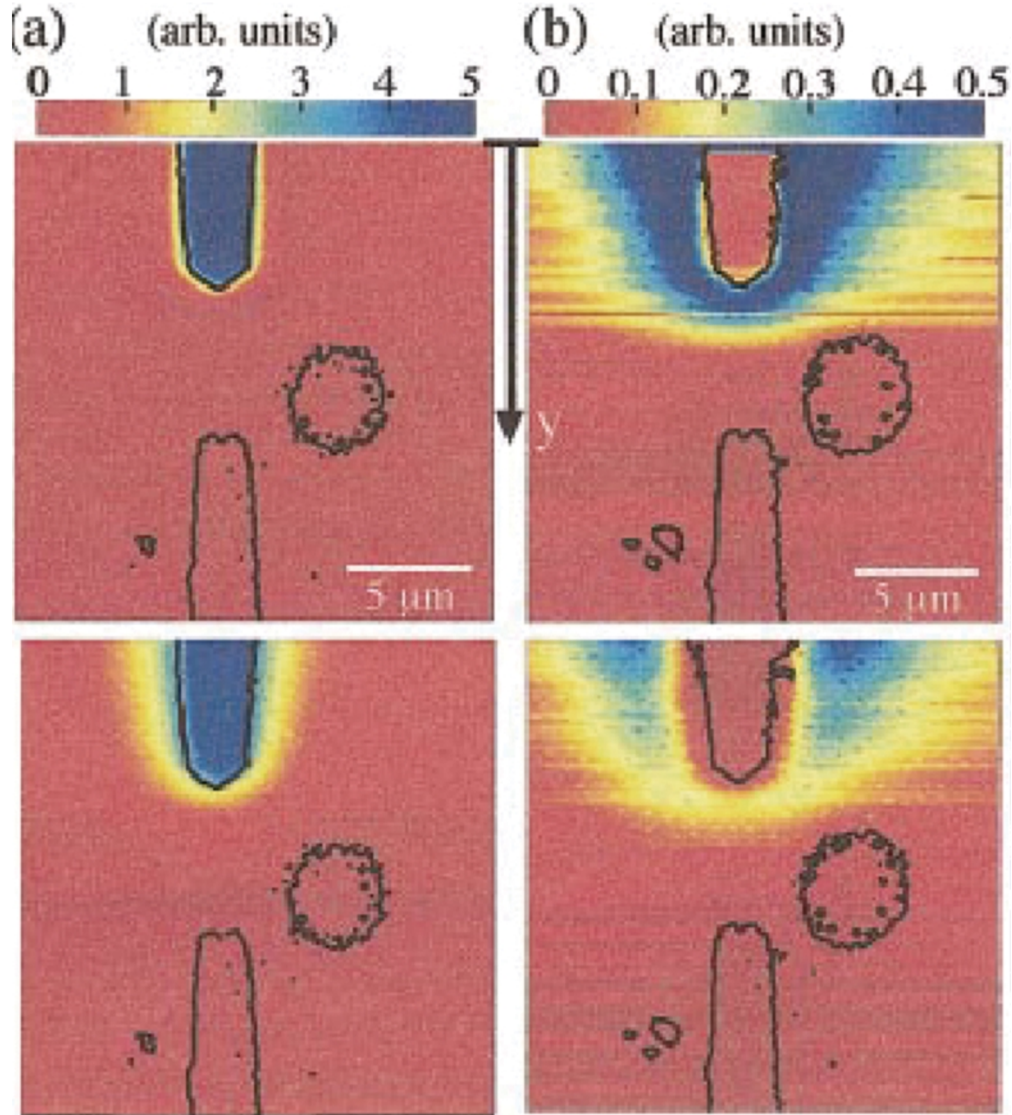

FIG. 14. Charge spreading over time from the source electrode: the bottom image in (a), taken 40 minutes after the top, shows more charge (white glow) around the source electrode (delineated at the top of each image). In (b), nine minutes elapsed between top and bottom images and the charge can be seen to spread out. (Reprinted with permission from Ref. 43, Copyright 2003, American Institute of Physics.)

the tip is scanned in contact mode at 0.25–4 μm/s, but a much lower contact force is used. The tip bias is typically varied from 0.2 to 1.5 V peak-to-peak.

Upon the application of a sinusoidal bias between the tip and semiconductor sample, carriers alternatively are depleted or accumulated in the semiconductor region underneath the contact point of the tip. The total capacitance of the tip–oxide–semiconductor interface consists of two parts: oxide capacitance (C_{ox}) and semiconductor accumulation–depletion capacitance (C_s) :

$$\frac{1}{C} = \frac{1}{C_{ox}} + \frac{1}{C_s}. \quad [11]$$

The overall capacitance is given by

$$C = \frac{C_{ox}}{\sqrt{1 + \left(2VC_{ox}^2/q\epsilon n\right)}}, \quad [12]$$

where V is the applied bias, n free carrier density, and ϵ dielectric constant. If the oxide capacitance remains constant during the scan, the measured SCM signal dC/dV is obtained,

$$\frac{\mathrm{d}C}{\mathrm{d}V} = \frac{C_{ox}^3}{q\epsilon n\left[1 + \left(2VC_{ox}^2/q\epsilon n\right)\right]^{3/2}}. \quad [13]$$

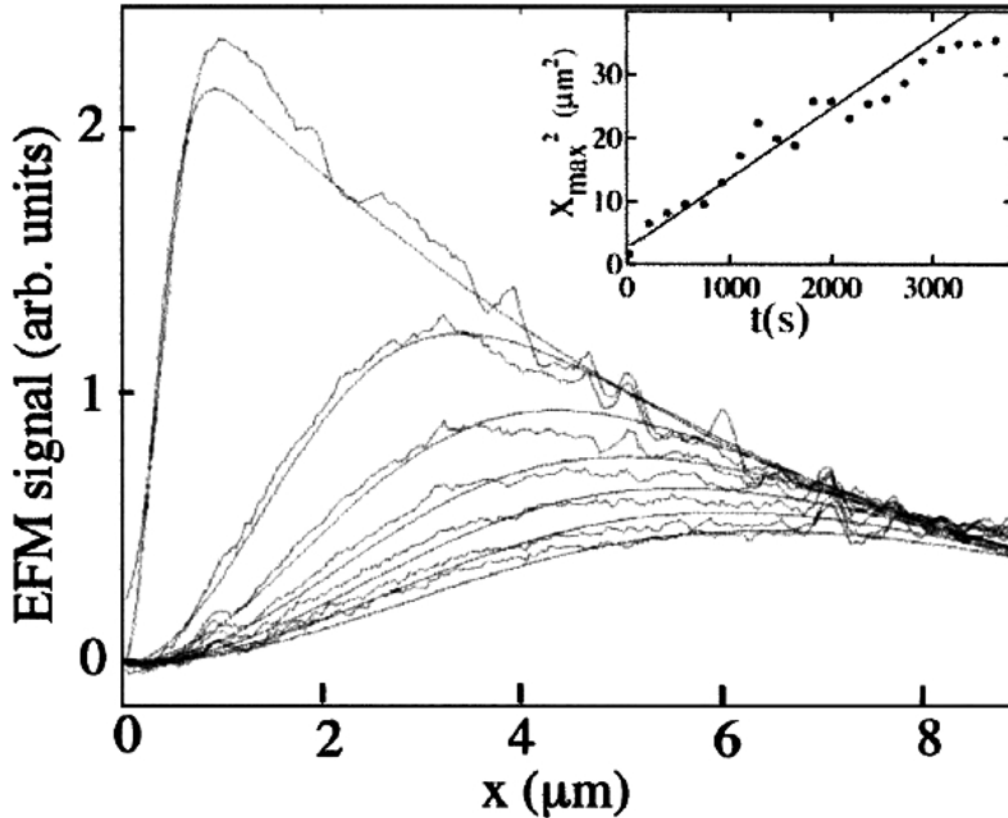

FIG. 15. Charge diffusion from the source electrode over several minutes; the diffusivity of the resistive film is obtained in the fitted curve. (Reprinted with permission from Ref. 43, Copyright 2003, American Institute of Physics.)

Equation 13 discloses the dependence of the SCM signal on the carrier density. Actual SCM measurement is in reality more complicated than this ideal model: the SCM output signal is affected by operational parameters such as the AC bias modulation voltage, the modulation frequency, the DC offset voltage, and the capacitor sensor probing voltage. Consequently, to convert the SCM signal to local carrier density directly is a significant challenge.

SCM of III-V Semiconductor Laser Diodes

SCM has been used to examine BH lasers in cross-section. SCM is a nondestructive technique due to the weak force applied by the probe tip to the sample surface. Figure 16 shows typical SCM images obtained on the uncoated facet of the BH laser device in (a) dC/dV open loop amplitude mode and (b) feedback closed-loop amplitude mode. The AC bias voltage is 0.5 V peak-to-peak and the scan rate is 0.25 Hz in the open loop mode scanning. In the closed-loop mode, the capacitance feedback set-point is set to 1.0 V and the scan rate is 0.25 Hz. Both SCM images show the basic cross-sectional features of the BH laser, but the spatial resolution is not as good as in the corresponding SSRM image (Figure 5). This difference occurs because the spatial resolution in the SSRM image is mostly determined by the radius of the probe tip, whereas the spatial resolution of a SCM image depends more on the lateral distribution of the depletion region in the semiconductor underneath the probe contact point.

In the open loop image, the n- and p-doped layers of the BH laser appear as darker and brighter regions, respectively. Due to the high image contrast between n- and p-doped regions, SCM is often used for the delineation of p–n junctions.[44] In comparison with the SSRM image, SCM provides only a weak contrast among the regions of the same doping type but with different doping concentrations. The nonlinear correlation between the SCM signal and the carrier density has been discussed and reported by several groups.[45,46]

Dark broad lines along p–n junctions are observable in the closed-loop image. SCM response in the closed-loop amplitude mode is much more sensitive to the junction depletion region because the surface is already highly depleted and a small AC signal is enough to maintain the preset constant change in depletion width. The broadening of the p–n junction, as seen in Figure 16b, results from the finite tip size and interaction volume. The darkness in the closed-loop SCM image reveals low free carrier density, particularly over the regions near the active region–thyristor interface. As will be seen from later SVM analysis, this gives rise to the clamping of the prospective leakage path between the two p-InP layers and consequently the blocking of diode leakage current.

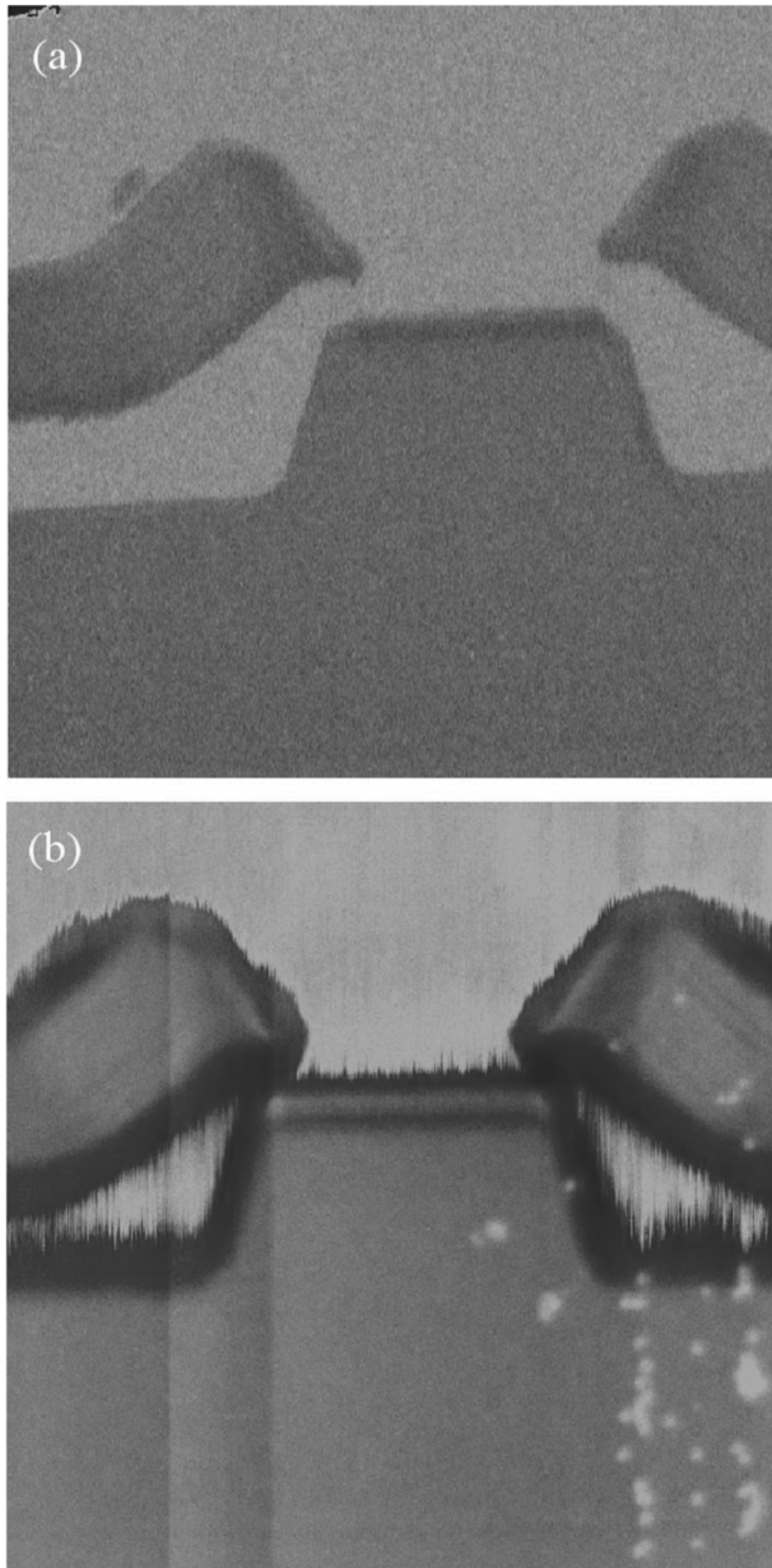

FIG. 16. Typical SCM image obtained on the cross-section of a MQW BH laser, (a) Open loop amplitude mode, an AC bias of 0.3 V and scan rate of 0.5 Hz; (b) Closed-loop amplitude mode, a capacitance feedback set-point of 1.0 V and scan rate of 0.25 Hz. The depletion regions of *p–n* junctions are particularly apparent in (b). (Reprinted with permission from Ref. 25, Copyright 2002, AVS The Science & Technology Society.)

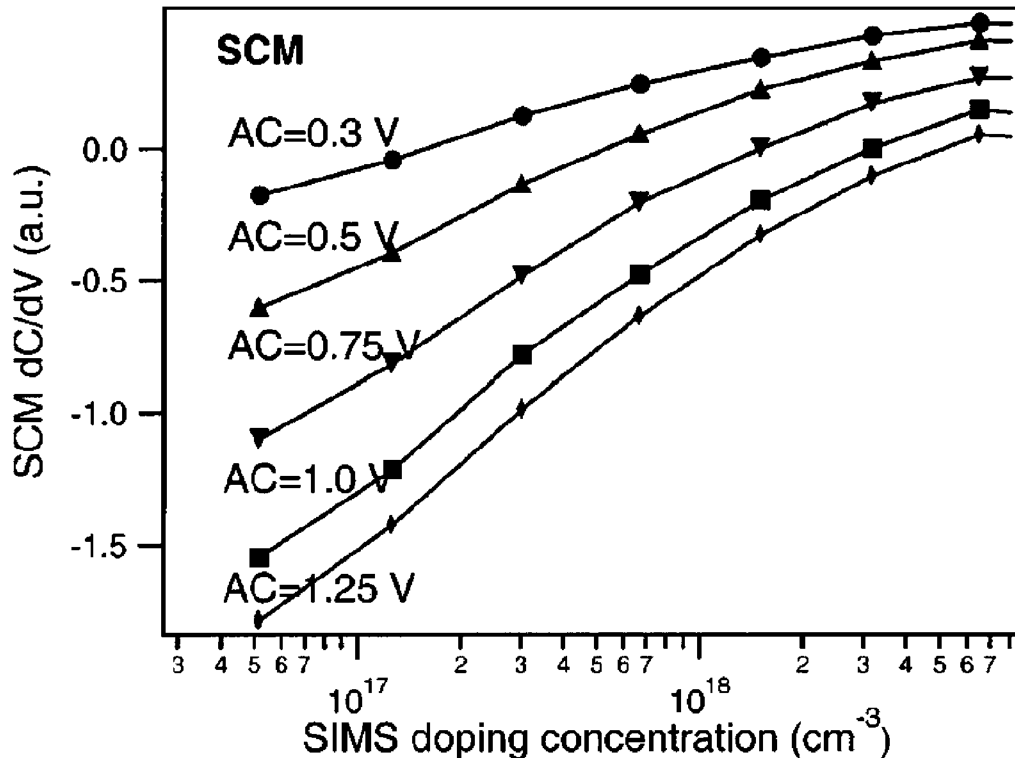

FIG. 17. SCM signal ($\mathrm{d}C/\mathrm{d}V$) versus the SIMS dopant concentration for the n-type InP standard sample. The correlation curves are obtained at each of the following AC bias voltages: 0.3, 0.5, 0.75, 1.0, and 1.25 V. (Reprinted with permission from Ref. 25, Copyright 2002, AVS The Science & Technology Society.)

Similar to SSRM, SCM calibration curves are obtained by plotting the SCM measured signal against the doping concentration as determined by SIMS for an n-type InP standard sample. Five calibration curves, measured under different AC bias voltages, are plotted in Figure 17. The SCM signals ($\mathrm{d}C/\mathrm{d}V$) at different AC biases tend to converge at high doping. These curves are now used, combined with the SCM values acquired on the p–n–p–n structure of the BH laser, to derive the carrier density of the n-doped layers in the device.

Using the calibration curves of Figure 17, the carrier density of each layer in the p–n–p–n structure of the BH laser can be obtained. As distinct from SIMS, which measures the total dopant concentration without regard for electrical activation, SSRM and SCM probe local conductivity and carrier density, respectively.

SCANNING VOLTAGE MICROSCOPY: PRINCIPLES OF OPERATION

Apparatus

SVM Circuit

In 1952 Pearson, Read, and Shockley[47] probed the space charge region of a germanium p–n junction with a submillimeter tungsten probe by measuring the potential zeroing current between the probe and sample, the first direct voltage observation of its kind. By lightly dragging the tip across the device surface they found experimental measurements of the depletion width to be within 30% of theoretical values.

Scanning voltage microscopy places a nanoscopic voltage probe on an actively biased sample[13,14,24,48] as illustrated in Figure 18. Using a high-impedance voltmeter ensures that negligible current is drawn from the sample and normal device operation is maintained. The voltmeter is simply used as a high-impedance buffer and its analog output is passed directly to data collection hardware and software. By rastering the probe over the sample surface via an atomic force microscope, voltage maps and profiles are collected. Spatial resolution down to ~5 nm is possible so that small features such as individual quantum wells can be resolved.[24]

SVM Configuration in Practice

The experimental configuration references the n-type contact to ground so that no inversion of the voltage data is necessary and there is no DC offset. The grounds of the current source and voltmeter are connected to eliminate ground loop noise; noise from the probe is reduced by connecting the shielding of its cable to the common star ground point. Buffered voltage data are directed into the data collection system by replacing the lateral friction signal (which is not needed) from the tip with the voltage signal.

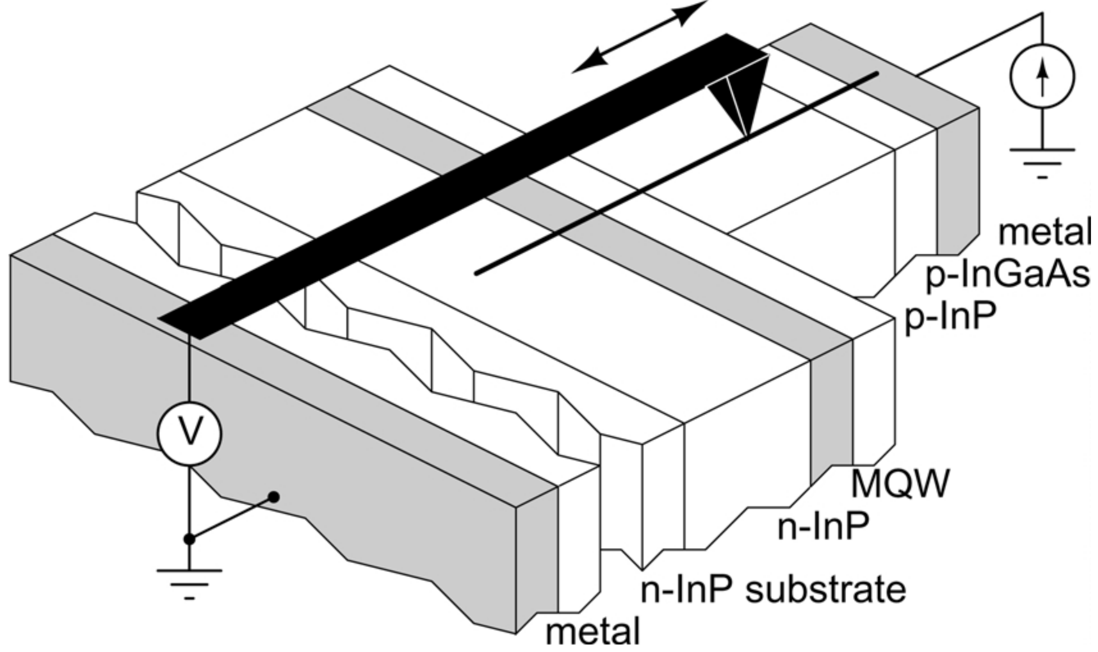

FIG. 18. Voltage scanning a ridge waveguide laser. The conductive SVM probe tip is rastered over the cleaved facet and the voltage recorded at each position. (Reprinted with permission from Ref. 49, Copyright 2005, American Institute of Physics.)

In order to measure the voltage difference between the reference point and the AFM probe contact point, and also to minimize disruption to the operation of the device under test, use of a voltmeter with very high input impedance is crucial. An operational amplifier circuit configured as a voltage follower must offer the high input impedance, typically greater than 10^{14} Ω.

Theoretical Interpretation of Measured Voltage

Thermodynamic Interpretation

The measured voltage between any two points, say, between a voltage probe and a grounded reference point, is the difference in the local electrochemical potentials,[50]

$$\triangle\phi = \phi_{\text{probe}} - \phi_{\text{reference}}, \quad [14]$$

where the electrochemical potential is equivalent to the (quasi) Fermi level of a semiconductor,[51]

$$q\triangle\phi = \mu_e(x_1) - \mu_e(x_2). \quad [15]$$

Electrochemical potentials can be easily derived for electrons

$$n_b = n_0 e^{q(\phi_b - \phi_0 - \phi_n)/k_B T} \quad [16a]$$

$$\Rightarrow \phi_n = (\phi_b - \phi_0) - \frac{k_B T}{q} \ln \frac{n_b}{n_0} \quad [16b]$$

and for holes

$$p_b = p_0 e^{q(-\phi_b + \phi_0 + \phi_p)/k_B T} \quad [17a]$$

$$\Rightarrow \phi_p = (\phi_b - \phi_0) + \frac{k_B T}{q} \ln \frac{p_b}{p_0}. \quad [17b]$$

In these equations, $\phi_{n,p}$ are the electron and hole electrochemical potentials (quasi-Fermi potentials), $\phi_b - \phi_0$ is the electrostatic potential, and $n_{0,b}$ and $p_{0,b}$ are the electron and hole concentrations at equilibrium and under bias.

Although there is a built-in potential across the depletion region of a *p–n* junction at zero bias,[52] this potential cannot be measured by a voltage probe because built-in potentials form at each probe contact point, exactly canceling the built-in potential at the junction. Thus, SVM *must measure flat, zero potential across a device at equilibrium.*

If energy is provided to the junction, the measured electrochemical potential becomes[48,53]

$$\phi(x, y) = (\phi_b(\mathbf{r}) - \phi_0(\mathbf{r})) \pm \frac{k_B T}{q} \ln \frac{c_b(\mathbf{r})}{c_0(\mathbf{r})}, \quad [18]$$

where the first term is the electrostatic potential and the second term is the chemical potential containing bias and equilibrium carrier densities c_b, and c_0.

The model just described does not take into account details of the perturbation of the sample by the AFM probe. In order to consider the impact of the probe, a drift-diffusion model is introduced in the following section from the other extreme point of view, wherein the probe determines the alignment of the energy bands of the sample surface at the contact point through the transport of carriers to and from the tip. There will be agreement between the thermodynamic and carrier transport views.

Carrier Transport Interpretation

When a metal contact is placed on a semiconductor material that is not in electronic equilibrium, a floating potential is

established between the metal and the bulk semiconductor.[54] A semiconductor beyond equilibrium has two quasi-Fermi levels: one describes the occupation probability of electrons, the other of holes. An especially important case is the active region of a laser biased above lasing threshold as the quasi-Fermi levels of electrons and holes may differ significantly from each other. The probe (modelled as a metal) interacts with the electrons and holes as it is placed in contact with the active region (i.e., as the probe is scanned along a given direction). Through the action of the feedback loop in the high-impedance amplifier circuit, the metal Fermi level is adjusted such that the net current between the probe and the semiconductor is zero.

Figure 19 shows the energy diagram at the interface of a metal probe and a semiconductor surface (InP is taken as a specific example), in which the quasi-Fermi levels of electrons $\mathcal{E}_{Fn}$ ($q\phi_n$) and holes $\mathcal{E}_{Fp}$ ($q\phi_p$) are assumed to merge into the metal Fermi level $\mathcal{E}_{Fm}$ ($q\bar{\phi}$) at the semiconductor boundary.[55] On the semiconductor side near the contact, the carrier densities $n(x)$ and $p(x)$ differ from the values in the bulk. This is reflected by the variation of $q\phi_n$ and $q\phi_p$ along the horizontal (x) axis in Figure 19b.

Current flow is restricted to one dimension, normal to the semiconductor surface; this assumption is supported by spreading resistance calculations of Ref. [57] and confirmed

a) Contact upon first probe tip placement or relocation

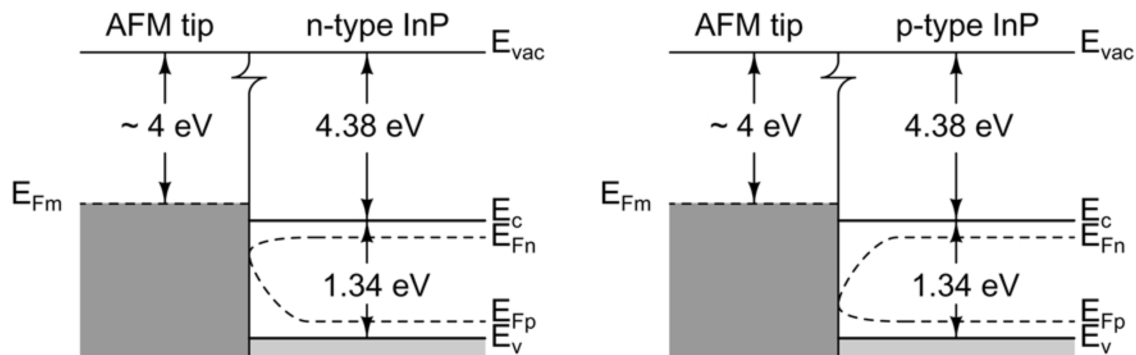

b) Steady-state contact after sufficient steady-state approach time

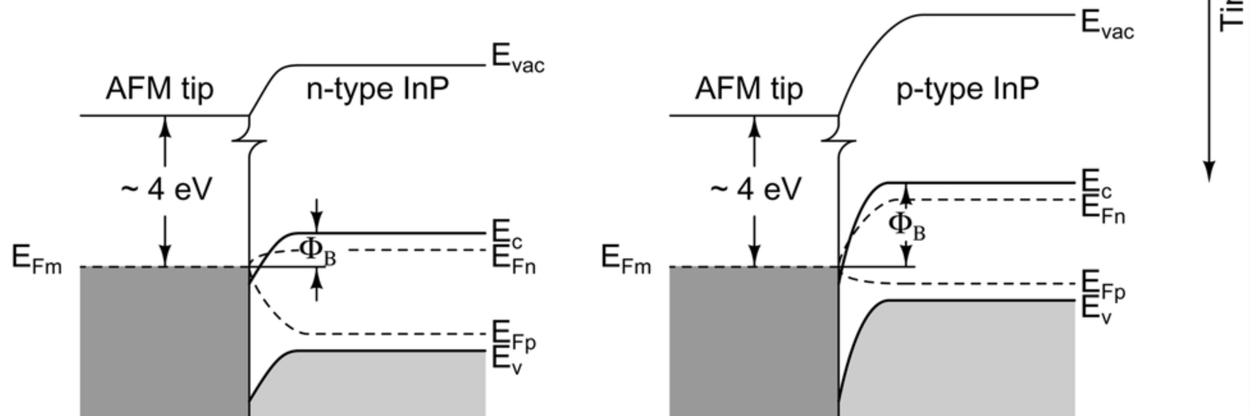

FIG. 19. Energy band diagram of tip–sample interface for n-type (left) and p-type (right) InP sample material: tip Fermi level $\mathcal{E}_{Fm}$ (work function near 4 eV), conduction band $\mathcal{E}_c$, valence band $\mathcal{E}_v$, quasi-Fermi levels $\mathcal{E}_{Fn}$ and $\mathcal{E}_{Fp}$, and Schottky barrier height Φ_B. (a) Non-steady-state condition at first probe–sample contact or after probe relocation, (b) Steady-state results when the Fermi levels align with charge redistribution, causing band bending and formation of space charge regions into the sample at the interface. Band bending is more severe for p-type InP and yields higher contact resistance. (Adapted from Ref. 56, reprinted with permission, Copyright 2004, American Institute of Physics.)

experimentally in, for example, nanometer-spatial resolution SSRM measurements.[58] Restricting current flow to one dimension along x between tip and sample the electron and hole current densities J_p and J_n are given by

$$J_n = -en\mu_n \frac{d\phi_n}{dx},\quad J_p = -ep\mu_p \frac{d\phi_p}{dx}. \qquad [19]$$

No current is drawn by the probe at steady-state, so the current $J(x)$ is defined as $J(x) \stackrel{\Delta}{=} J_n = -J_p$. Separating variables, multiplying by the sample carrier densities far from the surface, $\tilde{n}$ and $\tilde{p}$, and integrating from the surface ($x = 0$) to a point far from the surface in the sample ($x = d$), yields[55]

$$\int_0^d \tilde{n}\frac{J(x)}{n(x)}dx = -e\mu_n\tilde{n}(\tilde{\phi}_n - \bar{\phi}),\quad \int_0^d \tilde{p}\frac{J(x)}{p(x)}dx = -e\mu_p\tilde{p}(\tilde{\phi}_p - \bar{\phi}), \qquad [20]$$

where the "∼" overline denotes a quantity deep in the device well away from the interface, and $\bar{\phi}$ is the potential right at the interface that is registered on the voltmeter.

Adding these equations and dividing by $e(\tilde{n}\mu_n + \tilde{p}\mu_p)$ isolates the probe potential,

$$\bar{\phi} = \frac{\tilde{n}\mu_n\tilde{\phi}_n + \tilde{p}\mu_p\tilde{\phi}_p}{\tilde{n}\mu_n + \tilde{p}\mu_p} + \Delta, \qquad [21]$$

where the quasi-Fermi level band-bending Δ is defined as

$$\Delta \stackrel{\Delta}{=} \frac{1}{e(\tilde{n}\mu_n + \tilde{p}\mu_p)}\int_0^d \left(\frac{\tilde{n}}{n(x)} - \frac{\tilde{p}}{p(x)}\right)J(x)dx. \qquad [22]$$

Δ is small when $\tilde{n} \approx \tilde{p}$ in the case of quasi-space charge neutrality, yielding

$$\bar{\phi} = \frac{\tilde{n}\mu_n\tilde{\phi}_n + \tilde{p}\mu_p\tilde{\phi}_p}{\tilde{n}\mu_n + \tilde{p}\mu_p}. \qquad [23]$$

The measured potential given by Eq. 23 is an average of the quasi-Fermi levels (electrochemical potentials), weighted by the carrier density–mobility products. When the semiconductor is at equilibrium, $q\tilde{\phi}_n = q\tilde{\phi}_p \stackrel{\Delta}{=} \tilde{\mathcal{E}}_F$, yielding

$$q\bar{\phi} = \frac{\mu_n\tilde{n}\tilde{\mathcal{E}}_F + \mu_p\tilde{p}\tilde{\mathcal{E}}_F}{\mu_n\tilde{n} + \mu_p\tilde{p}}, \qquad [24]$$

from which $\tilde{\phi} = \tilde{\mathcal{E}}_F/q$ clearly follows. Therefore, the probe measures the Fermi level of a semiconductor at equilibrium. At equilibrium, the Fermi level is flat across the entire device[52] and thus the measured potential is zero as dictated by thermodynamics.

In unipolar regions where one carrier type dominates, the measured potential $\bar{\phi}$ tends toward the dominant quasi-Fermi level,

$$\bar{\phi} \to \tilde{\phi}_n, \quad \mu_n\tilde{n} \gg \mu_p\tilde{p} \qquad [25a]$$

$$\bar{\phi} \to \tilde{\phi}_p, \quad \mu_p\tilde{p} \gg \mu_n\tilde{n}. \qquad [25b]$$

Hence, in heavily doped p-type regions the voltage probe is expected to follow $\tilde{\phi}_p$. For example, if there is a heterojunction between p-type materials having different band gaps, a voltage drop should be observed under forward bias corresponding to the change in $\tilde{\phi}_p$ across the heterojunction. It will be seen that such voltage drops are indeed observed in operating heterojunctions.

In the case that there is quasi-space charge neutrality (e.g., across a depletion or intrinsic region) $\tilde{n} \approx \tilde{p}$ and

$$\bar{\phi} = \frac{\mu_n\tilde{\phi}_n + \mu_p\tilde{\phi}_p}{\mu_n + \mu_p}, \qquad [26]$$

the mobility-weighted average of the electron and hole quasi-Fermi levels. Such a reduction has been well validated across the depletion region of a p–i–n junction.[55]

Finally, in regions where $\tilde{\phi}_{n,p}$, $\tilde{n}$, $\tilde{p}$, and $\mu_{n,p}$ change rapidly and simultaneously (e.g., in a quantum well active region), $\bar{\phi}$ may well become difficult to interpret. However, this in no way degrades the application of this model to bulk regions and heterojunctions.

The drift-diffusion model yields the same results as given by the thermodynamic model presented earlier under the assumption of one dominant quasi-Fermi level.

Proof-of-Concept: SVM on InP *p–n* Junction

In order to verify the equations derived earlier, SVM measurements were performed on an InP p–n junction under forward and reverse biases.

The p–n junction sample grown by molecular beam epitaxy (MBE) consisted of two 500 nm thick InP layers. The two layers were Be- (for p-type) and Si-doped (for n-type), respectively, both with the nominal doping concentration of 10^{18} cm^{-3}. A heavily p-doped 200 nm InGaAs layer was grown at the top surface of the p–n junction for ohmic contact. A simple cleave was made to expose the cross-section of the p–n junction.[17]

Current-voltage characteristics of the samples were measured before, during, and after the SVM experiment—stable electrical device characteristics were obtained at all times. AFM images of the sample surface obtained simultaneously with the SSRM and SVM data showed no perceptible topographic features.

SSRM was first deployed to examine the cross-section of the p–n junction. Figure 20 shows a two-dimensional SSRM image obtained on the freshly cleaved facet of the p–n junction.

The n^+ substrate is the bright band at the bottom. Topmost is the heavily p-doped InGaAs layer. The p- and n-doped InP layers are clearly resolved in the SSRM image. The 0.37 nm–thick GaP marker layers within the n-doped InP layer, as shown

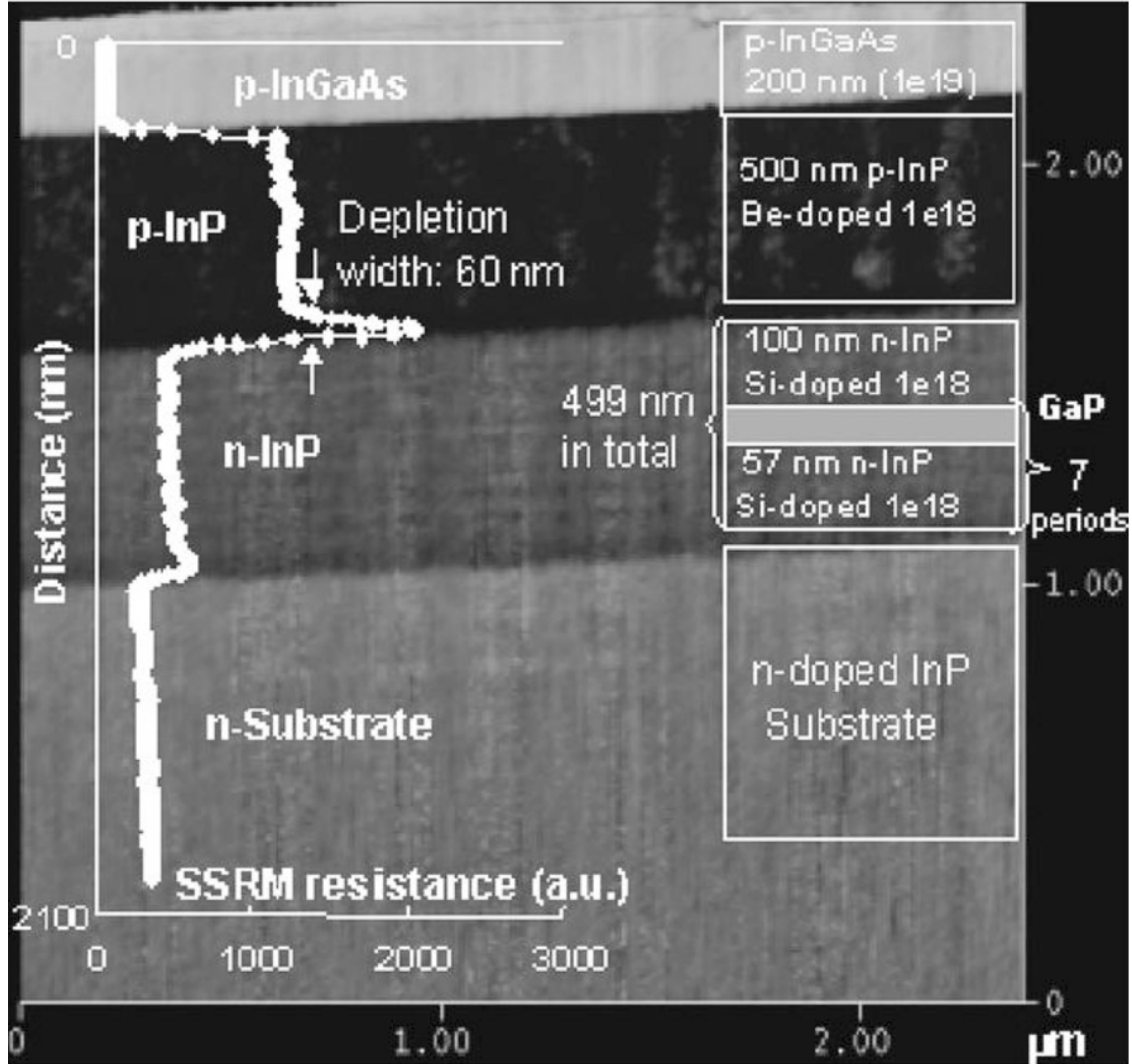

FIG. 20. An SSRM image of a *p–n* junction sample. The scan rate is 0.25 Hz and tip DC bias is 1.0 V. The ultrathin (0.37 nm) GaP mark layers, as shown in the inset, are resolved in the image. The cross-sectional SSRM resistance curve overlaid on the image shows the depletion width of the *p–n* junction at equilibrium is approximately 60 nm. (Reprinted with permission from, Ref. 48, Copyright 2002, American Institute of Physics.)

in the inset of the schematic structure of the sample, can be resolved in the 2-D image, attesting to the high spatial resolution of this technique.

A cross-sectional SSRM resistance curve is obtained by averaging the scan lines that make up the 2-D image of Figure 20 and is presented in the overlay. It shows that the depletion width of the *p–n* junction is around 60 nm. The impact of the GaP marker layers on the electrical characteristics of the *p–n* junction is negligible because they are ultra thin and far away from the junction depletion region.

A simple model of the *p–n* junction predicts the appearance of a depletion layer at the interface of the *p–n* junction and allows a precise calculation of its depletion width as a function of applied bias. The width of depletion region at equilibrium is given by[52]

$$W_0 = \left[\frac{2\epsilon_r\epsilon_0 k_B T}{q^2}\ln\left(\frac{N_a N_d}{n_i^2}\right)\left(\frac{1}{N_a}+\frac{1}{N_d}\right)\right]^{1/2}. \qquad [27]$$

The relative permittivity ϵ_r of InP is 12.56; the doping concentrations of the *p–n* junction treated herein are $N_a = 1.0 \times 10^{18}$ cm^{-3} and $N_d = 1.0 \times 10^{18}$ cm^{-3}; and for InP at 300 K, $n_i = 1.2 \times 10^8$ cm^{-3}. The depletion region width of the *p–n* junction at equilibrium is calculated to be $W_0 = 57$ nm. This agrees with the measured result of 60 nm from SSRM.

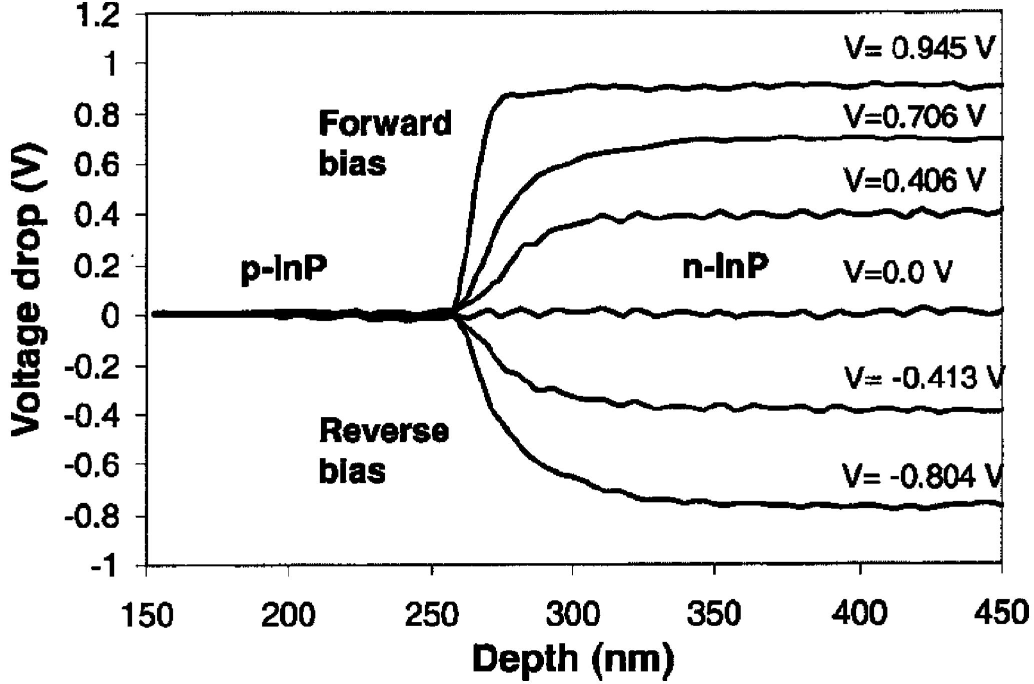

FIG. 21. Cross-sectional voltage drop across the p–n junction under forward and reverse biases. Voltage falls essentially within the depletion region of the p–n junction. The voltage drop curves show that the depletion region shrinks as the applied voltage changes from reverse to forward bias. (Reprinted with permission from Ref. 48, Copyright 2002, American Institute of Physics.)

The simple model of the p–n junction predicts the depletion width (W) as a function of applied bias (V),

$$W(V) = W_0\left[1 - \frac{V}{V_{bi}}\right]^{1/2}, \quad [28]$$

where W_0 is defined in (Equation 27) and V_{bi} is the built-in voltage across the p–n junction:

$$V_{bi} = \frac{k_B T}{q} \ln \frac{N_a N_d}{n_i^2}. \quad [29]$$

The depletion width of the p–n junction under bias can be estimated from SVM data. Figure 21 shows the cross-sectional voltage distribution curves of the p–n junction under various biases. As the applied voltage changes from reverse to forward, the measured voltage of the n-InP layer (reference to p-contact) increases correspondingly and the transition region from p- to n-InP shrinks, reflecting the change of the depletion region (high-impedance) of the junction.

The depletion widths as a function of device bias, obtained from Figure 21 and calculated using Eq. 28 under forward and reverse biases are shown in Figure 22. Excellent agreement is obtained between the measured and the calculated widths. The measured accumulative voltage changes from p- to n-sides at each bias voltage are also shown in Figure 22, and a linear relationship is obtained, confirming that the SVM probe is measuring the voltage difference between the SVM tip contact point and the reference point in the circuit.

SVM ON Si TRANSISTORS

The first known use of AFM-based SVM was the acquisition of potential maps of actively biased MOS transistors.[13,14] Although these first studies were primarily demonstrative in nature, they offered great promise for further quantitative analysis of electronic and optoelectronic devices in fully operational modes, many examples of which follow in the next section.

Figure 23 shows a corresponding series of SVM images across a cleaved MOS transistor exposing the source–gate–drain structure. Evolution of the transistor in operation can be studied by varying the external bias points from image to image.[13]

Figure 24a shows a high-resolution image of the potential distribution across the cross-section of an operational transistor; both the physical and electronic structures can be seen. Cut-sections through the drain and source are shown in Figure 24b. Cross-sectional voltage maps across the channel were taken and compared to simulation[14]; good qualitative agreement was obtained with a mobility-weighted average of the electrochemical potentials of the holes and electrons, Eq. 26 derived earlier.

SVM ANALYSIS OF InP/InGaAsP-BASED DIODE LASERS

SVM has been applied to study two important semiconductor devices used for advanced optical communication systems,

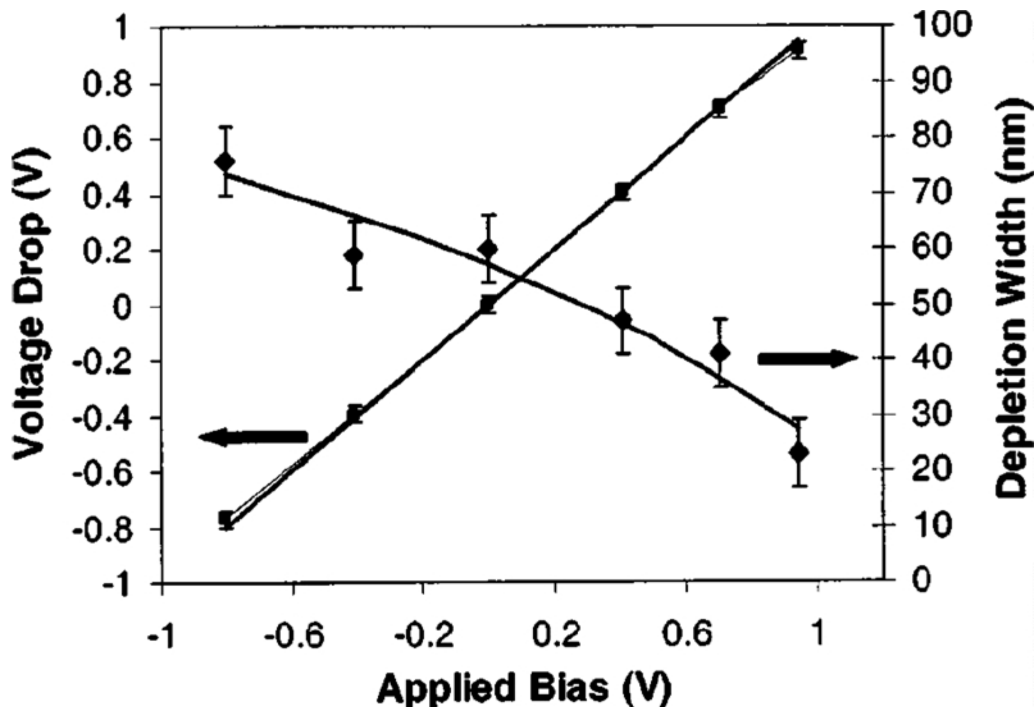

FIG. 22. Measured (discrete diamond) and calculated (solid line) depletion width of the *p–n* junction under different bias voltages. The measured accumulative voltage drop (discrete square) from *p* to *n* side agrees well with the externally applied bias (solid line). (Reprinted with permission from Ref. 48, Copyright 2002, American Institute of Physics.)

namely buried heterostructure multi-quantum-well lasers and ridge waveguide multi-quantum-well lasers. The focus is on direct observation of inner origins of critically important external performance of operating devices such as breakdown of current blocking structures, lateral current spreading, and anomalously high series resistance.

Free carrier distribution within an actively driven laser is an important physical quantity determining the operational performance. Light emission originates from the radiative recombination of holes and electrons, which are injected into the active region from *p*- and *n*-injectors. The spatial overlap of electrons and holes in the MQW active region has a direct impact on the optical gain, and thus the efficiency and optical output power of the laser device.

Lateral Current Leakage

Ridge waveguide (RWG) lasers allow for simple device processing, and provide low threshold current, fundamental lateral transverse mode operation, and nearly circular optical far field patterns. They are technologically important for their applications in optical communication systems. Such applications include RWG gain-coupled distributed feedback lasers for 10 Gb/s directly modulated operation at 85°C,[59] single-mode broad-waveguide In-GaAsP/InP RWG diode lasers emitting in the 1500 nm wavelength range with continuous-wave output power levels in excess of 400 mW[60] and twin ridge waveguide optical amplifier switches with low loss, low polarization sensitivity, and low crosstalk.[61]

The lateral current and carrier profiles underneath the ridge represent one important concern in the design and fabrication of ridge waveguide lasers and related optoelectronic devices.[62–67] Hu *et al.*[64,68] suggested that a large fraction of the current required for lasing in quantum-well RWG lasers is due to lateral current spreading within the device. Current spreading results directly from the structure of the RWG laser: there are no potential barriers in the lateral direction to impede current flow out of the active region. Current leakage due to current spreading—broadening in the lateral current profile—can significantly increase the threshold current density, considerably degrade fundamental transverse mode operation, reduce efficiency above threshold, and disturb the longitudinal mode due to lateral mode instability, causing intermodulation distortion under direct modulation.[69,70]

Evans and coworkers developed an analytical model to evaluate the effects of lateral current spreading on the performance of quantum-well RWG lasers.[62,71] They reported that lateral current spreading in narrow ridge width lasers (less than 5 μm) could be significant—up to 42% at 30°C for a 2 μm ridge width laser. Numerical[64] and experimental[63] studies were used to investigate how laser structures could be designed to reduce current spreading.

In sum, two-dimensional carrier transport effects are widely recognized as an issue of critical significance in RWG laser

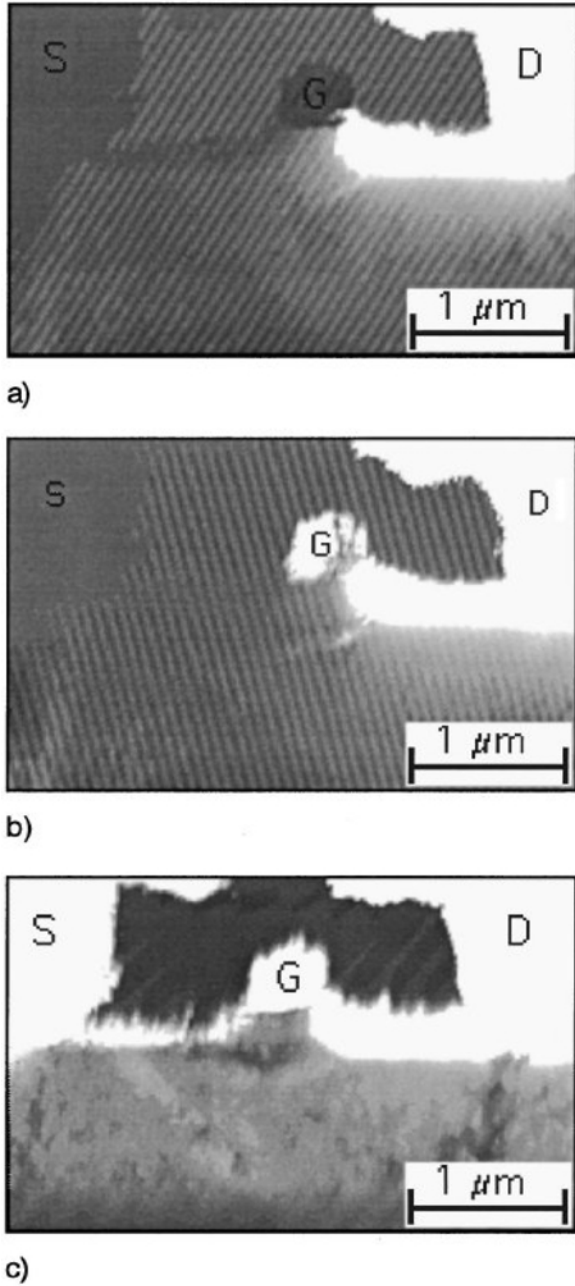

FIG. 23. Potential maps of an N-MOS transistor.[13] (a) Switched off: $V_{DS} = +1$ V, $V_{GS} = V_{SB} = 0$ V. (b) At $V_{DS} = +1$ V, $V_{GS} = +0.25$ V. (c) Switched on: $V_{DS} = +1$ V, $V_{GS} = +0.75$ V. (Reprinted with permission from, Ref. 13, Copyright 1998, AVS The Science & Technology Society.)

operation and optimization. The problem has been tackled through modeling of laser internal operation, taken in conjunction with experimental observation of external performance (light-current-voltage measurements, far field, etc.). The mechanism merits direct internal experimental observation in lasing devices.

Figure 25 shows the two-dimensional SVM image in transverse cross-section of a RWG MQW laser with ridge width of 2.4 μm biased under a forward current injection of 100 mA. The ridge structure and some buried layers beneath the top surface, such as the etch stop layer, the MQW active region, the n- and p-cladding layers and the n-substrate, are resolved in the SVM image. It can be seen in the SVM image that the lateral (parallel to the device top surface) voltage profile within the n-cladding layer is not uniform from one edge to the other across the ridge. This lateral nonuniformity in voltage is more clearly observable in the cross-section shown in the inset. The voltage within the p-InAlAs ridge and MQW active region is flat. However, a difference of up to 75 mV can be measured within the n-InAlAs layer below the ridge. The curve in the n-InAlAs is symmetric with respect to the ridge center—this is expected because of the symmetry of the device structure. The nonuniform lateral voltage distribution within RWG lasers, as revealed in Figure 25, is directly related to lateral current profiles and merits in-depth investigation and further discussion.

The voltage in the n-InAlAs layer below the ridge varies up to 200 mV along the lateral direction at higher device bias. Increased current injection increases the nonuniformity in the lateral voltage distribution. This is reflected in the lateral voltage difference in the n-InAlAs layer, which is around 200 mV at 150 mA, whereas only 75 mV at 100 mA (Figure 25).

Because ridge definition is achieved by etching off the semiconductor layers on the p-doped side until very close to the active layer, current confinement in p-doped layers and even in the MQW active region is well established by the ridge boundary. The lateral voltage profile is consequently uniform across the ridge region. Absence of ridge boundary results in the two-dimensional carrier transport observed in the layers on the n-doped side.

Two-dimensional carrier transport effects may be estimated quantitatively by analysis of the SVM data. It is a good approximation to assume that drift dominates the total current flow in the n-doped region (due to the high doping concentration and electron mobility). The vertical component of the local current density (j) is therefore given by:

$$j = -\sigma \Delta V, \quad [30]$$

where σ is the local conductivity and ΔV is the voltage gradient along the direction perpendicular to the semiconductor junctions.

For an essentially homogeneous conductivity, the voltage gradient drives the current flow. The voltage from the n-InP to n-InAlAs layers is $\Delta V_c = 190 \pm 15$ mV at the center, or $\Delta V_e = 114 \pm 15$ mV at the edge of the ridge, as read directly from the SVM lateral cross-section. The ratio of the local current density at the edge and center is then estimated to be:

$$\frac{j_e}{j_c} = \frac{\sigma \Delta V_e}{\sigma \Delta V_c} = \frac{\Delta V_e}{\Delta V_c} = \frac{114}{190} = 0.6. \quad [31]$$

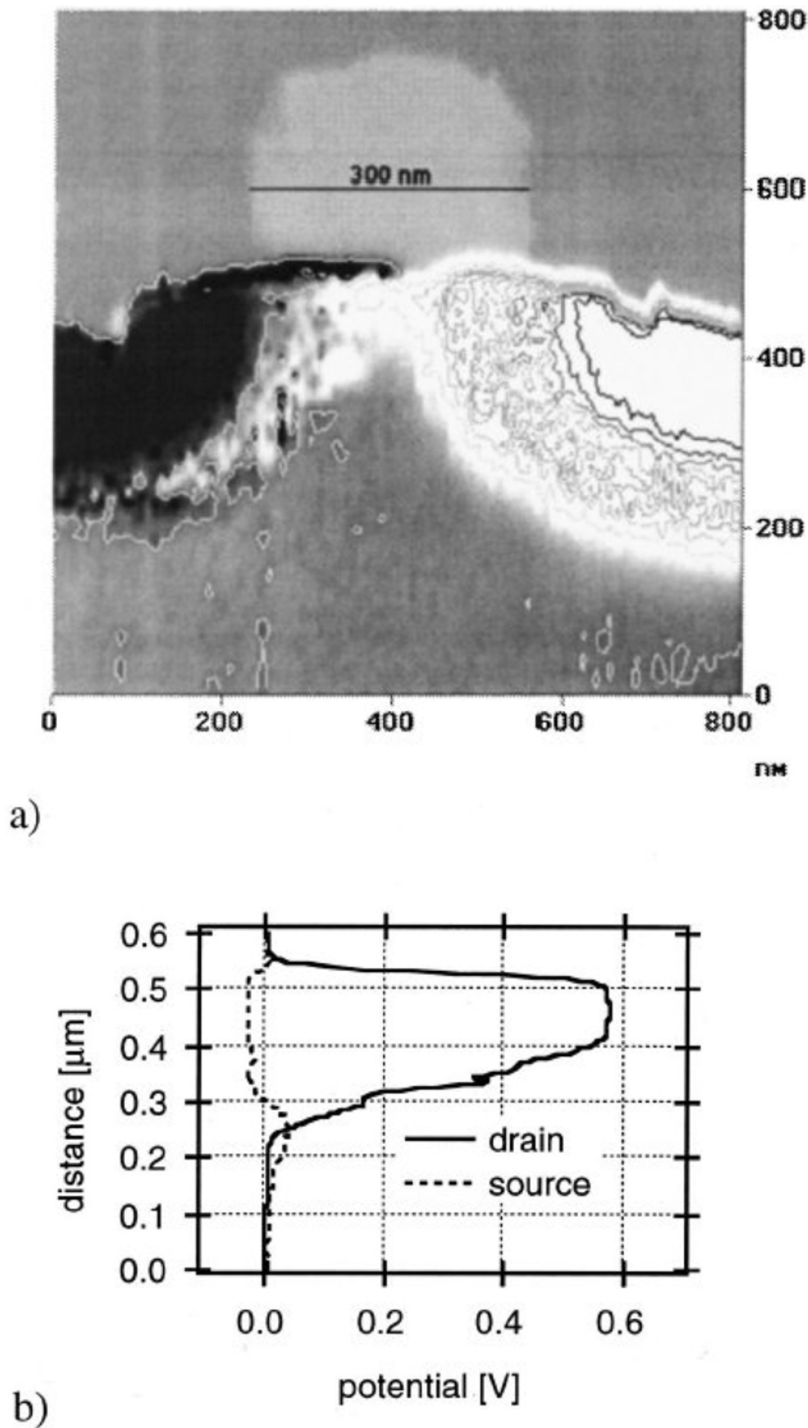

FIG. 24. (a) Potential distribution on a 300 nm N-MOS transistor. The black-to-white scale ranges from 0 to 1 V. The grounded source (dark) is at the left side, the gate (gray, at 0.5 V) is visible in the upper middle, and the drain (white, biased at 1.0 V) is at the right side. The isopotential lines inside the drain region indicate the potential gradients inside the drain. (b) Line section through the drain and source regions illustrating the detailed potential distribution across the depletion layer. (Reprinted with permission from Ref. 14, Copyright 2000, AVS The Science & Technology Society.)

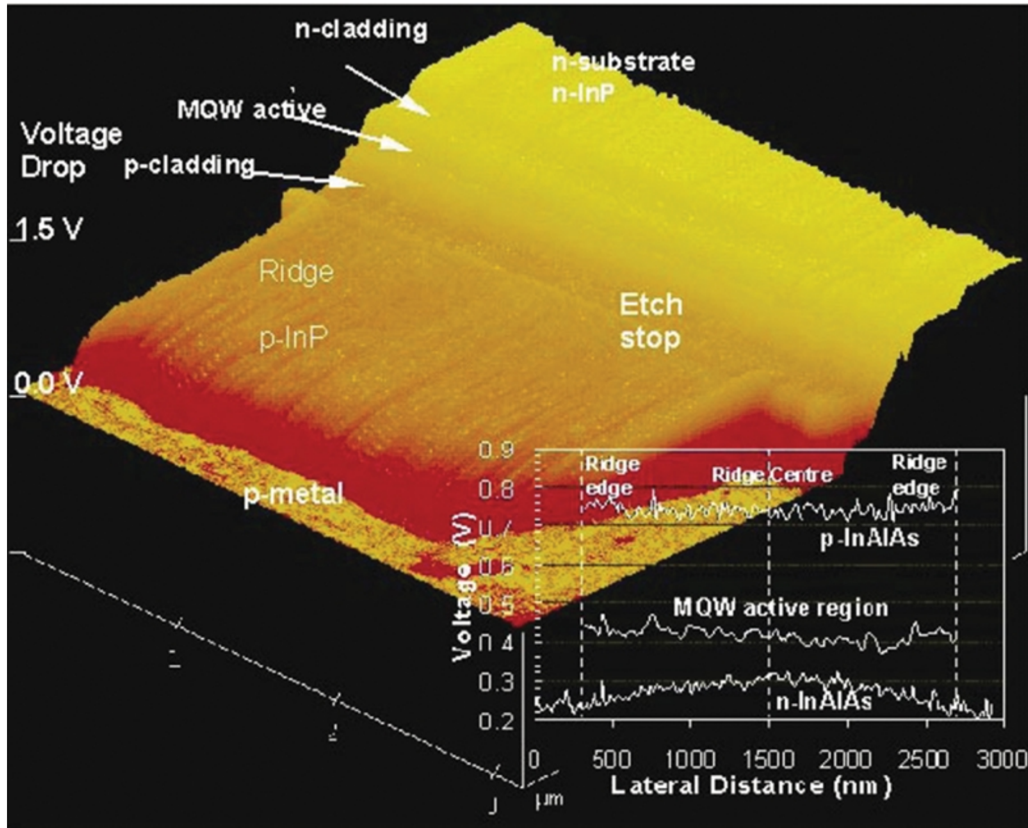

FIG. 25. (Color) 2-D local voltage drop image of the RWG laser in transverse cross-section. (Note: to display the measurement as clearly as possible, the voltage scale is inverted.) The laser was biased 40 mA above lasing threshold (a forward bias of 1.372 V). The inset shows the full lateral cross-sectional voltage profiles sampled in three vertical layers: n-InAlAs, MQW active region, and p-InAlAs. The n-InAlAs layer displays a nonuniform lateral voltage distribution. (Reprinted with permission from Ref. 72, Copyright 2003, American Institute of Physics.)

The result indicates that the local vertical current density at the edge is around 40% smaller than that at the center of the ridge. This may be compared with calculated results based on an analytical theoretical model for a similar laser structure,[62] which indicated that the lateral current spreading could be up to 42% for a 2 μm ridge width laser.

Buried Heterostructure Breakdown

Buried heterostructure lasers have low threshold currents and a stable fundamental transverse optical mode due to tight confinement of carriers and photons to an active region defined by the current-blocking structure. However, leakage current, which increases with increasing temperature and injection current, deteriorates the performance of the laser at high temperatures.[73] There are two major leakage current paths outside the active region: the diode leakage current and the thyristor leakage current.[74] Figure 26 shows a schematic diagram of the transverse cross-section of the BH laser and the possible leakage current paths.[75] Diode leakage current (I_{L1}) flows through the p-InP cladding layer, p-InP blocking layer, and n-InP substrate. Thyristor leakage current (I_{L2}) flows through the p-InP cladding layer, n-InP blocking layer, p-InP blocking layer, and n-InP substrate.

Investigations based on a simplified equivalent electrical circuit calculation show that the connection width (W_c), as defined in Figure 26, plays a key role in determining the current leakage.[73] Depletion regions between p- and n-doped InP layers near the active region–thyristor interface are crucial in funneling current into the active region. As the BH laser device is biased at a high injection current, a forward breakover of the current-blocking structures is often observed. It has been recognized to be an important factor that degrades the performance of a BH laser under high-current operation.[76] Previous experimental studies of the thyristor turn-on phenomena consist of characterization of external performance measurements such as light-current-voltage.[77]

Figure 27a shows the light-current-voltage (L–I–V) characteristics of a BH laser that exhibits breakdown of the current-blocking structure at a current injection of 270 mA. The applied

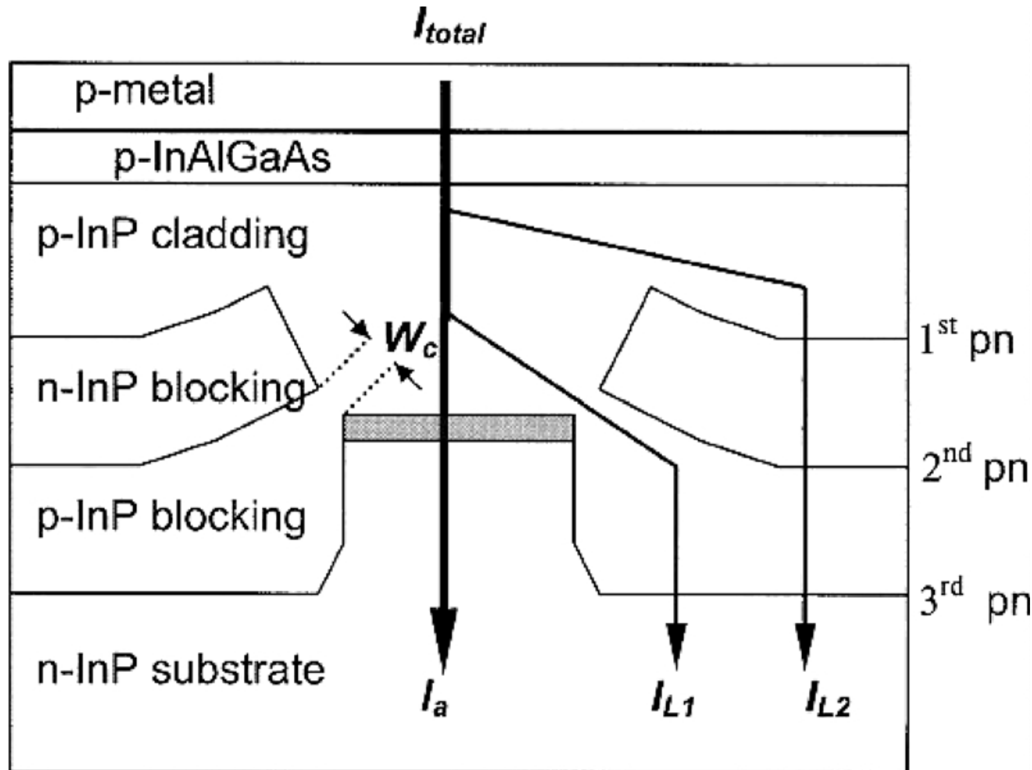

FIG. 26. Schematic transverse cross-sectional structure of a BH laser showing the possible current paths from p- to n-sides. W_c is the minimum distance between the active region (shadow area) and the n-InP blocking layer and is referred to as the connection width. (Reprinted with permission from Ref. 75, Copyright 2004, IEEE.)

voltage and the light output drop sharply as current injection rises above the breakdown point. This indicates that at least one current leakage path is turned on. A significant portion of the injected current bypasses the MQW active region. As a consequence, the applied voltage drops from 1.985 to 1.635 V and the optical output power degrades from 25.6 to 13.6 mW.

Figure 27b shows the hysteresis phenomenon in the breakdown of the structure. The current leakage path is turned on when increasing current injection to 270 mA and turned off when decreasing current injection to 170 mA. The I–V curves are repeatable with cycling, which indicates the breakdown of the current-blocking structure is not due to physical damage of the device.

Direct observation of the internal behavior in lasing devices is important to resolve conclusively where and how the breakdown of the failure to block current other than the active region occurs.

Figure 28 shows a two-dimensional voltage profile acquired under a DC forward bias of 0.845 V, which results in a current of 10.55 mA (above lasing threshold). The buried mesa is clearly resolved in the SVM image. The narrow strip at the left side of the mesa in the SVM image is the MQW active region, clad by p- and n-doped layers from the left and right. At the top are the p–n–p–n current-blocking structures. The accumulated voltage change from the p-metal to the n-doped substrate measured from the SVM is 0.844 V, in good agreement with the external voltage applied to the device. Voltage is nearly uniform over the n-doped regions due to the high electron mobility and doping concentration. Dips in voltage over the MQW active region and the second p-doped layer from the left side are observable.

The internal voltage profiles of the BH laser under the turn-on and turn-off states of the current leakage are measured using SVM. The SVM line scans are performed on the p–n–p–n region far from the mesa structure of the laser. The device is biased at the same current injection of 220 mA. The accumulative voltage difference between the two voltage curves is around 0.28 V. This agrees well with the difference in externally applied bias (~0.29 V, see Figure 27b) from the I–V curve measurements.

Figure 29 shows the cross-sectional analysis of voltage profiles along the diode leakage path depicted in Figure 26. An abrupt voltage change (~150 mV) at the p-InP cladding–p-InP blocking interface is observed when the diode leakage path is blocked. When it is turned on, the voltage profile varies smoothly across the interface.

The combination of thermal effects from active region heating and high electrical fields across the thyristor structures under high current injection is responsible for the observed current blocking failure. At high current injection, the temperature of

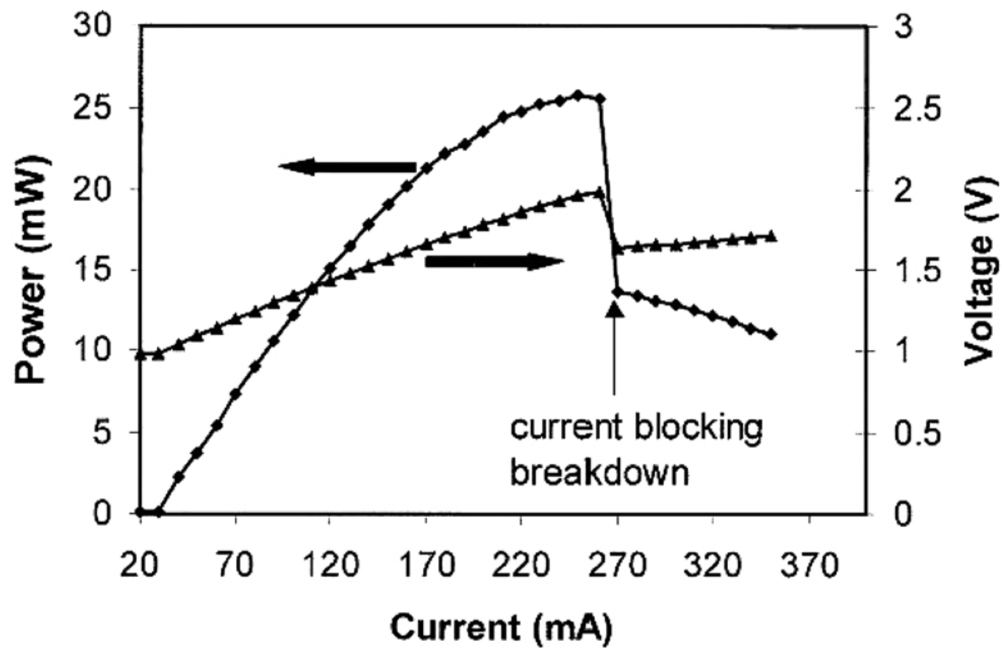

(a)

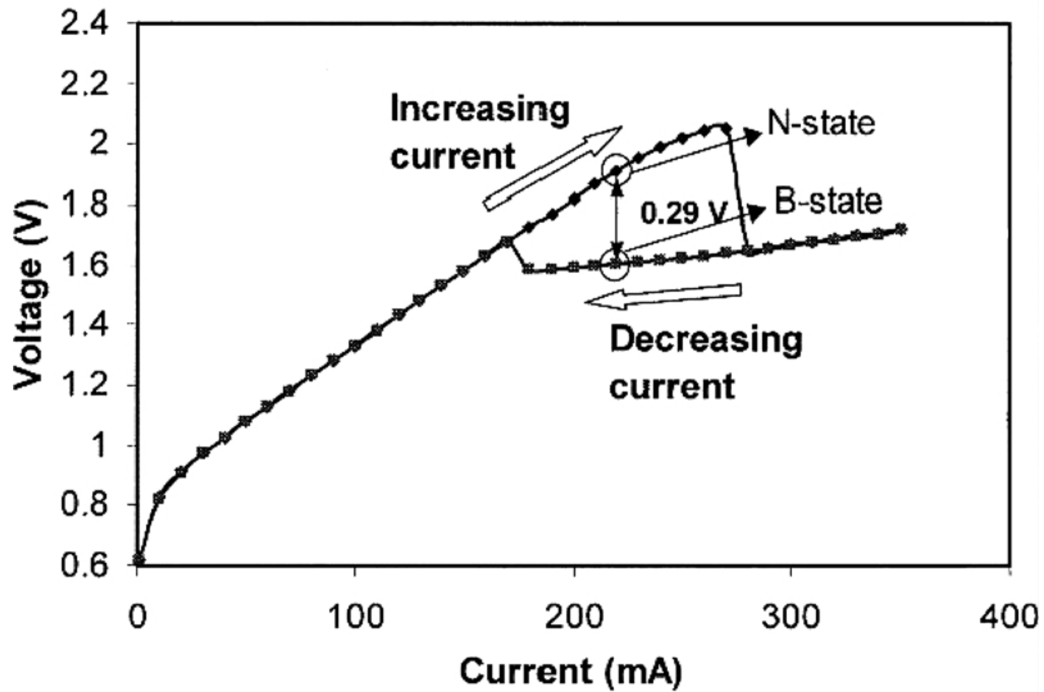

(b)

FIG. 27. (a) L–I–V curves of a typical BH laser that show the breakdown of current blocking, (b) I–V curves of the BH laser with cycling the current injection, showing the hysteresis behavior of the current blocking failure. The state in which the leakage current was turned on is denoted by B-state; the state in which the leakage current was turned off is denoted by N-state. (Reprinted with permission from Ref. 75, Copyright 2004, IEEE.)

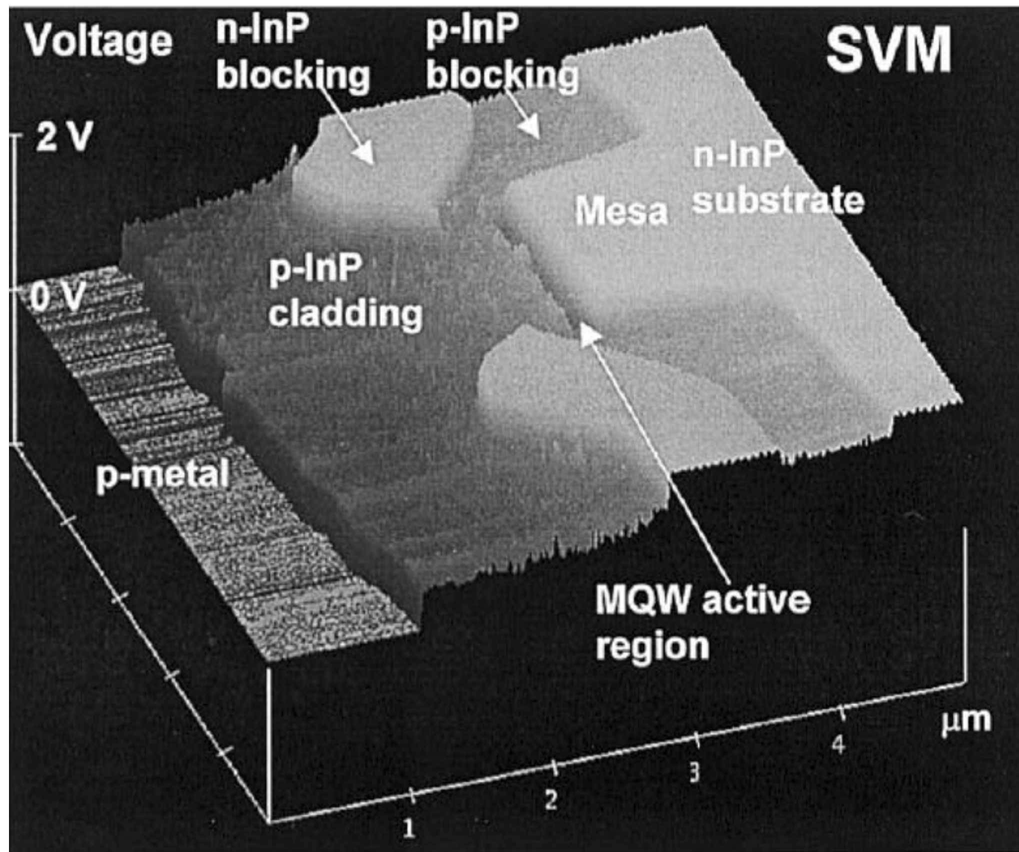

FIG. 28. Two-dimensional SVM image of a BH laser under forward bias of 0.92 V. The scan rate was 0.005 Hz. (Reprinted with permission from Ref. 75, Copyright 2004, IEEE.)

the active region as well as the neighboring *p–n–p–n* structures could be considerably higher than the heatsink temperature. The temperature increase gives rise to generation of more excess carriers in the intrinsic and/or depleted regions, which results in more current leakage. Elevated internal electrical field leads to increase of field emission or tunneling through the regions, where no current should flow through in an ideal situation. This also contributes to the increase of leakage current.

The SVM results could not provide direct insight into the physical reasons for the current blocking failure, that is, which is the dominant factor, the thermal effect or the high electrical field? However, the SVM results show direct experimental evidence for the turn on of the diode leakage rather than the thyristor leakage at high current injection.

Identification of Faulty Growth Interface

Scanning voltage microscopy has been employed to explore actively biased ridge waveguide lasers exhibiting anomalous current–voltage behavior—much-larger-than-expected voltage required for a given current. Conventional characterizations could not resolve the underlying origins of this observation. SVM analysis provides the nanoscopic clues as to the origins of the problem and point to the solution.

Series resistance is one of the key physical parameters controlling the external performance of semiconductor lasers. In particular, low series resistance is stringently required for high continuous-wave power operation in ridge waveguide (RWG) lasers.[60] Makino *et al.* studied the effects of series resistance and resultant heating at high powers and high temperatures[78]: series resistance and its temperature dependence are key determinants of the high-power performance of multi-quantum-well lasers.[79,80] Recently, Elenkrig *et al.* studied the temperature-dependent behavior of the series resistance, and, its relationships with laser properties such as threshold current and differential efficiency.[81]

As shown in Figure 30, the required voltage for a given current injection to the laser sample B is significantly higher than that of the laser sample A, even though they have nominally identical layer structures and geometric configuration. Sample A exhibits normal current–voltage behavior; the above-threshold differential series resistance of B is almost as twice as that of A.

SVM measurements were performed on both samples that were biased at an identical current injection of 100 mA.

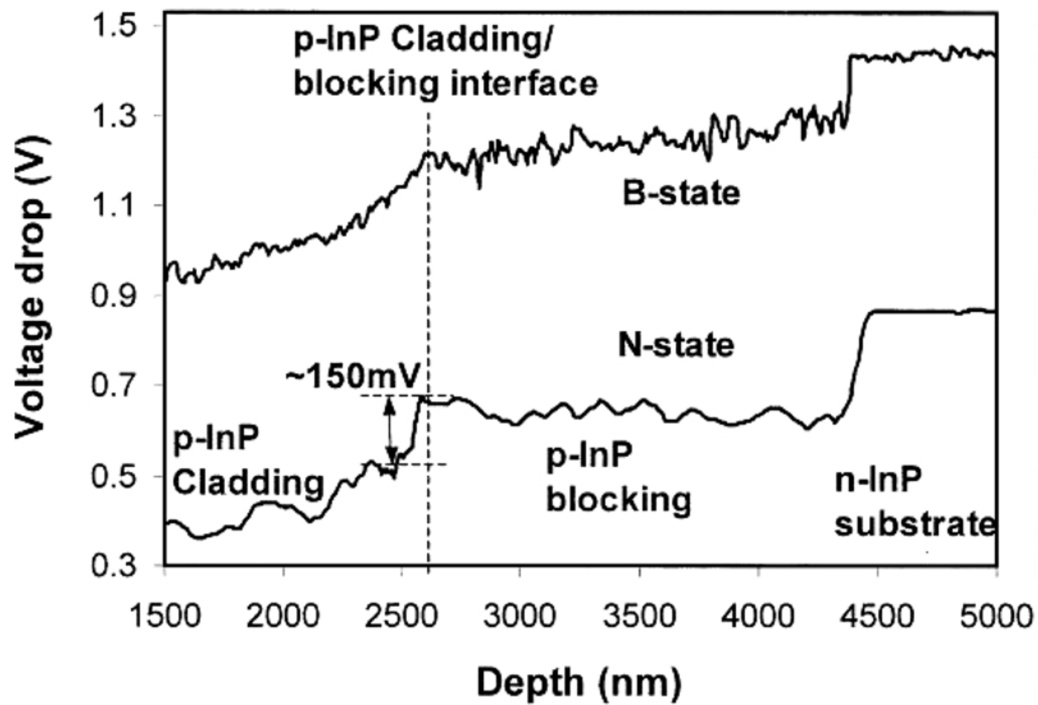

FIG. 29. Comparison of the cross-sectional voltage profiles along the p-InP cladding, p-InP blocking, and n-InP substrate (diode leakage path, L1) as outlined in Figure 26 when the laser was in the B-state and the N-state. (Reprinted with permission from Ref. 75, Copyright 2004, IEEE.)

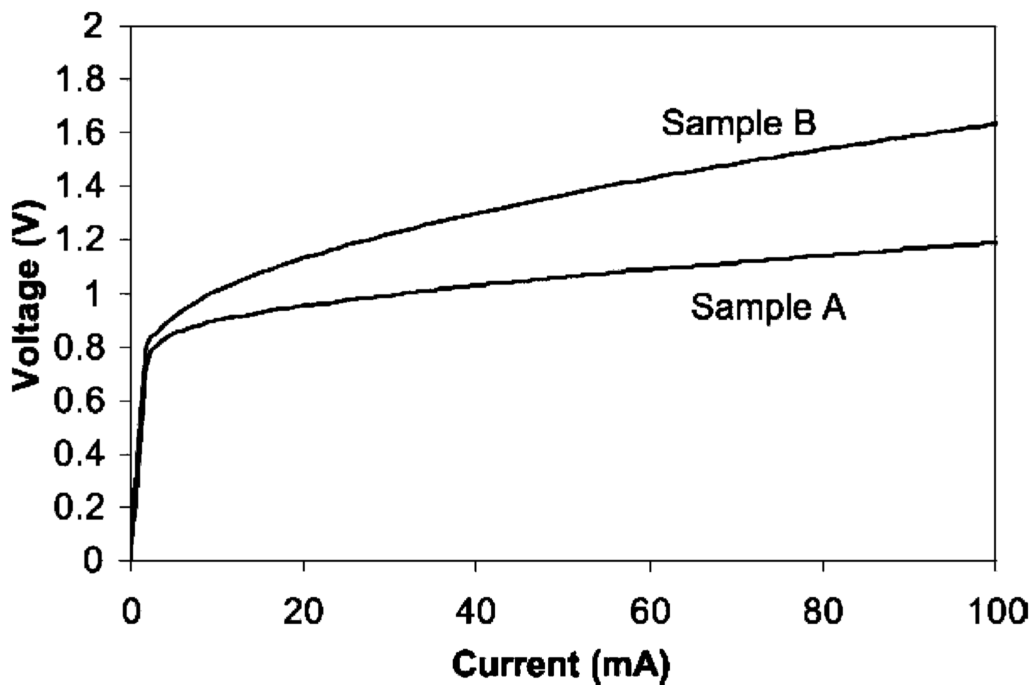

FIG. 30. Current–voltage curves of two RWG MQW lasers (samples A and B), showing different series resistances. Sample B has higher series resistance than sample A. (Reprinted with permission from Ref. 82, Copyright 2003, IEEE.)

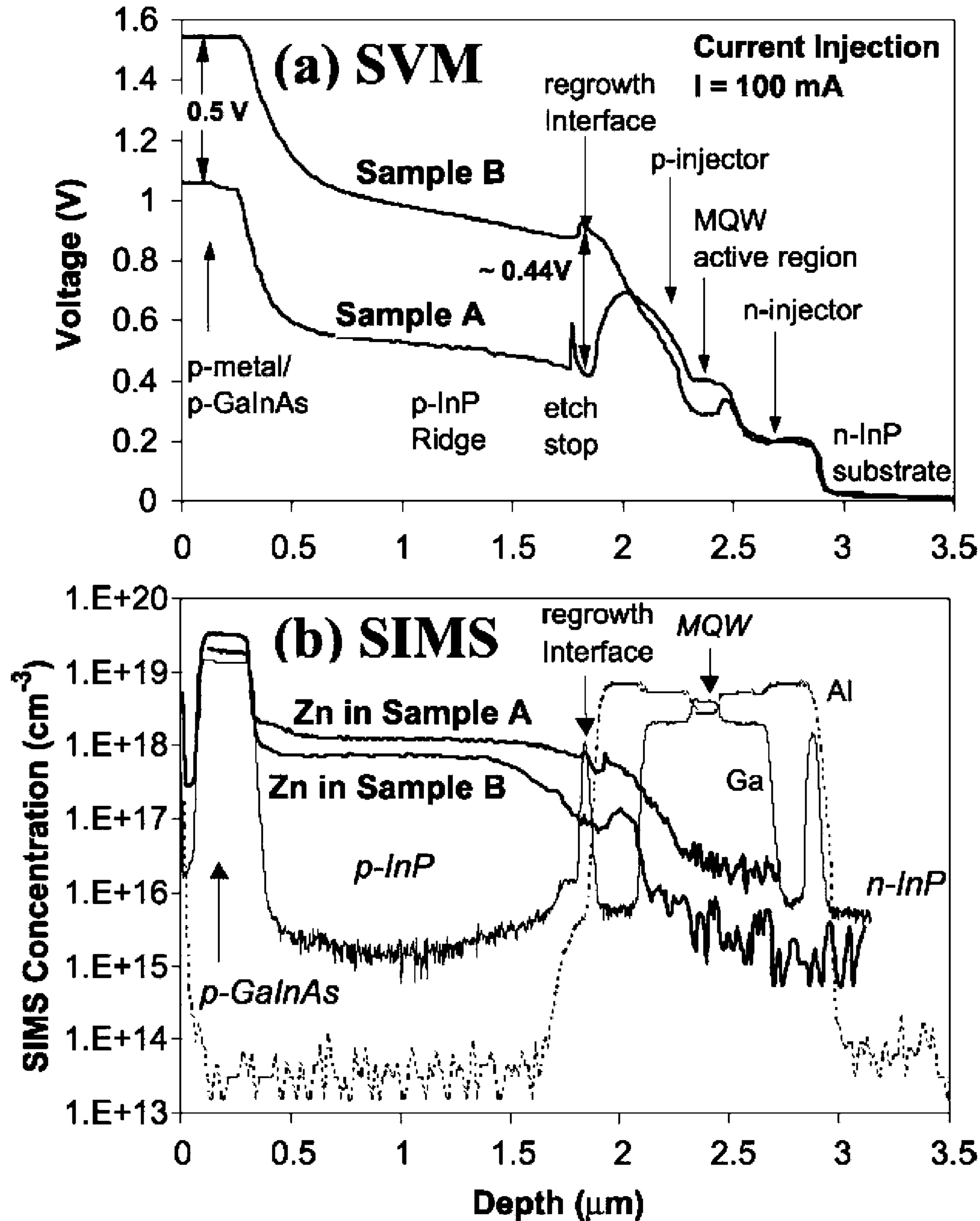

FIG. 31. (a) Cross-sectional SVM voltage distribution across the layer structure of the two RWG lasers, samples A (low resistance) and B (high resistance), under a forward current injection of 100 mA. Note that the total accumulative voltage difference of the two curves is around 0.5 V, about 90% occurring near the MBE-MOCVD growth interface region, (b) SIMS concentration of p-dopant (Zn) profiles in samples A and B. The sample A curve shows the targeted doping profile. Zn dopant concentration is lower in sample B near the MBE–MOCVD growth interface. (Reprinted with permission from Ref. 82, Copyright 2003, IEEE).

Cross-sectional SVM voltage profiles from the p-metal to the n-substrate of the two samples are plotted in Figure 31a. The two cross-sectional voltage profiles agree except at the regrowth interface. The voltage in sample B across the regrowth interface is 0.44 V larger than that in sample A, responsible for 88% of the total difference (0.5 V) of the external applied voltages.

Quality of the p-contact is of major concern in the electrical properties of a semiconductor laser device. The results of Figure 31a show no excess p-contact resistance in sample B compared to sample A and therefore exclude the possibility of a deteriorated p-contact in B.

These results prompted reexamination of any differences in growth and processing of these samples. The difference in series

resistance was discovered to be the result of the transition from molecular beam epitaxy to metal organic chemical vapor deposition growth. The p-injector layer, MQW active region, and n-injector layers in both samples were grown using MBE. The upper layer structures of the devices, including the etch stop and p-InP ridge definition, were grown using MOCVD.

In order to verify the conclusion drawn from the SVM data, second ion mass spectroscopy (SIMS) was performed on the laser samples. SIMS results show that the two samples had almost identical dopant profiles on n-side and the p-dopant profiles in the p-injector layer. Difference lay largely in the p-dopant profile at the p-ridge-p-injector interface, as shown in Figure 31b.

The concentration of element Zn (as p-dopant in InP) is the highest in the p-GaInAsP layer (for an ohmic contact); the concentration stays fairly flat within the p-InP region and drops to lower levels at a depth of around 1.5 μm. SIMS data show that Zn dopant concentration of the sample A is higher than that in B over all the regions of interest. The most remarkable difference occurs at the regrowth interface where Zn dopant concentration in sample B is smaller than that in sample A by almost one order of magnitude. Low dopant concentration gave rise to a high impedance region in which SVM revealed the significant voltage change to occur as an external bias was applied.

Elenkrig *etal*.[81] have shown that there are two contributions to the overall series resistance. One is due to the carrier transport over the heterobarriers and the other is from the semiconductor bulk resistance. The cross-sectional voltage profile in Figure 31a provides direct resolution of the two sources of the series resistance of the laser device. For example, the total voltage change from the p-metal to n-substrate in sample A is 1.05 V. A significant voltage change can be observed at several heterobarriers, including the p-metal-p-InP, MQW active region–n-injector and n-injector-n-substrate interfaces. Accumulative voltage change across the heterobarriers is 0.756 V, which contributes 72% of the total voltage across the entire structure.

Semiconductor bulk resistance (R_b), which accounts for only the bulk material resistivity of the layer structures in the laser devices, can be calculated using

$$R_b = \frac{V_t - V_h}{I}, \quad [32]$$

where V_t is the total voltage, V_h is the accumulative voltage change across the heterobarriers, and I is the current. Substituting the numbers of $V_t = 1.05$ V, $V_h = 0.756$ V in sample A and $I = 0.1$ A, the bulk resistance is $R_b = 2.94\,\Omega$.

This calculated result agrees well with the above-threshold differential series resistance (2.48 Ω) of sample A obtained from the slope of the voltage–current curve measurement (Figure 30).

Direct Measurement of *p*-type Contact Resistance

A source of self-heating is the p-type InP/InGaAs electric contact, normally not addressed in studies of laser optimization.[83–85] In order to be classified as ohmic, a contact must have a linear current–voltage characteristic, which generally implies good energy band alignment from one material to the next.[86] Ideally, the specific contact resistance $R_c = V/J$ should be $10^{-6}\ \Omega \cdot \mathrm{cm}^2$ or less. Metal/p-InP contacts are primarily nonohmic because the energy barrier from the metallic work function to the InP Fermi level is ∼0.8 eV,[87] leading to diode (Schottky) current–voltage behavior. In particular, holes face a significant energy barrier from metal to p-InP and their scattering causes joule heating of the device.

Much research during the last two decades[88–91] has focused on bridging metal (specifically non-corrosive gold) and p-InP ohmically, employing combinations and alloys of Au, Zn, Ni, Pd, Pt, Mn, Sb, W, and Ti to achieve reasonably linear I–V characteristics with $R_c \sim 10^{-5}\ \Omega \cdot \mathrm{cm}^2$.[87,92] Beyond the metallurgy of the metal–semiconductor junction, a buffer layer of highly doped InP-lattice-matched $In_{0.53}Ga_{0.47}As$ reduces the compound contact resistance,[93,94] although holes still must surmount an energy barrier at the p-InGaAs/p-InP heterojunction.

Contact resistance is normally measured by the test structure shown in Figure 32. In the first instance, current is passed from one electrode to the other via the InGaAs layer; the resistance measured is influenced by both the forward and reverse contacts of the structure. The InGaAs layer is then etched between the electrodes and the total resistance is measured for the combined contact to p-InP; again, there are forward and reverse heterojunctions in the current path. Additionally, minority electrons from vertical current leakage may influence the total resistivity of the real diode laser.[84] The conclusion must be that this is an *indirect* method used to infer the actual resistance of the heterojunction in a real device.

InP/InGaAsP laser chip samples emitting in the 1310 nm range and having 12 quantum wells were examined with SVM, with results shown in Figure 33. Dominating the voltage profiles—even at low voltage where the reverse photocurrent prevails—is the voltage drop across the p-type $In_{0.53}Ga_{0.47}$ As/InP heterojunction interface. Thermionic emission is expected to dominate[93] over tunneling because the barrier is relatively wide. As holes scatter at this barrier, they contribute phonons to the lattice, thereby heating the ridge and surrounding regions. The voltage drop measured by the SVM circuit reveals the change of the hole quasi-Fermi level under forward bias as predicted by the model developed earlier.

Dividing this voltage drop V_{het} by the total voltage drop across the device yields the fractional voltage drop, power loss and series resistance at the heterojunction,

$$\frac{V_{\mathrm{het}}}{V_{\mathrm{tot}}} = \frac{P_{\mathrm{het}}}{P_{\mathrm{tot}}} = \frac{R_{\mathrm{het}}}{R_{\mathrm{tot}}}, \quad [33]$$

plotted in Figure 34 for constant current bias. Primary uncertainty in the data arises from estimating the actual voltage of the p-type InP which is subject to noise. There is less significant uncertainty in the bias current and the voltage level of the InGaAs.

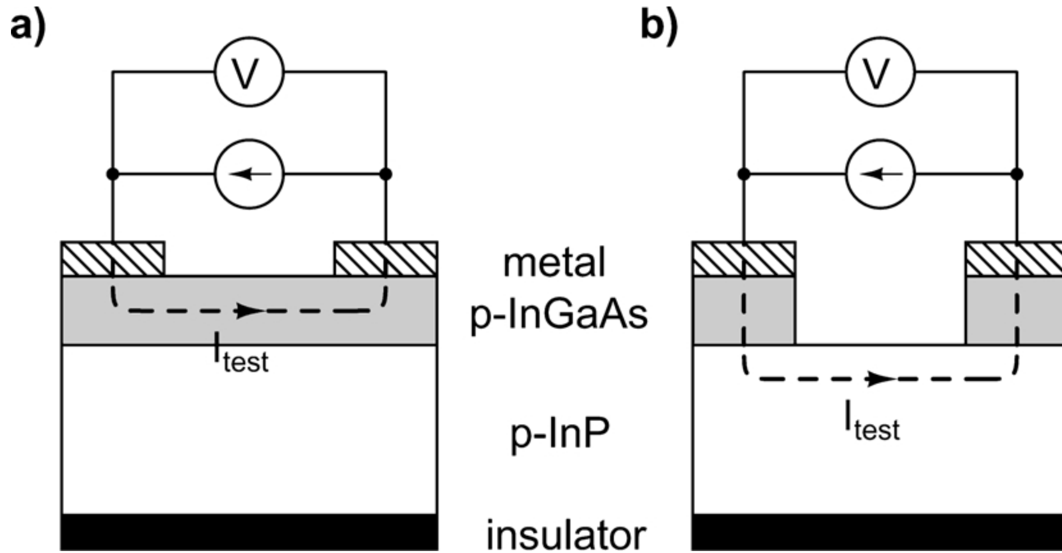

FIG. 32. Conventional method of measuring specific contact resistance of p-InP contact. (a) Measurement of the metal/p-InGaAs contact resistance, (b) The InGaAs between the electrodes is removed by etching, allowing the combined contact resistance to p-InP to be measured. In either case, the contact resistance for a *single* forward-biased metal/p-InGaAs/p-InP cannot be isolated from the combined system and must be inferred. (Reprinted with permission from Ref. 49, Copyright 2005, American Institute of Physics.)

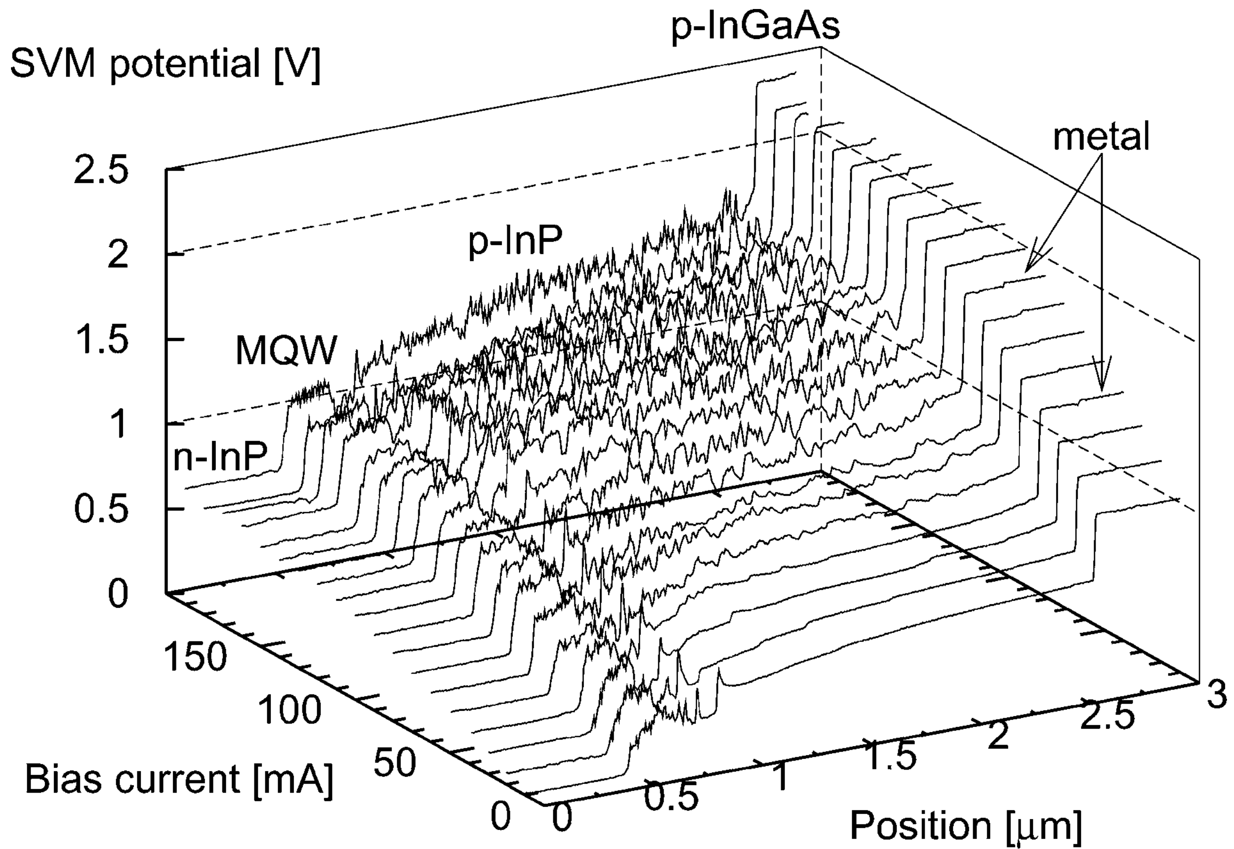

FIG. 33. SVM scans of wide-MQW RWG laser, 10 mA to 190 mA in 10 mA increments. The layer structure is indicated. Shot noise increases on p-type material due to the wide depletion region at the tip–sample interface at high bias. (Reprinted with permission from Ref. 49, Copyright 2005, American Institute of Physics.)

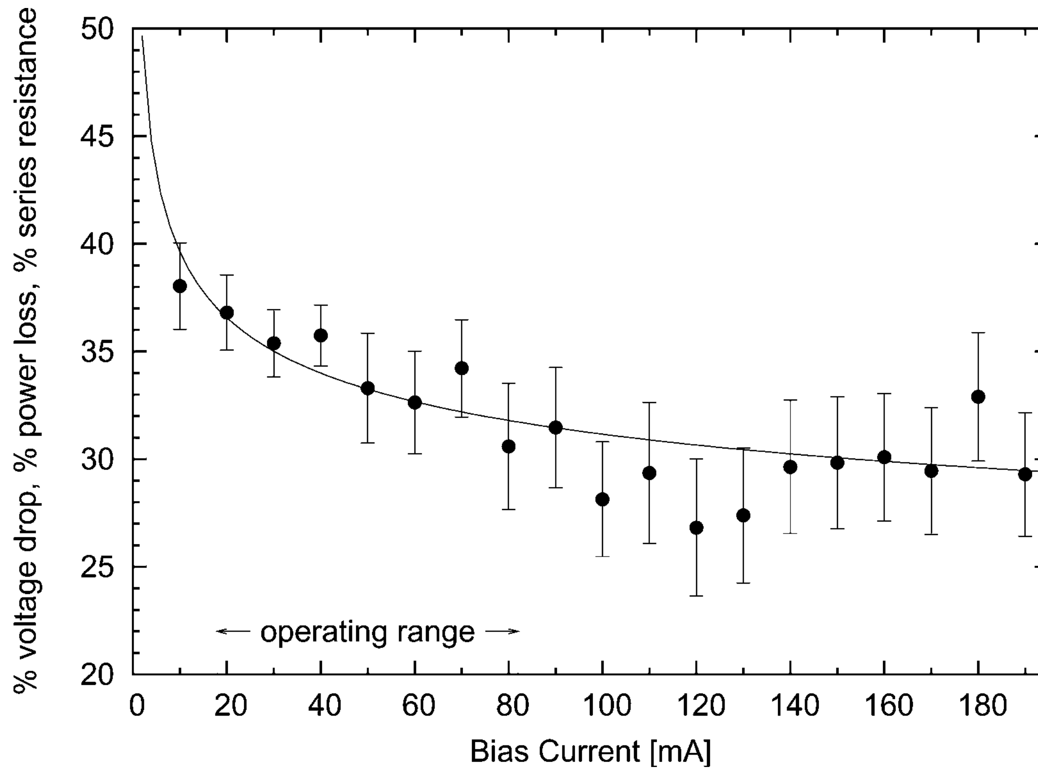

FIG. 34. Fractional parasitic voltage drop (power loss, series resistance) of p-InP/p-$In_{0.53}Ga_{0.47}As$ heterojunction. The average value is 35% over the operating range. (Reprinted with permission from Ref. 49, Copyright 2005, American Institute of Physics.

It is striking that over the normal operating range of this laser (20–80 mA), approximately 35% of the wallplug power is lost before it ever reaches the active region. Clearly, from the SVM profiles the $In_{0.53}Ga_{0.47}As$ layer yields a flat, relatively lossless contact with the metal. However, a highly nonohmic contact is formed subsequently with the InP ridge, degrading performance and wallplug efficiency. The specific contact resistance of this interface is a dismal $\sim(10\,\Omega)(2\,\mu\text{m})(300\,\mu\text{m}) = 6\times10^{-5}\,\Omega\cdot\text{cm}^2$ (the product of resistance and transverse cross-sectional area), nearly two orders of magnitude greater than the metal/p-InGaAs contact.

SOURCES OF SVM ARTIFACTS

SVM, like all AFM and scanning probe techniques, is subject to measurement artifacts. If SVM is to be used to analyze nanometer-sized structures in a reliable, repeatable manner, it is critically important to identify and evaluate sources of artifact.

Influence of Scan Speed on Maximum Spatial Resolution

Qualitative differences in two-dimensional SVM potential maps have been noted depending on scan direction (to higher or lower sample potential) and material doping type (n- or p-type). In the direction that tracks increasing sample potential, abrupt interfaces between adjacent material layers are more clearly delineated than those in the decreasing-potential scan direction. Images taken in decreasing-potential direction are notably more smeared, particularly over p-type InP.

In one calibration experiment, a conductive AFM tip was scanned over the alternating p–n–p–n current blocking layers (nominal doping of 10^{18} cm^{-3}) of a DC-biased buried heterostructure laser at various scan rates to observe hysteresis between the forward and reverse electric potential scans.

512 samples were captured along 5 μm scans giving approximately 10 nm resolution limited ideally by the tip radius. Direct comparison of potential profiles in Figure 35 reveals hysteresis between the different directional scans: the forward scan (left to right) tracks closely the abrupt increasing potential changes from layer to layer and is relatively invariant to scan speed whereas the reverse scan (right to left) converges to abrupt decreasing potential changes only for the slowest scan speed shown (0.1 μm/s). Exponential time constants were estimated from these results: time constants on p-type InP are an order of magnitude slower than those on n-type InP; on p-type InP the average time constant for the decreasing potential scan direction is several times slower than that for the increasing potential scan direction. Noise becomes apparent only during the slowest scan (see Figure 35d).

In a second calibration experiment, the SVM setup was modified: 50% duty-cycle square-wave bias was supplied to the BH laser and the potential output from the stationary AFM tip was captured on an oscilloscope via the voltmeter preamplifier output port (see Figure 36). A similar set-up was used by Trenkler

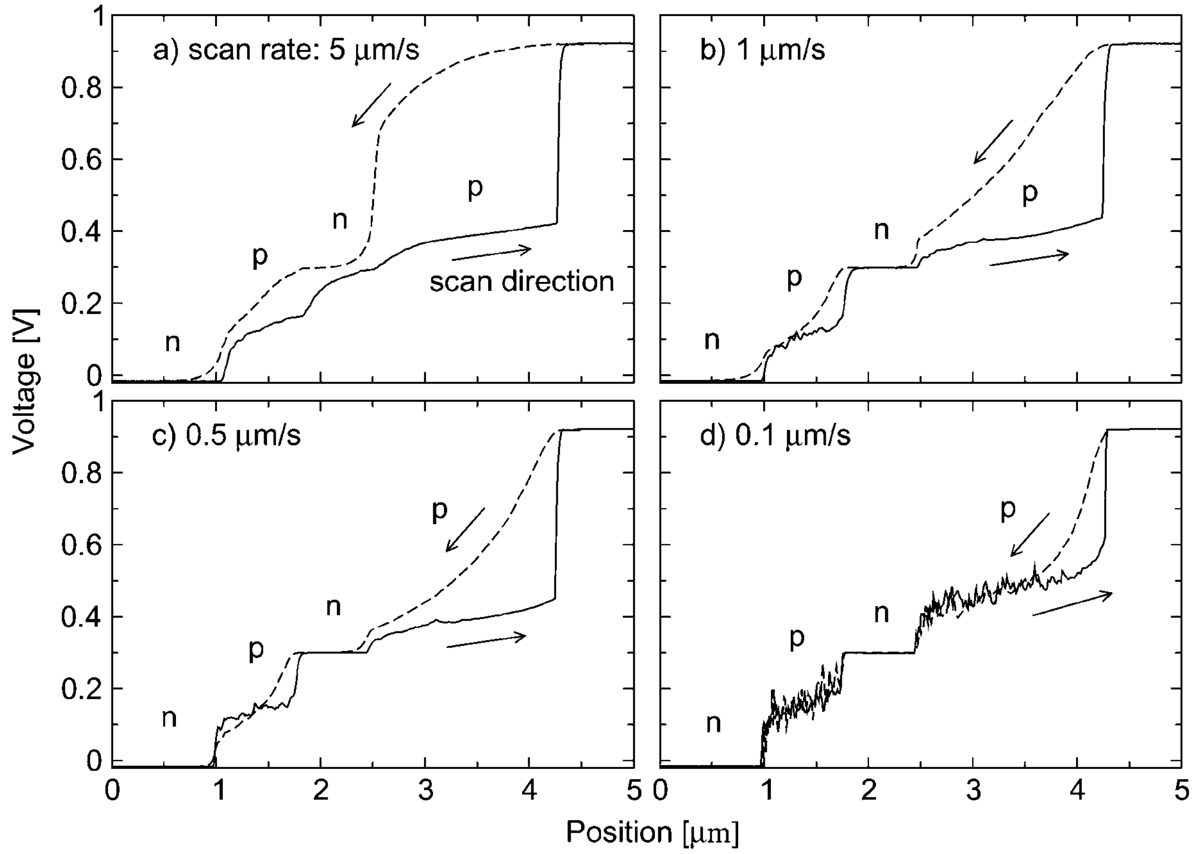

FIG. 35. Electric potential cross-sections of the p–n–p–n blocking layers of a forward-biased buried heterostructure laser (arrows show spatial scan direction of probe). Significant hysteresis is observed between increasing (left to right) and decreasing (right to left) electric potential scans on p-type material at faster scan rates (a) 0.5 Hz, (b) 0.1 Hz, and (c) 0.05 Hz. At the slowest scan rate of 0.01 Hz (d) steady-state has been reached and the hysteresis is reduced acceptably; shot noise is observed at this speed because otherwise dominant probe–sample steady-state-approaching currents have subsided. (Reprinted with permission from Ref. 56, Copyright 2004, American Institute of Physics.)

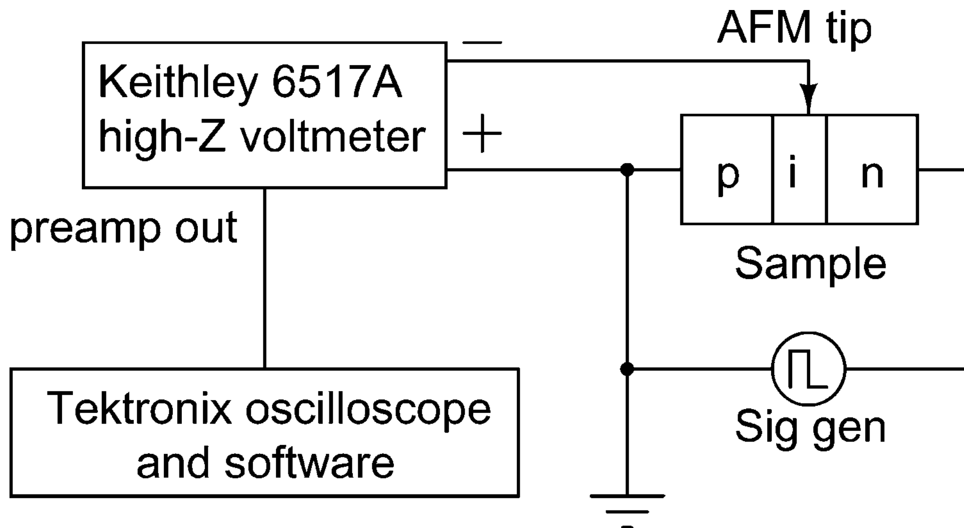

FIG. 36. SVM setup modified for time-resolved measurements: the current source is replaced with a square-pulse signal generator and the output of the voltmeter is directed to an oscilloscope to capture the impulse response of the SVM measurement circuit.

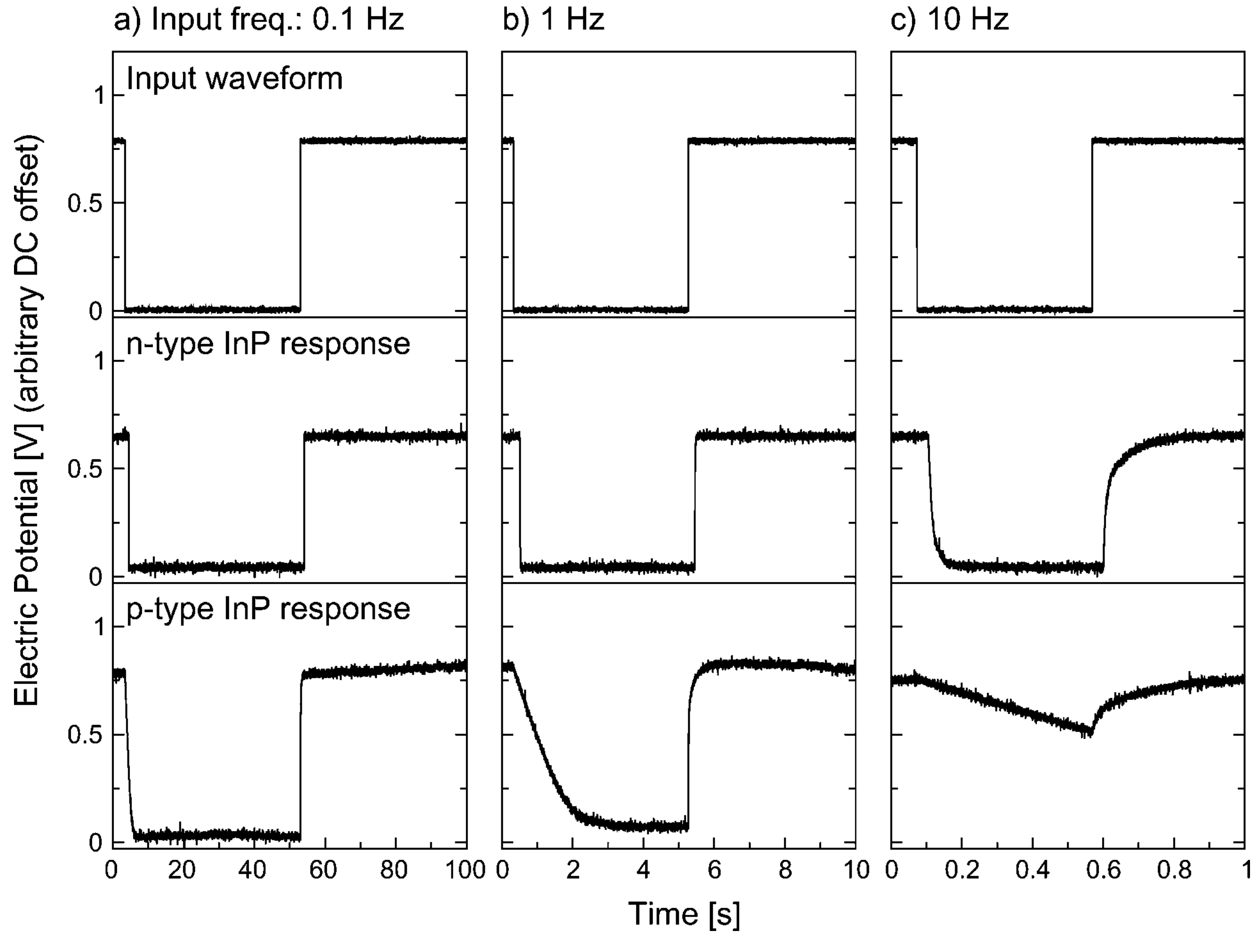

FIG. 37. Step response of the scanning voltage microscopy measurement circuit on buried heterostructure laser: input waveform (above), n-type response (middle) and p-type response (below), InP material 10^{18} cm^{-3} nominal doping, biased with square waves at (a) 0.1 Hz, (b) 1 Hz, and (c) 10 Hz. Faster impulse response of n-type InP is observed. (Reprinted with permission from Ref. 56, Copyright 2004, American Institute of Physics.)

et al.[14] to characterize SVM probes. Figure 37 shows the step response for n- and p-type InP of the BH laser for increasing bias frequency. Again, time constants for p-type InP are an order of magnitude slower than those on n-type InP and tracking decreasing potential is several times slower than tracking increasing potential. At 10 Hz input frequency (Figure 37c), the p-type response shows the effects of severe low pass filtering. The voltmeter was isolated and found to have a frequency response many orders of magnitude higher than that of the tip–sample interface shown in Figures 35 and 37.

The response shown in Figure 37 is characteristic of a low pass filter. The source of the high contact resistance can be traced to the formation of a Schottky barrier at the tip–sample interface. The diamond grain coating of the AFM tip is doped sufficiently heavily with boron that it is appropriate to model the tip material as a metal[8] with Fermi level $\mathcal{E}_{Fm}$ at the work function energy near 4 eV below vacuum.[7,95] At the surface of the biased semiconductor laser, the quasi-Fermi levels ϕ_n and ϕ_p must converge as shown in Figure 19a for both n- and p-type InP. The electron affinity of InP is 4.38 eV below vacuum; the band gap energy between conduction band edge $\mathcal{E}_c$ and valence band edge $\mathcal{E}_v$ is 1.34 eV.[96] The process of approaching steady-state at the tip–sample interface takes place as charge is transfered between tip and sample to align the Fermi level of the tip and the convergence point of the quasi-Fermi levels of the sample. A depletion region arises in the sample as the pinned energy bands bend, leading to the formation of a Schottky barrier[86] Φ_B as shown in Figure 19b.

Two conduction mechanisms are possible for electrons to cross the Schottky barrier: thermionic emission and tunneling. For a semiconductor of light to moderate doping concentration, thermionic emission dominates[86] and the contact resistance r_c is given by

$$r_c = \frac{k_B T}{q A^* T^2} \exp\left(\frac{\Phi_B}{k_B T}\right), \quad [34]$$

where A^* is the effective Richardson constant for thermionic emission, $A^* = 4\pi q m^* k_B^2/h^3$. If the semiconductor is heavily doped, tunneling dominates, and the contact resistance is proportional to

$$r_c \propto \exp\left(\frac{2}{\hbar}\Phi_B\sqrt{\frac{\epsilon_s m^*}{\hbar N}}\right), \quad [35]$$

where ϵ_s is the dielectric constant, m^* is the appropriate effective mass, and N is the doping concentration. Typical doping concentrations for semiconductor lasers span the range from light to heavy, but regardless, contact resistance at the interface depends exponentially on the barrier height.

Because the bandstructure of p-type InP gives rise to a larger barrier, its contact resistance must be substantially higher than that for n-type InP. Furthermore, the greater depletion of carriers across the interface in the p-type case further slows the approach to steady-state. Noise resulting from fluctuations in current at the interface appears at the slowest scan rate in Figure 35d because the system has come to reasonable steady-state and charge transfer is no longer dominated by Fermi level alignment-induced current. (The dominant source of noise is random thermal generation of electron-hole pairs that are then swept to opposite sides.[52] Shot noise is generated across the depletion region width—the wider the depletion region, the greater the shot noise; thus, more noise appears on p-type material.) With the parasitic capacitance of the measurement circuit fixed, the time-to-steady-state varies only with this contact resistance.

Approaching steady-state for decreasing sample potential is notably slower (particularly on p-type InP) because the barrier Φ_B and contact resistance increase for a lower convergence point of the quasi-Fermi levels, whereas approaching a higher steady-state potential decreases the barrier and contact resistance. More importantly, scanning from lower to higher potential shrinks the depletion region, allowing more carriers to be transported across the interface and accelerating the steady-state process; scanning from higher to lower potential has just the opposite effect—carriers become increasingly sparse as the depletion region expands. Therefore, there is a preferential scanning direction in terms of frequency response from lower to higher sample potential.

To allow the probe–sample interface to reach steady-state for each electric potential location at a desired spatial resolution d, the scan speed of the tip v must be limited such that

$$v < \frac{d}{5\tau}, \quad [36]$$

where τ is the longest time constant encountered on a given scan (according to material type and whether potential is increasing or decreasing); after five time constants the tip is considered to be at steady-steady with the sample with less than 1% error ($e^{-5} = 0.007$; it is common[97] to take five or six time constants in asymptotic approximation). For example, at $v = 0.5$ μm/s, roughly 50 samples/s can be captured accurately at a resolution of 10 nm on n-type InP because each sample has 0.05 s to reach steady-state as shown in Figure 35c. The time required to reach tip–sample steady-steady is shorter for scans in which increasing potential is measured so that v may be increased if scans in the direction of decreasing potential are discarded.

These results apply generally to a wide variety of semiconductors. The band gaps for common semiconductors—including band gap ranges for ternary and quaternary materials—are plotted in Figure 38. All have similar bandstructures relative to the CVD diamond tip workfunction and so p-type material will always form the greatest Schottky barrier and limit the scan speed.

For accurate measurements, the SVM scan speed must be limited by the ratio of spatial resolution to slowest time required to reach steady-state. There is a preferential scanning direction in terms of frequency response from lower to higher sample potential due to the asymmetry of the Schottky junction. Using diamond tips on InP and other common semiconductors, measuring n-doped regions will always be faster (and less noisy) than measuring p-doped, and measuring from low-to-high potential will be faster.

Effect of Optical Lever Laser at Low Device Bias

A constant voltage source replaced the constant current source to reduce the bias voltage below the turn-on value, as illustrated in the schematic Figure 39 (with a constant current source, the diode voltage immediately assumes a value of ~0.5 V). 3 μm line scans with 512 samples per line were obtained as before.

It is interesting to note that for bias voltages below 0.49 V in Figure 40, the p-type SVM voltage dips *below* 0 V. Even at a bias voltage of 0 V with the device terminals shorted together, the SVM voltage remains rooted firmly below zero, even after two hours of continuous scanning to discount stored-charge processes.

In fact, the laser is not at equilibrium: the laser light from the AFM optical lever not reflected by the tip is absorbed by the sample laser, which in turn produces a reverse photocurrent, demonstrated in Figure 39 and revealed in the I–V characteristic of Figure 41. Although SVM scans cannot be performed without the AFM laser activated (deflection feedback is necessary), the short-circuit photocurrent vanishes when the AFM laser is removed (see Figure 41 inset). The wavelength of the AFM laser is 670 nm, well above the 1310 nm bandgap of the sample laser, and the output power is 1 mW before reflection off the tip, a significant portion of which is not reflected to the photodetector.

At bias points above 0.49 V, the bias current (~mA) washes out the photocurrent (~μA) and all effects due to the AFM laser can be completely neglected. At bias points below 0.49 V where the SVM traces begin to dip below 0 V, the photocurrent is comparable to the external bias current as shown in the inset of Figure 41 (both ~μA), and so its effect must be considered.

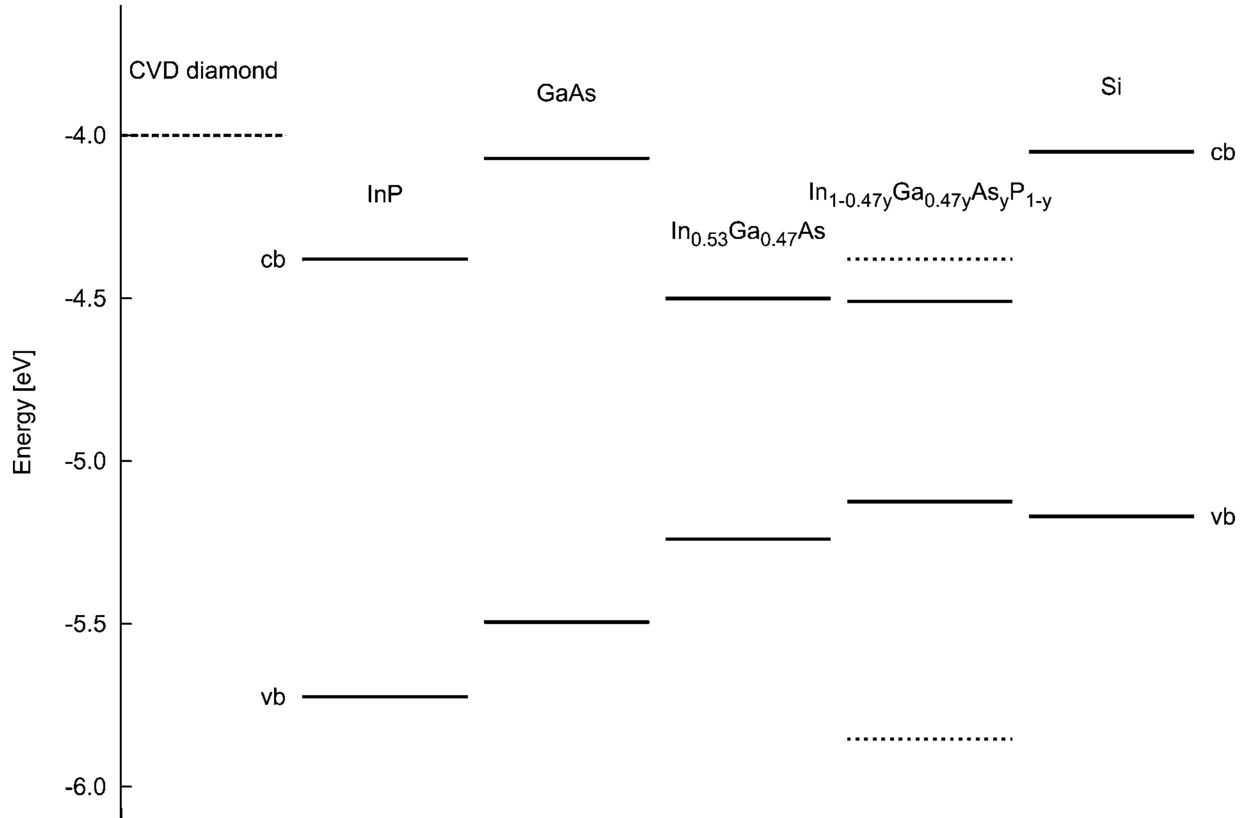

FIG. 38. Comparison between the metallic Fermi level of CVD diamond and the conduction (top solid line) and valence (bottom solid line) bands of common semiconductors; the range of conduction and valence band energies of InGaAsP lattice-matched to InP is shown by upper and lower dashed lines.

Thus, when the bias is set to 0 V, the sample laser is not actually at equilibrium and is rather acting as a photovoltaic diode.

SCANNING DIFFERENTIAL SPREADING RESISTANCE MICROSCOPY

The measured voltage in SVM comprises two parts: a change of electrostatic potential and a change of free carrier concentration upon the application of external biases. Contribution from the change of free carrier concentration cannot be neglected over the active region in a laser diode, particularly when the device is biased above the lasing threshold. It is therefore important to measure free carrier density distribution independently in order to separate the two effects in SVM measurements.

By its own right, carrier transport and distribution is of major interest in multi-quantum-well (MQW) lasers.[99] The injection of carriers into the QWs profoundly affects the performance of the devices. The physical parameters involved include efficiency and optical modal gain,[100] current leakage,[101] threshold current,[102] modulation bandwidth, and wavelength chirp under direct modulation.[103] Prior experimental work consists mostly of carrier-lifetime measurements using time-resolved photoluminescence experiments[104,105] and modulation response measurements.[106,107]

The SSRM technique resolves free carrier distribution within a semiconductor device but only at equilibrium.[17,18,23] The present authors describe a technique they call scanning differential spreading resistance microscopy (SDSRM). SDSRM is used to investigate the free carrier distribution inside a BH MQW laser under both zero bias and forward biases. Individual quantum well–barrier periods can be resolved with high-resolution SDSRM. The results provided the first direct experimental observation of overbarrier electron leakage in BH lasers operating at room temperature.

SDSRM Circuit and Interpretation

The obstacle in measuring the free carrier density electrically inside an operating device is in separating the informative electrical signal from the device bias voltage. It is necessary to filter out the impact of the device bias on the measurements; perturbations to device operation due to the measurements must be minimized to a negligible level. Separating the measuring circuit is achieved from the biasing circuit by means of lock-in techniques. This technical solution leads to the prototype of a new scanning probe microscope technique: scanning differential spreading resistance microscopy, SDSRM.

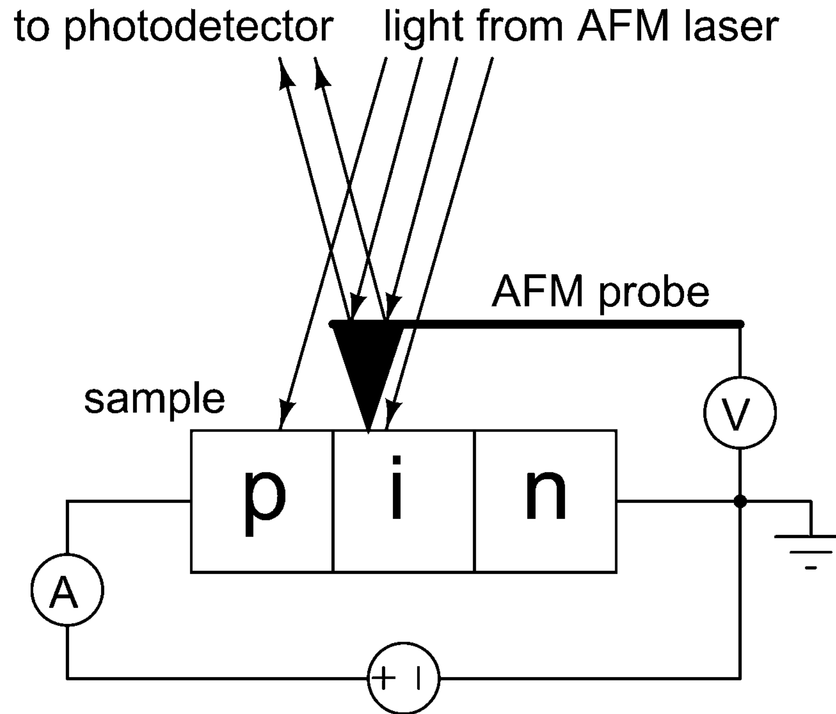

FIG. 39. Schematic of scanning voltage microscopy realized using an atomic force microscope with a conductive probe tip. The probe measures the voltage of an actively biased sample. (Size of the probe is exaggerated for illustration.) Some laser light from the "optical lever" bypasses the end of the probe and is absorbed by the sample. (Reproduced from Ref. 98)

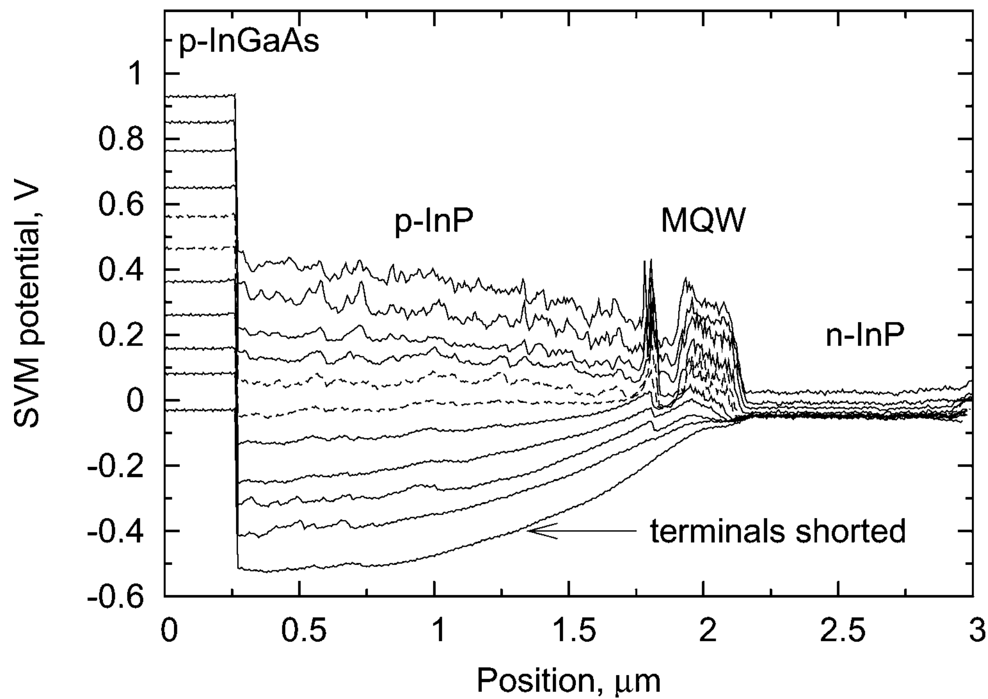

FIG. 40. SVM scans of wide-MQW RWG laser at low bias voltage. Below a bias voltage of 0.49 V, the SVM potential dips below 0 V; this is due to reverse photocurrent induced by the AFM laser (i.e., of the optical lever), insignificant at higher bias points. (Reproduced from Ref. 98)

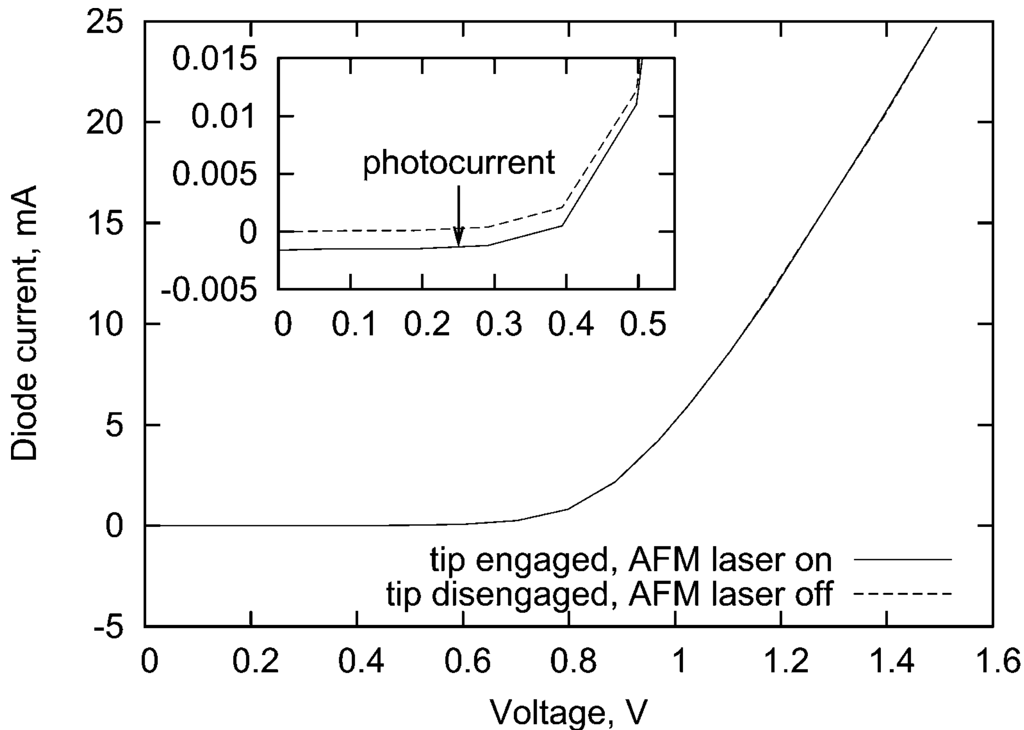

FIG. 41. Evidence of reverse photocurrent effects at low sample voltage. Below 0.49 V bias, the photocurrent contends with the bias current (inset). When the AFM laser is deactivated, the photocurrent vanishes. (Reproduced from Ref. 98).

SDSRM eliminates the requirement of zero device bias by separating the measuring circuit from the biasing circuit via the frequency domain. As shown in Figure 42, a DC voltage is applied to the input ends of the device under test for biasing, and an AC voltage is applied between the conductive AFM tip and the cross-sectional surface of the sample for measuring.

A capacitor is connected in series with the AFM tip in the measuring circuit to screen the DC bias voltage. The AC voltage is set sufficiently low (typically 0.1–0.3 V peak-to-peak) to minimize its impact on the biasing circuit. The contact resistance between the AFM tip and semiconductor surface is in the range of 10^6–10^9 Ω; this is six to nine orders of magnitude larger than the bulk series resistance and the contact resistances on *p*- and *n*-sides of the semiconductor laser (typically less than 10 Ω in total). Consequently, the vast majority of the AC voltage drops across the contact between the AFM tip and semiconductor surface. Voltage perturbation on device bias due the application of the AC voltage is on the order of 1 μV and its influence on device operation is negligible. The resultant AC current flowing into the sample surface in the measuring circuit (typically below 1 μA) is measured using a lock-in amplifier system.

The resultant AC current is evaluated by monitoring the AC voltage drop across a reference resistance, measured by the lock-in amplifier and acquired by the AFM computer via a signal access module. The differential spreading resistance sensed by the AFM tip is then derived from the measured AC signal in post-processing.

Presuming an ohmic contact between the tip and the semiconductor surface and an ideal semi-infinite uniformly doped semiconductor, the differential spreading resistance R_d of a non-penetrating ohmic contact of radius a is given by

$$R_d = \frac{\rho}{4a} = \frac{1}{4\sigma a} \qquad [37]$$

where ρ is the resistivity and the conductivity σ is equal to $qn\mu$, (q the electron charge, n is the local free carrier density, and μ the carrier mobility). Measured differential spreading resistance is therefore inversely proportional to the free carrier concentration of the sample via $R_d \propto 1/\sigma \propto 1/n$. However, variations in the tip–surface contact resistance in some certain circumstance, that is, the non-ohmic behaviors of the tip–semiconductor interface,[18] may cause deviation of the real measurements from the prediction in Eq. 37.

SDSRM Analysis of Electron Over-Barrier Leakage in Semiconductor Diode Lasers

A specific issue in carrier transport—electron overbarrier leakage from a laser active region—has been widely recognized in long wavelength InGaAsP-InP laser diodes.[84,101,109] Both experimental and theoretical investigations have pointed to electron thermionic emission into the *p*-injector as a possible cause of the strong temperature dependence of laser performance. It has been proposed to use a larger-bandgap *p*-AlGaAs cladding layer instead of *p*-InP to suppress electron leakage out of the

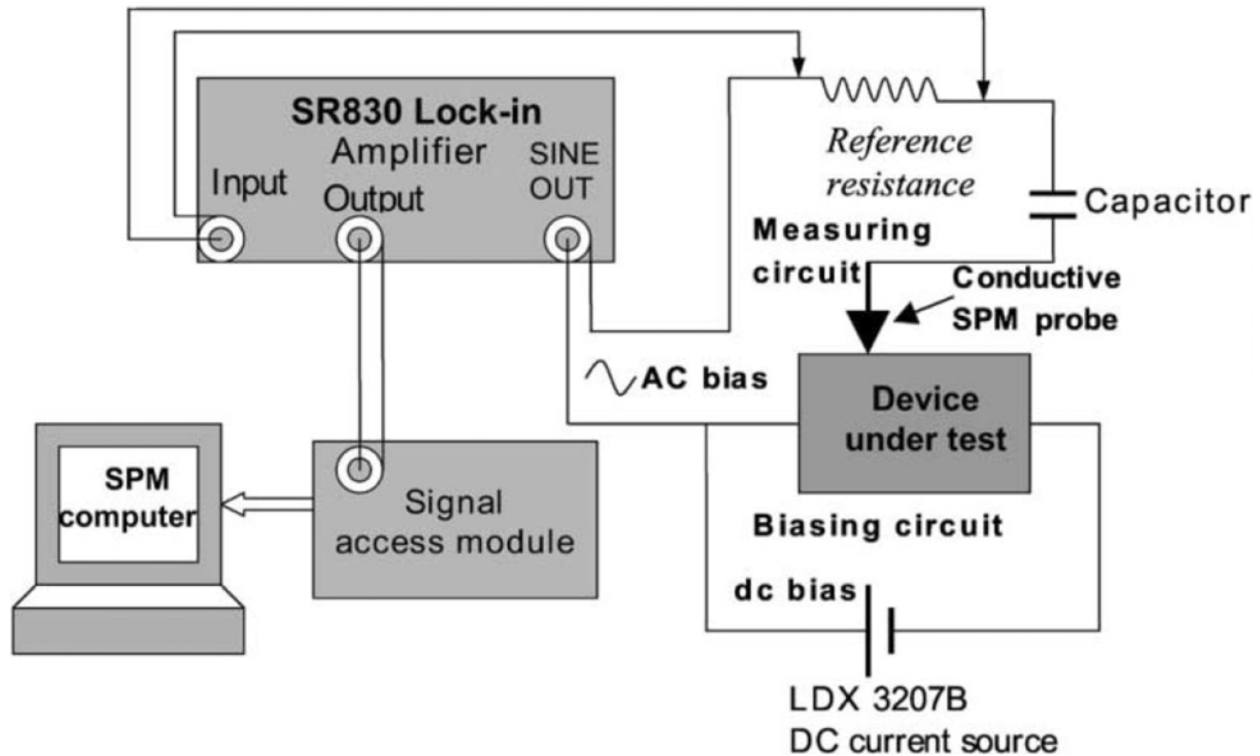

FIG. 42. Schematic circuitry of the SDSRM. The diagram shows the laser device under forward DC bias using a laser power supply, whereas an AC bias was used on the measurement circuit. A lock-in amplifier was used to measure the AC current, and the output of the lock-in amplifier was fed into the data acquisition system. (Reprinted with permission from Ref. 108, Copyright 2004, IEEE.)

active region because the former has a larger band gap.[110] Experimental measurement based on a purely input /output electrical method showed the electron overbarrier current leakage was only on the order of μA at 20°C, which was only around 0.1% of the total current injection.[109] A self-consistent analysis on MQW InGaAsP-InP lasers showed that electron current leakage could contribute significantly at high temperature, accounting for 10% of the total current injection at 80°C.[84] Disputes in previous studies call for direct observation of electron overbarrier leakage in operating laser devices and an end to speculation.

SDSRM measurements are performed under contact-mode feedback conditions. The tip is scanned over the cross-section of the device at a speed of 0.05–0.2 μm/s (scan rate of 0.005–0.02 Hz) and with force in the range of 2–5 μN. AC bias applied to the AFM tip is in the range 0.1–0.3 V peak-to-peak.

The current–voltage characteristics of the diode lasers are measured before, during, and after the SDSRM experiment: no change was observed in device electrical behavior. The topographic AFM images of the device surface, obtained simultaneously with the SDSRM data, showed no perceptible features.

Figure 43 shows a typical SDSRM image of the laser device in transverse cross- section at zero device bias.[108] The *n*-substrate is the bright band at the bottom. The buried mesa structure is clearly resolved in the SDSRM image. The narrow, bright strip on top of the mesa is the MQW active region, which is clad by *p*- and *n*-doped layers above and below. At the left and right sides of the active region are the symmetric *p*–*n*–*p*–*n* current-blocking structures. In zero device bias mode, the SDSRM image agrees very closely with conventional SSRM images[25] (always taken at zero device bias), as expected.

Figure 44a shows the cross-sectional SDSRM resistance as a function of depth below the device top surface obtained from a high-resolution SDSRM image of the MQW active region of the BH laser under zero bias. Individual quantum wells and barriers were resolved in the resistance curve, attesting to the high spatial resolution (sub 20 nm) attainable with the SDSRM technique. Resistance in the *n*-InP region is smaller than that in the *p*-InP region because the electron mobility is considerably larger than the hole mobility. The intrinsic quantum well active region appears least resistive.

Observed nonuniform resistance (R) among the six quantum wells can be ascribed to the exponentially decayed distribution of electron concentration in the intrinsic transition region from the *n*- to *p*-cladding layers. At equilibrium, the electron density distribution $n(x)$ in the intrinsic region of a p–i–n structure can

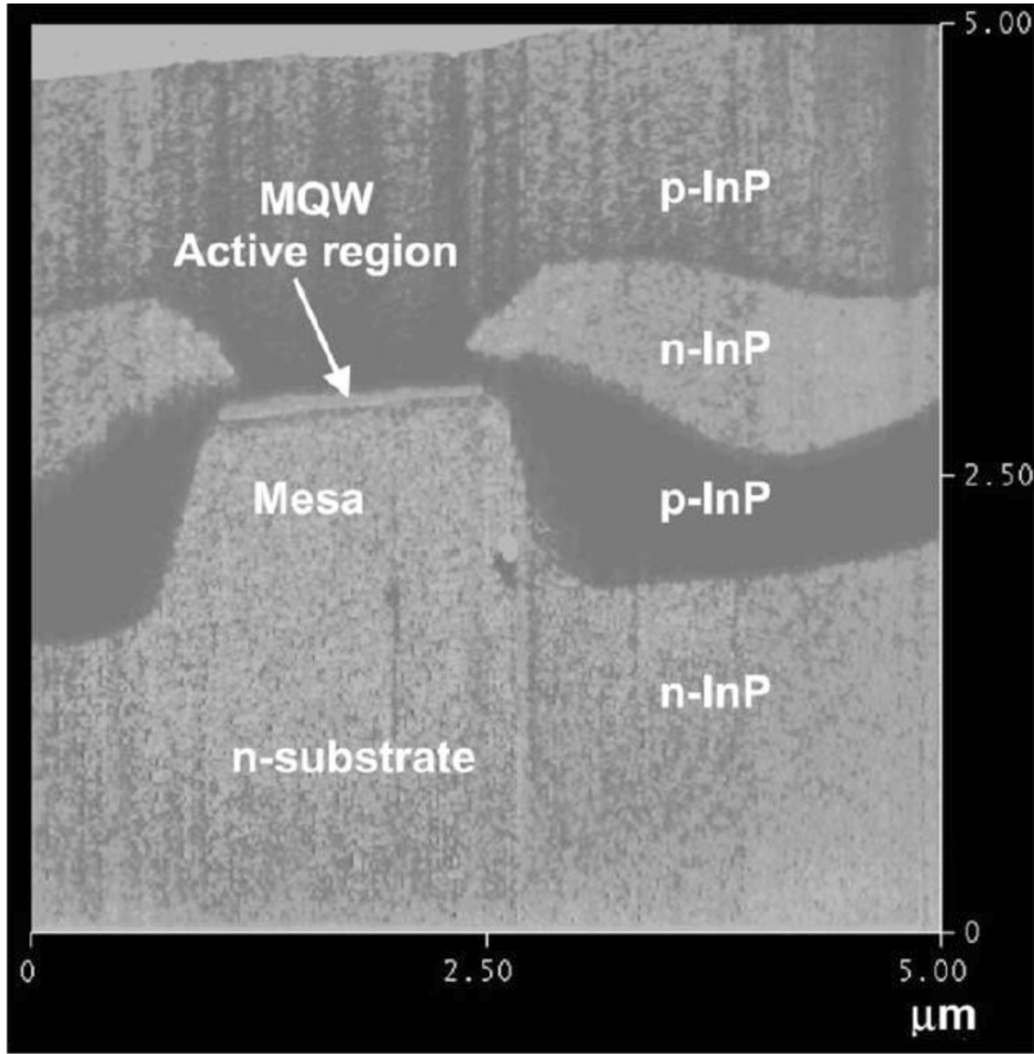

FIG. 43. Transverse cross-sectional SDSRM image of a buried heterostructure MQW laser at equilibrium under zero bias. The AC bias of the measurement circuit was 0.2 V and the scan rate was 0.05 Hz. (Reprinted with permission from Ref. 108, Copyright 2004, IEEE.)

be approximated by[111]

$$n(x) = n_0 \exp\left(\frac{q(\phi(x) - \phi_0)}{k_B T}\right), \qquad [38]$$

where $\phi(x)$ is the potential at x, k_B Boltzmann's constant, T temperature and q electron charge. n_0 and ϕ_0 are the electron density and potential at a reference point, respectively. Given that the electric field (E) inside the intrinsic active region remains constant, the potential is a linear function of $x : \phi(x) = E(x - x_0) + \phi_0$. Because the hole mobility is much smaller than electron mobility, the measured SDSRM conductance σ (=1/ R_d) in the active region is essentially due to electron conductance. Thus, the contribution from hole conductance is ignored, yielding

$$\frac{1}{R(x)} = \sigma(x) = \sigma_0 + a n_0 \exp\left(\frac{qE(x - x_0)}{k_B T}\right), \qquad [39]$$

where σ_0 is the term counting other contributions for the measured conductance, that is, surface leakage, and a is a coefficient constant.

The fitting of the measured resistance at each quantum-well using Eq. 39 is shown in Figure 44b. The good agreement between experimental data and theoretical prediction verifies the assumption: the measured SDSRM resistance essentially relates to local electron density.

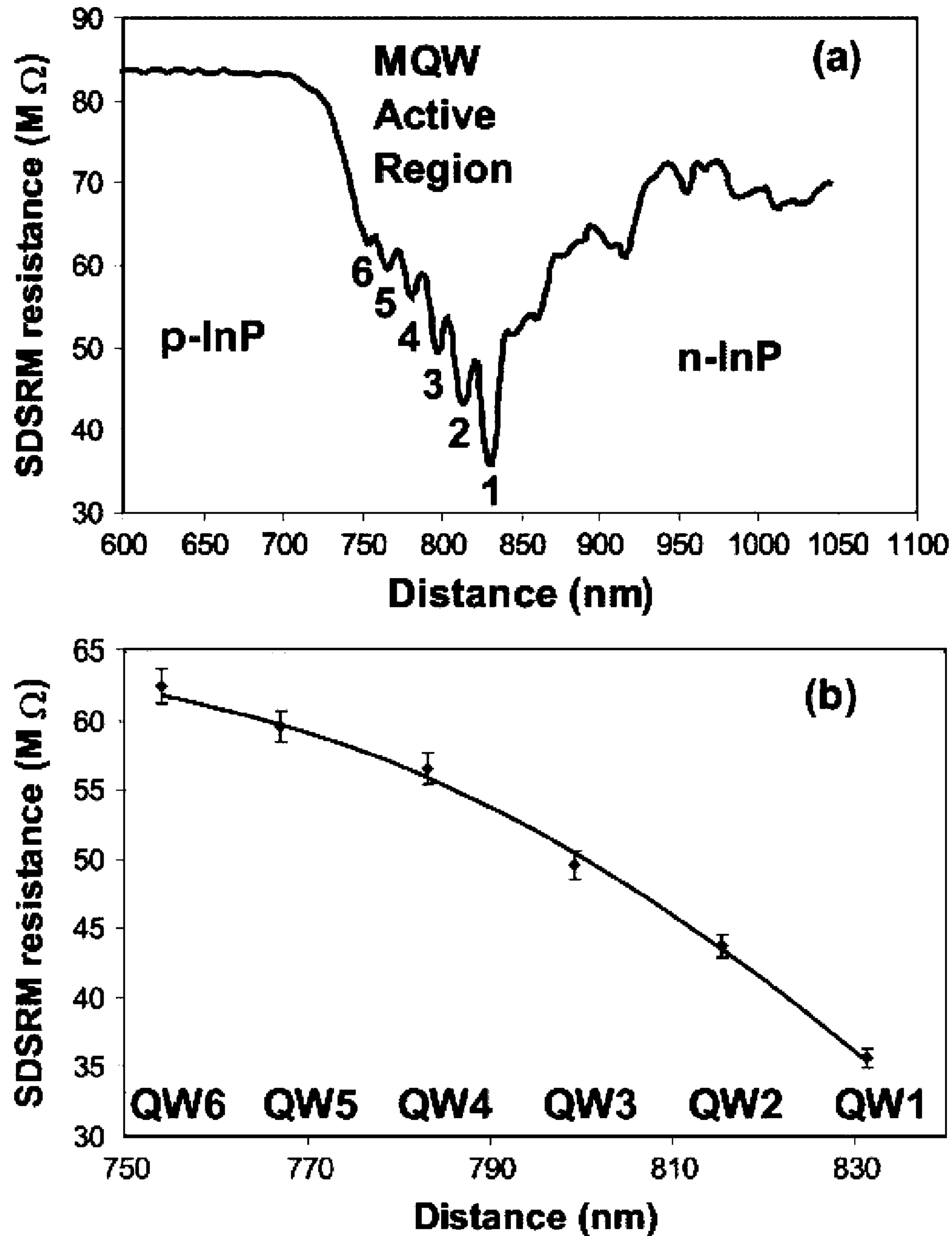

FIG. 44. (a) Cross-sectional analysis of the SDSRM resistance across the active region of the BH laser at equilibrium. Individual QWs are delineated. The SDSRM scan size was 1.65 μm, the tip bias was 0.3 V peak-to-peak, and the scan rate was 0.05 Hz. The number of sampling points along each line scan was 512. (b) The fitting of measured resistance at individual QWs as a function of distance. Discrete diamonds: experimental data; solid line: fitting curve. (Reprinted with permission from Ref. 108, Copyright 2004, IEEE.)

Of greatest interest in SDSRM is probing the internal dynamics of a BH laser in its intended operational state. SDSRM is sensitive to electron density—this is to achieve the direct observation of the electron density distribution in an operating device.

The turn-on voltage of the laser diode for a nontrivial current is around 0.7 V. Current threshold for lasing is around 8 mA at room temperature. The overall series differential resistance of the laser above threshold derived from the current–voltage curve is 6 Ω, confirming

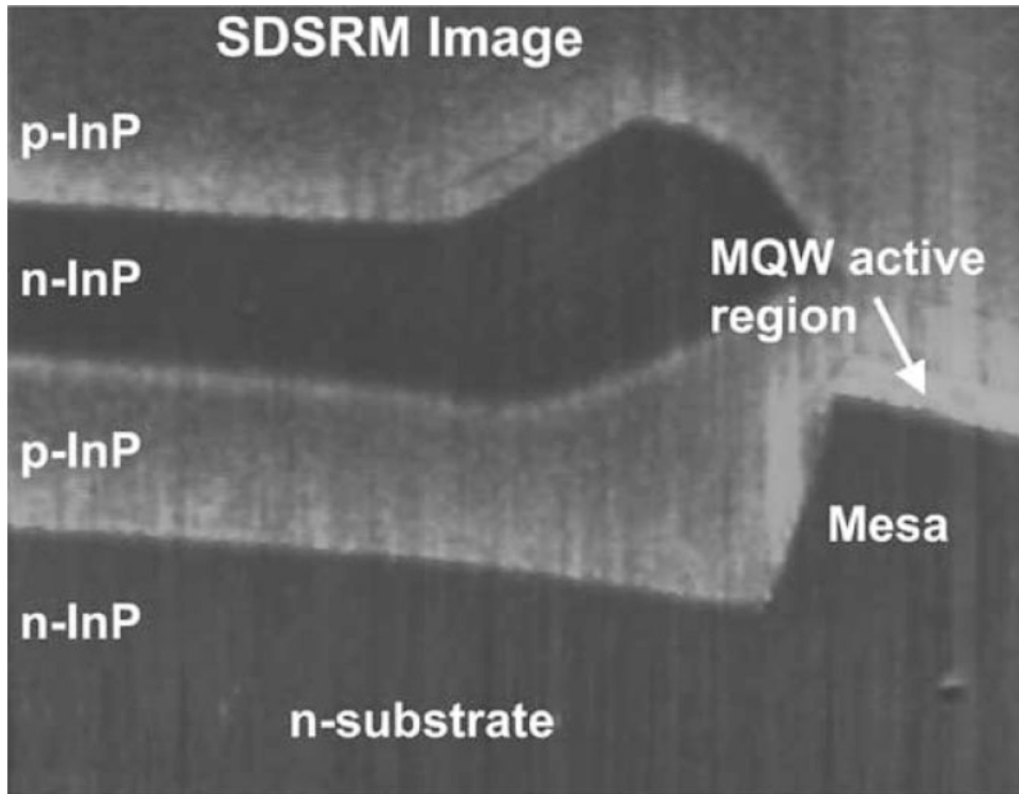

FIG. 45. Transverse cross-sectional SDSRM image of the BH MQW laser under forward current injection of 20 mA. The AC bias of the measurement circuit was 0.3 V and the scan rate was 0.05 Hz. (Reprinted with permission from Ref. 108, Copyright 2004, IEEE.)

the presumption that SDSRM is non-perturbative to device operation.

Figure 45 shows an SDSRM image of the transverse cross-section of a BH MQW laser under a forward bias of 0.955 V corresponding to a current of 20 mA. Part of the MQW active region, buried mesa and *p–n–p–n* current blocking structure are clearly delineated in the image.

Compared to the image at zero bias (Figure 43), the MQW active region under forward bias appears wider in vertical direction and brighter in contrast. Because the brightness is a direct sign of local free carrier concentration—higher carrier concentration regions appears brighter—SDSRM visualizes free carrier accumulation in the MQW active region. For the same reason, brighter strips in *p*-InP layers adjacent to the *n*-InP are observed in the *p–n–p–n* thyristor structures.

Figure 46 shows the cross-sectional resistance through the active region of the BH laser under zero and forward bias voltages obtained from a single SDSRM scan. Impact of the application of external bias is twofold: (1) the valley in the biased curve is wider, deeper, and more symmetric than that of the unbiased curve; and (2) the biased curve shows a shoulder structure over the adjoined *p*-cladding layer near the active region. As the forward bias is increased beyond the threshold voltage, the higher carrier concentration within the active region yields a lower differential spreading resistance as sensed by the AFM tip and the deeper valley as observed in the SDSRM curve.

The shoulder structure in the *p*-cladding layer reveals excess electrons leaking out of the active region. Electrons with high kinetic energy in quantum wells may surmount the energetic barrier at the *p*-side junction of the separate-confinement-heterostructure and diffuse into the *p*-doped region; this effect is responsible for the lower resistance shoulder structure as seen in the SDSRM curve. Width of the shoulder is on the same order of the diffusion length of electrons in *p*-InP. The measured width, as read directly from the curve, is around 500 nm. This agrees with the reported minority carriers effective diffusion lengths of 380–540 nm.[112] Because hole overbarrier leakage is generally much weaker and SDSRM is much less sensitive to holes, no shoulder structure is observed on the *n*-doped side. In the *n*- and *p*-InP regions further away from the MQW active region, the measured resistance remains unaffected by the application of a device bias. This again confirms that the SDSRM measurement is insensitive to device bias and sensitive particularly to electron density.

It has been theoretically predicted by Aarts[101] and Kazarinov[113] that the increase in the voltage drop at the *p*-InP-to-SCH (separate-confinement-heterostructure) interface results in reduction of the thermionic emission barrier for electrons

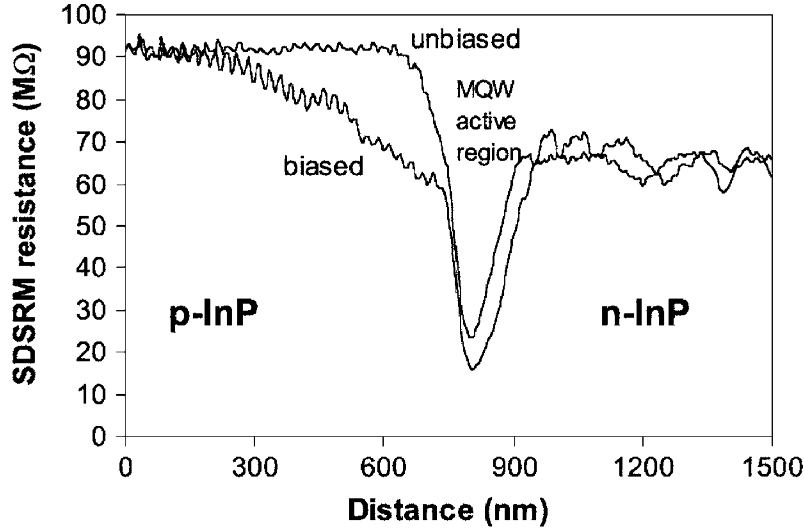

FIG. 46. Cross-sectional analysis of the SDSRM resistance across the active region of the MQW active region of the BH laser under zero and under forward (0.851 V) biases. The SDSRM scan size was 5.0 μm and the scan frequency was 0.05 Hz. The number of sampling points along each line scan was 512. The shoulder structure of the biased SDSRM curve is attributed to electron overbarrier leakage. (Reprinted with permission from Ref. 108, Copyright 2004, IEEE.)

and, consequently, in an increase in electron overbarrier leakage. SVM results in Figure 47 provide direct experimental verification: a significant voltage drop (around 0.2 V) is observed from the MQW active region to the *p*-injector layer above threshold. SVM thus offers insight into the results of SDSRM: electrons leak over heterobarriers on the *p*-side in MQW lasers operating at room temperature due to heterobarrier lowering.

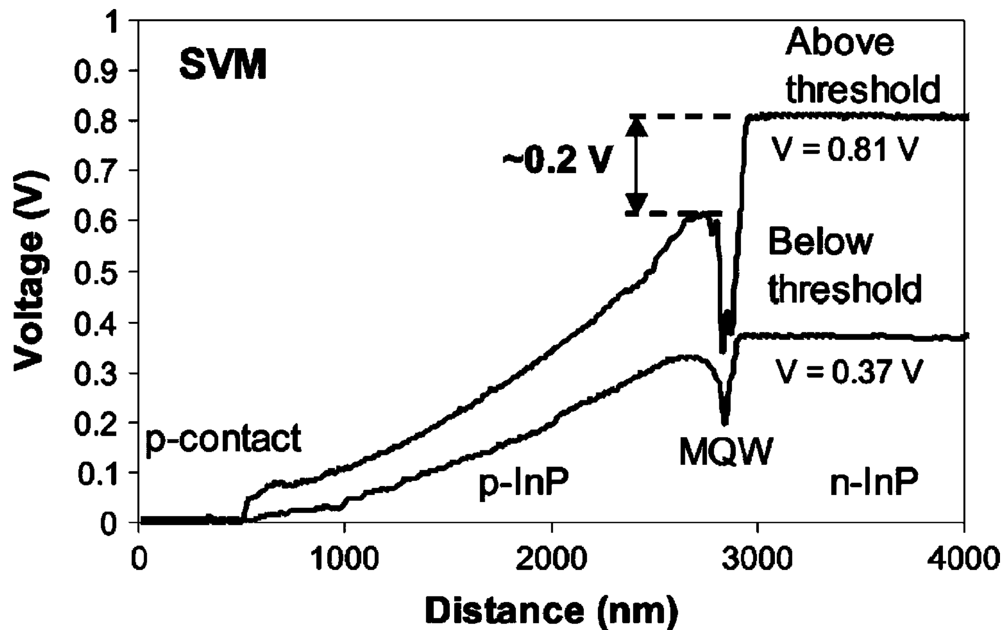

FIG. 47. One-dimensional voltage profiles across the active region of the BH laser measured using SVM. The laser was biased at forward bias voltages of 0.37 V (below threshold) and 0.81 V (above threshold). The voltage drop (~0.2 V) measured in the above-threshold curve across the active region leads to a reduction of the heterostructure energetic barrier for thermionic emission of electrons from the active region, yielding electron overbarrier leakage observed in Figure 46. (Reprinted with permission from Ref. 108, Copyright 2004, IEEE.)

NANOSCALE ELECTRONIC DEVICES: EXPERIMENTAL CHALLENGES

Nanocrystals and Composites

A new class of optoelectronic devices is emerging, a class that has wide spectral tunability, seamless integration with electronic and photonic circuits, and economic, scalable fabrication. Low-cost, easy-to-make optoelectronic devices will provide high-bandwidth data connections directly to users (e.g., fiber-to-the-desktop) for high-definition multimedia on demand. Devices will be small enough (nanometers) and cheap enough (cents) to be used on circuit boards to eliminate data bottlenecks chip-to-chip and within chips to facilitate distribution of critical signals.

Today's optoelectronic components are grown by MBE and MOCVD, complex processes that require the cleanest and safest of conditions in highly specialized equipment. Current device structures limit spectral tunability; current materials limit electronic integration. The high performance of these devices comes at premium cost.

Conversely, nanocrystals are easy to make in a regular chemistry lab, are widely tunable and highly integrable. The size of nanocrystal semiconductors gives rise to striking new properties. Luminescence and absorption are tuned over wide visible[114] and infrared[38] spectral ranges by nanocrystal size. Nanocrystals self-assemble in organometallic chemical reactions that take place in a flask of an ordinary fumehood[115] and their size is tuned by controlling the growth reaction. Electronic and mechanical properties are engineered by encapsulating the nanocrystal with semiconductor or organic ligands[116] (Figure 48a). Encapsulation is also tuned by basic chemistry during or after growth. Nanocrystals are conveniently mixed into semiconducting polymers and the polymers are spun into layers to form devices (Figure 48b). Optoelectronic luminescent (Figure 48c) and photodetection (Figure 48d) devices can be made to span the entire telecommunications spectral range and beyond with a single material system.

Optoelectronic interaction between a host polymer and an active nanocrystal occurs via three processes: incoherent energy transfer (Förster transfer),[117] coherent energy transfer,[118] and charge transfer.[35] Although it is clear that coherent transfer dominates in nonlinear optical interactions,[118] the nanocomposite research community remains agnostic as to whether Förster or charge transfer dominates in optoelectronic conversion (in either conversion direction).[119]

Scanning probe techniques could be used to resolve which energy transfer mechanism is dominant and identify specifics of the transfer rate, pathway (whether mediated by intermediate nanocrystals), and so on. AFM has been used to characterize sizes of individual nanocrystals and ensembles,[120] so spatial resolution is sufficient and addressing individual nanocrystals is possible. EFM was used to observe the charging and discharging of individual nanocrystals,[28,35] and to probe nanocomposite films.[43]

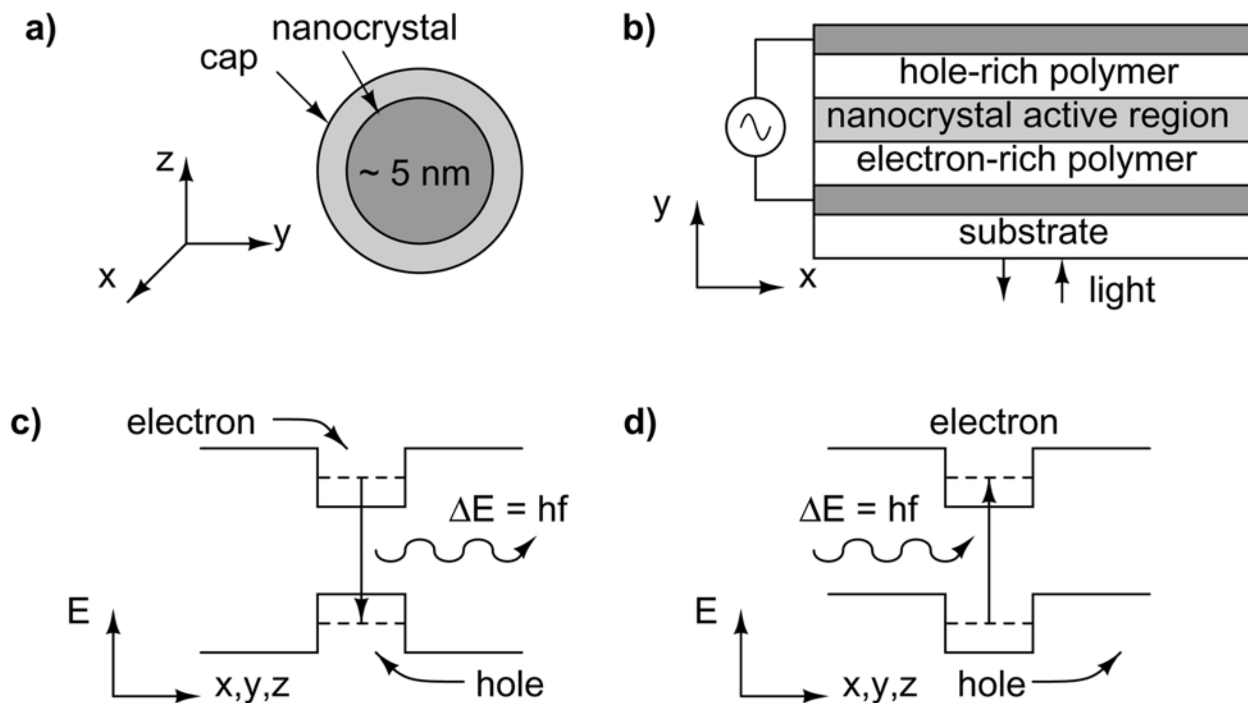

FIG. 48. Nanocrystal optoelectronic devices, (a) Spherical semiconductor colloidal nanocrystal, typical average size ~5 nm (typical range 2–20 nm). (b) Typical nanocrystal–polymer composite device structure: metal electrodes address polymer functional layers with the central layer containing active semiconductor nanocrystals. (c) Energy transfer from polymer to nanocrystal for photogeneration. (d) Energy transfer from nanocrystal to polymer for photodetection.

Charge transport and separation is a process of central importance in the area of nanotechnology, particularly in composites of organic polymers and inorganic nanocrystals.[121] Polymer/nanocrystal blends are attracting attention for their potential applications in a wide range of electronic and optoelectronics devices such as light-emitting diodes[37,122] and photovoltaic devices[123] and nonlinear optical devices.[124,125] Electron transfer from polymers to nanocrystals is typically studied using photoluminescence quenching and photoconductivity. Detailed information about the transfer process, such as the spatial separation of holes and electrons and the underlying mechanisms for the transfer, is urgently needed. SVM and SDSRM could be employed to directly probe these transports processes in working devices.

Unlike EFM, which is a non-contact technique, SVM and SDSRM require good electrical contact with the sample and therefore require a relatively smooth scan surface. The geometry of spin-coated nanocomposite devices is unsuitable at present for SVM/SDSRM as the edges are uneven and uncleavable. Furthermore, nanocrystals are randomly distributed in the active layer and may not reach the scanning surface in a predictable manner; one must address how an edge-lying nanocrystal should differ in behavior from a nanocrystal buried deep in the device. For these reasons, SVM has not been performed on these devices to date to the authors' knowledge. However, if these geometrical issues could be solved—perhaps by dye-casting devices in a cubic mold and ensuring smooth facets—potential distributions that are thought to govern charge capture[34] could be observed and confirmed. Proposed theoretical potential distributions[34] dictate current design rules and so direct observation is extremely valuable.

Nanowires and Interconnects

Quasi-one-dimensional objects exhibit quantum confinement in two spatial dimensions. Such objects could be made into nanoscopic electronic wires with the possibility of ballistic transport, quantum resistance, and Coulomb blockade effects.[126] Two strong candidates for nanowires are carbon nanotubes (graphine sheets rolled into hollow tubes) and molecular DNA.

For instance, the way in which a carbon nanotube is rolled, its *chirality*, has direct influence on its current-voltage response: nanotubes can be metallic, semiconducting, or insulating.[127] By depositing nanotubes onto an insulating SiO_2 substrate with gold contacts, a metallic EFM probe was used in full contact mode to measure the I–V characteristics of individual nanotubes,[126] essentially employed as SSRM. As shown in Figure 49, certain carbon nanotubes exhibit semi-metallic (top) or semiconducting (bottom) characteristics. The authors noted that a measured resistance of 10 kΩ for the semi-metallic tubes was among the lowest recorded values at the time, which is promising for conduction applications. In contrast, DNA was found to be insulating when deposited similarly onto mica with gold contacts.[126] Figure 50 shows topology (top) and potential (bottom) captured in KPFM mode (the gold electrode is in the bottom left corner of the images); it is clear that the potential of the DNA is invisible from that of the mica, thus this particular DNA is highly resistive and unsuitable for charge conduction.

The other scanning probe techniques—SVM, SDSRM, and SCM—will also become invaluable tools for characterizing nanowires that link nanoscopic devices.

SUMMARY AND COMPARISON

Features of the methods described earlier are summarized in Table 1. These include spatial resolution (in nanometers), dynamic range (in atoms/cm^3), functionality, quantification ability, nondestructiveness, and applicability to operating devices. Together, these techniques allow direct observation of key internal operating parameters in two dimensions. It is possible to delineate quantitatively the transverse cross-sectional electronic structure of operating complex two-dimensional devices such as diode lasers. Also compared are non-AFM SIMS and EBIC techniques that do not apply to devices under operating conditions.

SSRM and SCM techniques represent the leading candidates for quantitative profiling of 2-D carrier distributions with nanometer resolution in semiconductor devices. They have sub-20 nm spatial resolution and wide dynamic range (10^{15}–10^{20} cm^{-3}) and can be applied to arbitrary structures. Critical examples were presented: the application of SSRM and SCM to BH MQW lasers. A systematic and quantitative study of the laser devices was demonstrated.

EFM permits the simultaneous capture of sample topology and electric potential[128] or charge.[43] Scanning is generally performed in the noncontact regime and is therefore nondestructive, making it ideal for electronic characterization of fragile materials such as DNA.[126] With EFM one can measure important properties of systems such as the diffusivity and resistance of highly resistive films that could not be measured easily by any other technique.[43] An experimental disadvantage is that the potential measured is susceptible to the sample surface states and trapped charges[30]—what one measures may not be the true sample potential and may depend on work function difference and surface contamination (due to adsorption of water and organics in the ambient atmosphere). Interpretation of basic EFM data requires simulation and calibration. However, uncalibrated potential *differences* still provide useful information. If surface charge is too strong, it becomes difficult to obtain topographic profiles needed to maintain constant height on the second pass of two-pass operation.[43]

KFM, although requiring an additional feedback loop to the tip, measures the absolute potential difference[129] between two points, making interpretation easy and accurate. It can also be used to measure built-in potentials (such as in a p–n junction at equilibrium)[30] that could not be measured by any another scanning probe technique.

SVM is a diagnostic tool, capable of identifying sources of sub-optimal performance.[72,82] SVM is a failure analysis tool, able to pinpoint causes of device failure.[75] SVM is a

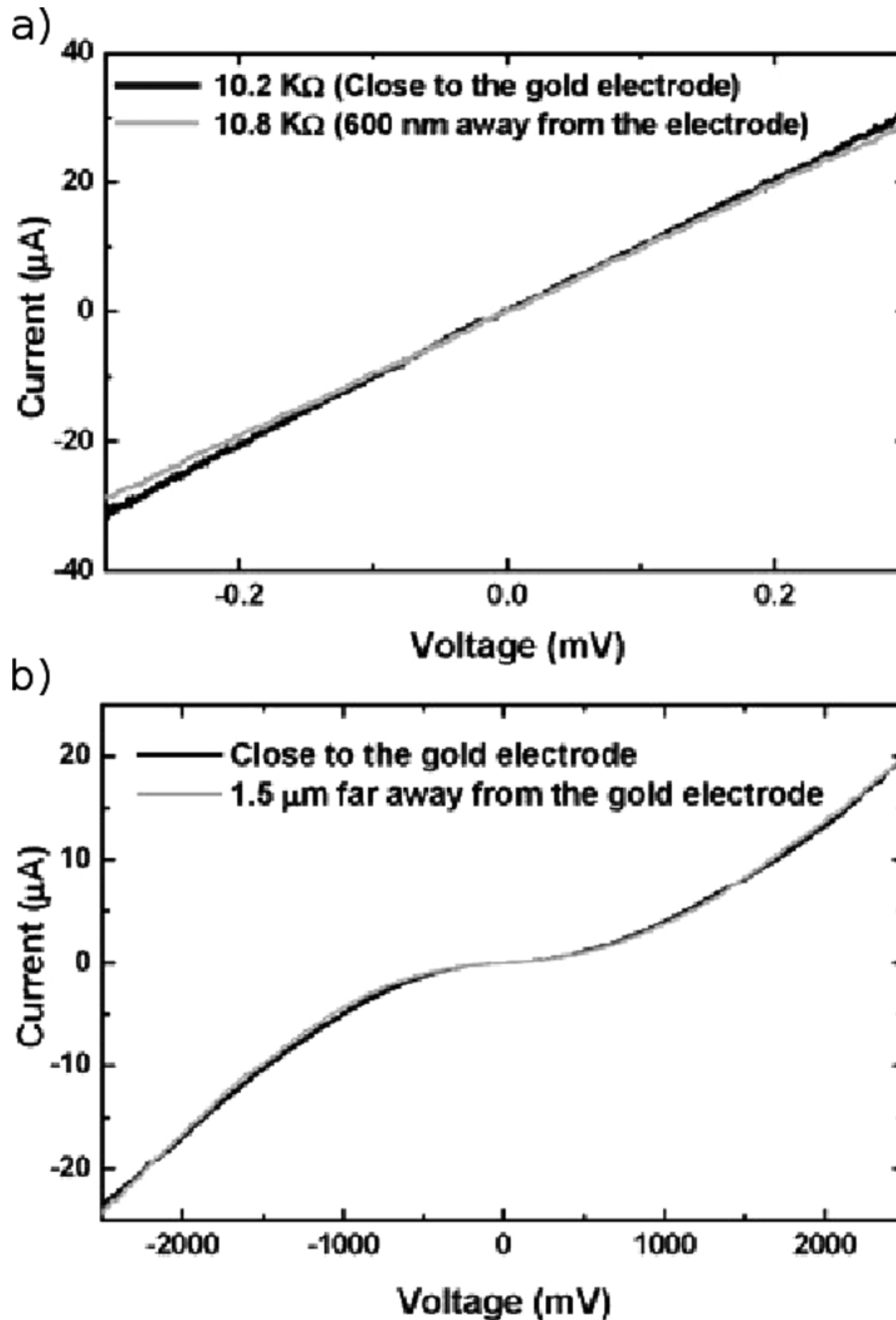

FIG. 49. I–V characteristics of individual semi-metallic (top) and semi-conducting (bottom) carbon nanotubes obtained by contact EFM. (Reprinted with permission from Ref. 126, Copyright 2002, Institute of Physics Publishing Limited.)

reverse engineering tool, illuminating device structure and *active* behavior.[14,24] SVM is a development tool, used in conjunction with other analysis techniques such as SDSRM. The physical basis of SVM technique was established and presented. The first SVM measurements were performed on biased InP *p*–*n* junctions and compared with prediction from theory. Voltage profiles across the InP *p*–*n* junction structure under forward and reverse biases were measured. Variation of the depletion width with the application of external bias was observed with nanometer resolution and agreed well with the expectation from a model of an idealized *p*–*n* junction.

Two-dimensional carrier transport in the RWG lasers was investigated directly and quantitatively using SVM. By examining the lateral variation of local voltage within the *n*-cladding layers of the laser, it was found that the local current density at the edge was 40% smaller than that at the center of the 2.4 μm-wide

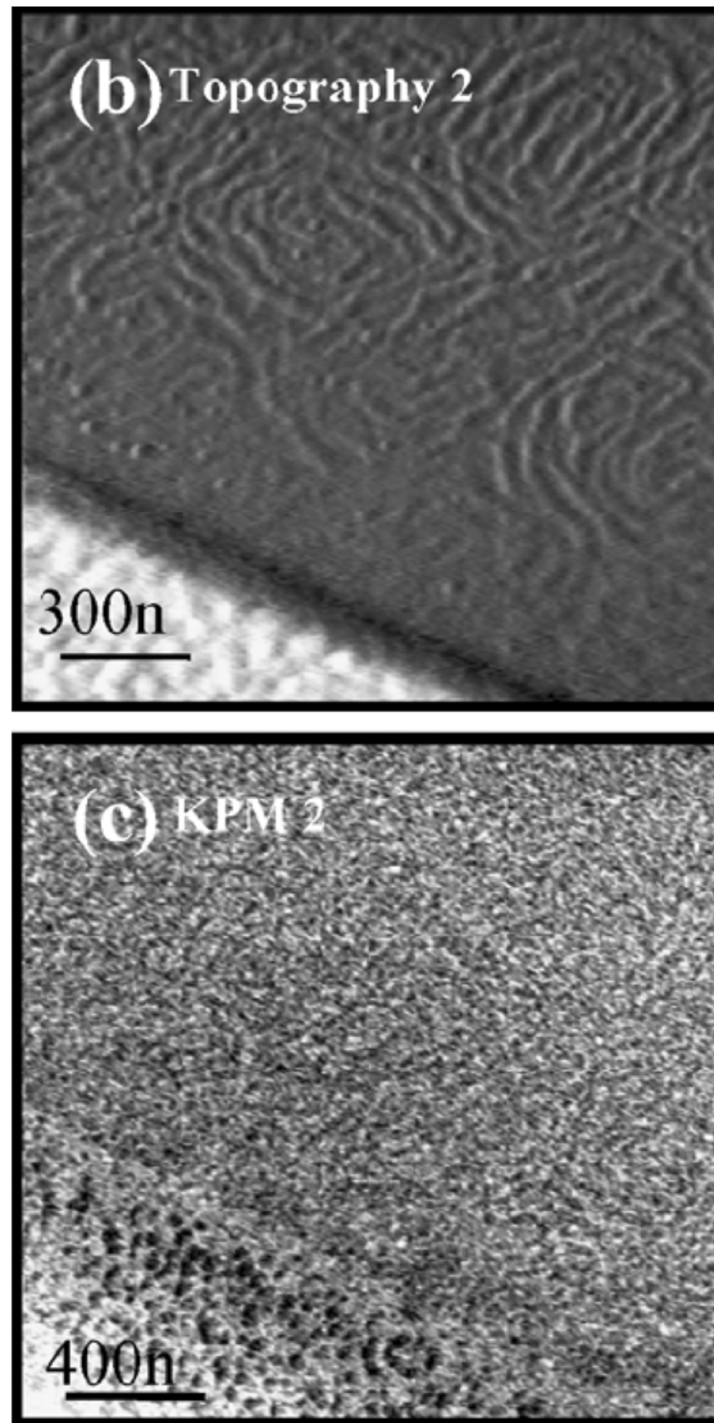

FIG. 50. Topographic EFM (top) and potential KPFM (bottom) images of DNA on mica next to a gold contact; the DNA is at the same potential as the mica and is therefore insulating. (Reprinted with permission from Ref. 126, Copyright 2002, Institute of Physics Publishing Limited.)

TABLE 1
Comparison of electronic SPM techniques and EBIC and SIMS

Method	Resolution [nm]	Dynamic range [cm^{-3}]	Functionality	Quantifiable	Nondestructive	Application to operating device	Comments and problems
AFM	5	n/a	Topographic information only	n/a	Yes	Yes	No electronic property characteristics
SSRM	20	10^{15}–10^{20}	Free-carrier profiling	Yes	Yes	No	Sharp delineation difficult
SCM	20	10^{15}–10^{20}	Free-carrier profiling	Limited	Yes	Limited	Poor calibration procedure
EFM	100	10^{15}–10^{20}	Surface potential mapping	Limited	Yes	Yes	Poor calibration procedure
SVM	5	n/a	Device potential mapping	Yes	Yes	Yes	Excellent quantification, resolution
SDSRM	5	10^{15}–10^{20}	Free-carrier profiling	Yes	Yes	Yes	Good quantification, excellent resolution
SIMS	50	10^{16}–10^{20}	Dopant concentration profiling	Yes	No	No	Special device structure required
EBIC	100	n/a	Failure analysis	No	Yes	Limited	Qualitative only

ridge under 150 mA of forward current injection. SVM provided a direct means for monitoring this key phenomenon. Two-dimensional SVM was used to delineate quantitatively the transverse cross-sectional structures of complex two-dimensional devices—functional BH MQW lasers—under working conditions was realized. SVM results showed that the turn on of the diode leakage path instigates the observed current-blocking breakdown as the device is biased at high current injection.

SVM was applied to the investigations of structure/performance relations in two RWG MQW lasers that exhibited different input/output behavior. The SVM measurements revealed quantitatively the internal voltage distribution of the transverse cross-section of actively driven devices. It allowed localization of the problem and focusing of the search for further explanatory evidence. SVM was also applied to study the p-type contact strategy of a state-of-the-art uncooled ridge waveguide laser. Although the metal/p-InGaAs contact was found to be ohmic and essentially lossless, the p-InGaAs/p-InP heterojunction was observed to dissipate a surprising one third of the total power applied to the laser over the operating bias range, causing self-heating and performance degradation.

Scanning differential spreading resistance microscopy was successfully developed and applied to profile the electron concentration in BH MQW lasers under zero and forward biases. High-resolution SDSRM imaging over the MQW active region of a BH laser yielded a sub-20 nm spatial resolution in the measured resistance. SDSRM results provided direct experimental observation of the accumulation of free carriers within the MQW active region and the diffusion of minority carriers into p-cladding layer. The results demonstrated the utility of SDSRM to delineate the transverse cross-section of free carrier density in two-dimensional devices such as MQW BH lasers under operating conditions. The method permitted the first direct experimental observation of electron overbarrier leakage in BH MQW lasers operating at room temperature. SVM provided an explanation for this observation via a direct observation revealing of heterobarrier lowering.

ACKNOWLEDGMENTS

The authors are indebted to Iain Calder, Grant Este, Rick Streater, Anthony J. SpringThorpe, Greg Letal, Alex Shik, and Shiguo Zhang.

REFERENCES

1. G. Binnig, C. F. Quate, and C. Geber, Atomic force microscope, *Phys. Rev. Lett.* **56**(9), 930–933 (March 1986).
2. Y. Martin, C. C. Williams, and H. K. Wickramasinghe, Atomic force microscope—force mapping and profiling on a sub 100-A scale, *J. Appl. Phys.* **61**(10), 4723–4729 (May 1987).
3. T. Trenkler and W. Vandervorst, Two-dimensional profiling in silicon using conventional and electrochemical selective etching, *J. Vac. Sci. Technol. B* **16**(1), 349–354 (Jan./Feb. 1998).
4. E. P. Visser, J. W. Gerritsen, W. J. P. van Enckevort, and H. van Kem-pen, Tip for scanning tunneling microscopy made of monocrystalline semi-conducting, chemical vapor deposited diamond, *Appl. Phys. Lett.* **60**(26), 3232–3234 (June 1992).
5. C. E. Nebel, J. Münz, M. Stutzmann, R. Zachai, and H. Güttler, Electronic properties of CVD and synthetic diamond, *Phys. Rev. B* **55**(15), 9786–9791 (April 1997).
6. M. J. Rutter and J. Robertson, *Ab Initio* calculation of electron affinities of diamond surfaces, *Phys. Rev. B* **57**(15), 9241–9245 (April 1998).
7. L. Diederich, O. M. Küttel, P. Aebi, and L. Schlapbach, Electron affinity and work function of differently oriented and doped

diamond surfaces determined by photoelectron spectroscopy, *Surf. Sci.* **418**(1), 219–239 (1998).

8. A. G. Fitzgerald, Y. Fan, P. John, C. E. Troupe, and J. I. R. Wilson, Characterization of the surface morphology and electronic properties of microwave enhanced chemical vapor deposited diamond films, *J. Vac. Sci. Technol. B* **18**(6), 2714–2721 (Nov./Dec. 2000).
9. D. Steinbach, A. Flöter, H. Güttler, R. Zachai, and P. Ziemann, Microscopic measurements of the electrical properties of highly oriented B-doped films: Influence of grain boundaries, *Diamond Relat. Mater.* **8**, 273–277 (1999).
10. C. Saby and P. Muret, Photoelectron spectroscopy of boron-doped homoepitaxial diamond (100) surfaces with several terminations and related Schottky barriers, *Diamond Relat. Mater.* **11**, 851–855 (2002).
11. T. Trenkler, T. Hantschel, R. Stephenson, P. De Wolf, W. Vandervorst, L. Hellemans, A. Malavé, D. Büchel, E. Oesterschulze, W. Kulisch, P. Niedermann, T. Sulzbach, and O. Ohlsson, Evaluating probes for 'electrical' atomic force microscopy, *J. Vac. Sci. Technol. B* **18**(1), 418–427 (Jan./Feb. 2000).
12. O. Wolter, T. Bayer, and J. Greschner, Micromachined silicon sensors for scanning force microscopy, *J. Vac. Sci. Technol. B* **9**(2), 1353–1357 (1991).
13. T. Trenkler, P. De Wolf, and W. Vandervorst, Nanopotentiometry: Local potential measurements in complementary metal-oxide-semiconductor transistors using atomic force microscopy, *J. Vac. Sci. Technol. B* **16**(1), 367–372 (Jan./Feb. 1998).
14. T. Trenkler, R. Stephenson, P. Jansen, and W. Vandervorst, New aspects of nanopotentiometry for complementary metal-oxide-semiconductor transistors, *J. Vac. Sci. Technol. B* **18**(1), 586–594 (Jan./Feb. 2000).
15. T. Hantschel, P. Niedermann, T. Trenkler, and W. Vandervorst, Highly conductive diamond probes for scanning spreading resistance microscopy, *Appl. Phys. Lett.* **76**(12), 1603–1605 (March 2000).
16. J. E. Sader and R. C. Sader, Susceptibility of atomic force microscope cantilevers to lateral forces: Experimental verification, *Appl. Phys. Lett.* **83**(15), 3195–3197 (Oct. 2003).
17. S. Dixon-Warren, R. P. Lu, S. Ingrey, D. Macquistan, T. Bryskiewicz, G. Smith, and B. Bryskiewicz, Scanning spreading resistance microscopy study of an MOCVD grown InP optoelectronic structure, *J. Vac. Sci. Technol. B* **19**, 1752 (2001).
18. R. P. Lu, K. L. Kavanagh, S. Dixon-Warren, A. Kuhl, A. J. SpringThorpe, E. Griswold, G. Hillier, I. Calder, R. Arès, and R. Streater, Calibrated scanning spreading resistance microscopy profiling of carriers in III-V structures, *J. Vac. Sci. Technol. B* **19**(4), 1662–1670 (July/Aug. 2001).
19. P. De Wolf, M. Geva, T. Hantschel, W. Vandervorst, and R. B. Bylsma, Two-dimensional carrier profiling of InP structures using scanning spreading resistance microscopy, *Appl. Phys. Lett.* **73**(15), 2155–2157 (Oct. 1998).
20. P. De Wolf, M. Geva, C. L. Reynolds, T. Hantschel, W. Vandervorst, and R. B. Bylsma, Two-dimensional carrier profiling of InP-based structures using scanning spreading resistance microscopy, *J. Vac. Sci. Technol. A* **17**(4), 1285–1288 (July/Aug. 1999).
21. P. De Wolf, W. Vandervorst, H. Smith, and N. Khalil, Comparison of two-dimensional carrier profiles in metal—oxide—semiconductor field-effect transistor structures obtained with scanning spreading resistance microscopy and inverse modeling, *J. Vac. Sci. Technol. B* **18**(1), 540–544 (Jan./Feb. 2000).
22. M. W. Xu, T. Hantschel, and W. Vandervorst, Three-dimensional carrier profiling of InP-based devices using scaniing spreading resistance microscopy, *Appl. Phys. Lett* **81**(1), 177–179 (July 2002).
23. R. P. Lu, K. L. Kavanagh, S. Dixon-Warren, A. J. SpringThorpe, R. Streater, and I. Calder, Scanning spreading resistance microscopy current transport studies on doped III–V semiconductors, *J. Vac. Sci. Technol. B* **20**(4), 1682–1689 (July/Aug. 2002).
24. D. Ban, E. H. Sargent, St. J. Dixon-Warren, I. Calder, T. Grevatt, G. Knight, and J. K. White, Two-dimensional transverse cross-section nanopotentiometry of actively-driven buried heterostructure multiple-quantum-well lasers, *J. Vac. Sci. Technol. B* **20**(6), 2401–2407 (Nov./Dec. 2002).
25. D. Ban, E. H. Sargent, St. J. Dixon-Warren, T. Grevatt, G. Knight, G. Pakulski, A. J. Spring-Thorpe, R. Streater, and J. K. White, Two-dimensional profiling of carriers in a buried heterostructure multi-quantum-well laser: Calibrated scanning spreading resistance microscopy and scanning capacitance microscopy, *J. Vac. Sci. Technol. B* **20**(5), 2126–2132 (Sept./Oct. 2002).
26. Y. Martin, D. W. Abraham, and H. K. Wickramasinghe, High-resolution capacitance measurement and potentiometry by force microscopy, *Appl. Phys. Lett.* **52**(13), 1103–1105 (March 1988).
27. B. D. Terris, J. E. Stern, D. Rugar, and H. J. Mamin, Contact electrification using force microscopy, *Phys. Rev. Lett.* **63**(24), 2669–2672 (Dec. 1989).
28. T. D. Krauss and L. E. Brus, Charge, polarizability, and photoionization of single semiconductor nanocrystals, *Phys. Rev. Lett.* **83**(23), 4840–4843 (Dec. 1999).
29. P. Girard, Electrostatic force microscopy: Principles and some applications to semiconductors, *Nanotechnolgy* **12**, 485–490 (2001).
30. F. Robin, H. Jacobs, O. Homan, A. Stemmer, and W. Bächtold, Investigation of the cleaved surface of a *p–i–n* laser using kelvin probe force microscopy and two-dimensional physical simulations, *Appl. Phys. Lett.* **76**(20), 2907–2911 (2000).
31. G. Lévêque, P. Girard, E. Skouri, and D. Yarekha, Measurement of electric potential in a laser diode by kelvin probe force microscopy, *Appl. Surf. Sci.* **157**, 251–255 (2000).
32. M. Azize, P. Girard, R. Teissier, A. N. Baranov, and A. Joullié, Failure analysis of a cascade laser structure by electrostatic force microscopy, *J. Vac. Sci. Technol. B* **21**(5), 2151–2154 (Sept./Oct. 2003).
33. F. Capasso, R. Paiella, R. Martini, R. Colombelli, C. Gmachl, T. L. Myers, M. S. Taubman, R. M. Williams, C. G. Bethea, K. Unterrainer, H. Y. Hwang, D. L. Sivco, A. Y. Cho, A. M. Sergent, H. C. Liu, and E. A. Whittaker, Quantum cascade lasers: Ultrahigh-speed operation, optical wireless communication, narrow linewidth, and far-infrared emission, *IEEE J. Quantum Electron.* **38**(6), 511–532 (June 2002).
34. A. Shik, S. Yu, E. Johnson, H. Ruda, and E. H. Sargent, Carrier transport and luminescence in composite organic-inorganic light-emitting devices, *Solid State Electron.* **46**(1), 61–68 (Jan. 2002).
35. T. D. Krauss, S. O'Brien, and L. E. Brus, Charge and photoionization properties of single semiconductor nanocrystals, *J. Phys. Chem. B* **105** 1725–1733 (2001).
36. M. A. Petruska, A. V. Malko, P. M. Voyles, and V. I. Klimov, High-performance, quantum dot nanocomposites for nonlinear optical

and optical gain applications, *Adv. Mat.* **15**(7–8), 610–613 (April 2003).
37. S. Musikhin, L. Bakueva, E. H. Sargent, and A. Shik, Luminescent properties and electronic structure of conjugated polymer-dielectric nanocrystal composites, *J. Appl. Phys.* **91**(10), 6679–6683 (May 2002).
38. L. Bakueva, S. Musikhin, M. A. Hines, T.-W. F. Chang, M. Tzolov, G. D. Scholes, and E. H. Sargent, Size-tunable infrared (1000–1600 nm) electroluminescence from PbS quantum-dot nanocrystals in a semiconducting polymer, *Appl. Phys. Lett.* **82**(17), 2895–2897 (April 2003).
39. C. A. Leatherdale, C. R. Kagan, N. Y. Morgan, S. A. Empedocles, M. A. Kastner, and M. G. Bawendi, Photoconductivity in CdSe quantum dot solids, *Phys. Rev. B* **62**(4), 2669–2680 (July 2000).
40. M. Pientka, V. Dyakonov, D. Meissner, A. Rogach, D. Talapin, H. Weller, L. Lutsen, and D. Vanderzande, Photoinduced charge transfer in composites of conjugated polymers and semiconductor nanocrystals, *Nanotechnolgy* **15**, 163–170 (Nov. 2004).
41. I. Visoly-Fisher, S. R. Cohen, D. Cahen, and C. S. Ferekides, Electronically active layers and interfaces in polycrystalline devices: Cross-section mapping of CdS/CdTe solar cells, *Appl. Phys. Lett.* **83**(24), 4924–4926 (Dec. 2003).
42. M. Chikamatsu, T. Taima, Y. Yoshida, K. Saito, and K. Yase, Mg-doped C_{60} thin film as improved n-type organic semiconductor for a solar cell, *Appl. Phys. Lett.* **85**(1), 127–129 (Jan. 2004).
43. M. Drndić, R. Markov, M. V. Jarosz, M. G. Bawendi, and M. A. Kastner, Imaging the charge transport in arrays of CdSe nanocrystals, *Appl. Phys. Lett* **83**(19), 4008–4010 (Nov. 2003).
44. G. H. Buh, H. J. Chung, C. K. Kim, J. H. Ye, I. T. Yoon, and Y. Kuk, Imaging of a silicon pn junction under applied bias with scanning capacitance microscopy and Kelvin probe force microscopy, *Appl. Phys. Lett.* **77**, 106–108 (2000).
45. M. Hammar, E. R. Messmer, M. Luzuy, S. Anand, S. Lourdudoss, and G. Landgren, Topography dependent doping distribution in selectively re-grown inp studied by scanning capacitance microscopy, *Appl. Phys. Lett.* **72**, 815–817 (1998).
46. J. F. Marchiando, J. J. Kopanski, and J. Albers, Limitations of the calibration curve method for determining dopant profiles from scanning capacitance micrscope measurements, *J. Vac. Sci. Technol. B* **18**, 414–417 (2000).
47. G. L. Pearson, W. T. Read, and W. Shockley, Probing the space-charge layer in a p-n junction, *Phys. Rev.* **85**(6), 1055–1057 (1952).
48. D. Ban, E. H. Sargent, St. J. Dixon-Warren, I. Calder, A. J. SpringThorpe, R. Dworschak, G. Este, and J. K. White, Direct imaging of the depletion region of an InP pn junction under bias using scanning voltage microscopy, *Appl. Phys. Lett.* **81**(26), 5057–5059 (Dec. 2002).
49. S. B. Kuntze, E. H. Sargent, J. K. White, K. Hinzer, S. Dixon-Warren, and D. Ban, *In Situ* resistance measurement of the p-type contact in InP–InGaAsP coolerless ridge waveguide lasers, *Appl. Phys. Lett.* **86**, 081111 (Feb. 2005).
50. C. Kittel, *Introduction to Solid State Physics.* John Wiley & Sons, Inc., 1996.
51. N. W. Ashcroft and N. D. Mermin, *Solid State Physics.* Thomson Learning, Inc., Stamford, Connecticut, 1976.
52. B. G. Streetman and S. Banerjee, *Solid State Electronic Devices*, 5th ed. Prentice-Hall Inc., New Jersey, 2000.
53. C. Kittel and H. Kroemer, *Thermal Physics*, 2nd ed. W. H. Freeman and Company, San Francisco, 1980.
54. J. Manifacier, Y. Moreau, H. K. Henisch, and G. Rieder, Response of potential probes to nonequilibrium situations, *J. Appl. Phys.* **56**(2), 387–395 (July 1984).
55. J. W. Mayer, O. J. Marsh, R. Baron, R. Kikuchi, and J. M. Richardson, Interpretation of potential-probe measurements in two-carrier structures, *Phys. Rev.* **137**(1A), A295–A301 (Jan. 1965).
56. S. B. Kuntze, E. H. Sargent, St. J. Dixon-Warren, J. K. White, K. Hinzer, and D. Ban, Nanoscopic electric potential probing: Influence of probe sample interface on spatial resolution, *Appl. Phys. Lett.* **84**(4), 601–603 (Jan. 2004).
57. P. De Wolf, T. Clarysse, and W. Vandervorst, Quantification of nanospread-ing resistance profiling data, *J. Vac. Sci. Technol. B* **16**(1), 320–326 (Jan./Feb. 1998).
58. D. Álvarez, J. Hartwich, M. Fouchier, P. Eyben, and W. Vandervorst, Sub-5-nm-spatial resolution in scanning spreading resistance microscopy using full-diamond tips, *Appl. Phys. Lett.* **82**(11), 1724–1726 (March 2003).
59. J. K. White, C. Blaauw, P. Firth, and P. Aukland, 85 degree C investigation of uncooled 10 Gb/s directly modulated InGaAsP RWG GC-DFB lasers, *IEEE Photon. Technol. Lett.* **13**, 773–775 (2001).
60. M. Maiorov, R. Menna, A. Komissarov, D. Garbuzov, and J. Connolly, High power InGaAsP/InP broad-waveguide single-mode ridge-waveguide lasers, *Optical Fiber Comm. Conf. and Exhibit Technical Digest*, 2001.
61. J. Singh, I. D. Henning, P. S. Mudhar, M. A. Fisher, S. Perrin, D. A. H. Mace, and M. J. Adams, A novel twin-ridge-waveguide optical amplifier switch, *IEEE Photon. Technol. Lett.* **4**, 173–176 (1992).
62. J. D. Evans, G. J. Letal, G. P. Li, and J. G. Simmons, The contribution of lateral current spreading to the temperature sensitivity of strained-layer, multiple-quantum-well, long wavelength, ridge waveguide lasers, *Lasers and Electro-Optics Soc. Ann. Meeting*, 1995.
63. L. Kuna, F. Uherek, J. Kovac, J. Jakabovic, V. Gottshalch, and B. Rheinlander, Ridge-waveguide InAs/GaAs lasers, *Third International EuroConference on Adv. Semicond. Devices and Microsystems*, 2000.
64. S. Y. Hu, S. W. Corzine, K.-K. Law, D. B. Young, A. C. Gossard, L. A. Coldren, and J. L. Merz, Lateral carrier diffusion and surface recombination in InGaAs/AlGaAs quantum-well ridge-waveguide lasers, *J. Appl. Phys.* **76**, 4479–4487 (1994).
65. M. Achtenhagen and A. Hardy, Lateral current spreading in ridge waveguide laser diodes, *Appl. Phys. Lett*. **74**, 1364–1366 (1999).
66. M. Legge, G. Bacher, S. Bader, A. Forchel, H.-J. Lugauer, A. Waag, and G. Landwehr, Strongly-index-guided II–VI laser diodes, *IEEE Photon. Technol. Lett*. **12**, 236–238 (2000).
67. M. Aoki, M. Komori, T. Tsuchiya, H. Sato, K. Nakahara, and K. Uomi, Inp-based reversed-mesa ridge-waveguide structure for high-performance long-wavelength laser diodes, *IEEE J. Select. Topics Quantum Electron.* **3**, 672–683 (1997).
68. S. Y. Hu, D. B. Young, A. C. Gossard, and L. A. Coldren, The effects of lateral leakage current on the experimental gain/current-density curve in quantum-well ridge waveguide lasers, *IEEE J. Quantum Electron.* **30**, 2245–2250 (1994).

69. G. H. B. Thompson, *Physics of Semiconductor Laser Devices.* John Wiley & Sons Inc., Chichester, 1980.
70. A. V. Harton and C. G. Fonstad, Implantation of Li^+ and Na^+ into PbTeSe for current confinement in PbTeSe/PbSnTe ridge waveguide lasers, *J. Appl. Phys.* **72**, 2575–2578 (1992).
71. G. J. Letal, J. G. Simmons, J. D. Evans, and G. P. Li, Determination of active-region leakage currents in ridge-waveguide strained-layer quantum-well lasers by varying the ridge width, *IEEE J. Quantum Electron.* **34**, 512–518 (1998).
72. D. Ban, E. H. Sargent, K. Hinzer, St. J. Dixon-Warren, A. J. Spring Thorpe, and J. K. White, Direct observation of lateral current spreading in ridge waveguide lasers using scanning voltage microscopy, *Appl. Phys. Lett.* **82**(23), 4166–4168 (June 2003).
73. Z. J. Wang, S. J. Chua, F. Zhou, X. J. Wang, W. Wang, and R. H. Wu, Native-oxidized InAlAs blocking layer buried heterostructure InGaAsP–InP MQW laser for high-temperature operation, *IEEE Photon. Technol. Lett.* **11**, 3–5 (1999).
74. H. S. Cho, D. H. Jang, J. K. Lee, K. H. Park, J. S. Kim, S. W. Lee, H. M. Kimand, and H. M. Park, High-performance strain-compensated multiple quantum well planar buried heterostructure laser diodes with low leakage current, *Japan. J. Appl. Phys.* **35**, 1751–1757 (1996).
75. D. Ban, E. H. Sargent, S. Dixon-Warren, G. Letal, K. Hinzer, J. K. White, and G. Knight, Scanning voltage microscopy on buried heterostructure multiquantum-well lasers: Identification of a diode current leakage path, *IEEE J. Quantum Electron.* **40**(2), 118–122 (Feb. 2004).
76. H. Yamazaki, T. Anan, K. Kudo, S. Sugou, and T. Sasaki, Planar-buried-heterostructure laser diodes with oxidized AlAs insulating current blocking, *IEEE J. Select. Topics Quantum Electron.* **5**, 688–693 (1999).
77. J. Matukas, V. Palenskis, C. Pavasaris, E. Sermuksnis, and J. Vysniauskas, Optical and electrical characteristics of InGaAsP MQW BH DFB laser diodes, *Mater. Sci. Forum* **384–385**, 91–94 (2002).
78. T. Makino, J. D. Evans, and G. Mak, Maximum output power and maximum operating temperature of quantum well lasers, *Appl. Phys. Lett.* **71**, 2871–2873 (1997).
79. S. Smetona, B. B. Elenkrig, and J. G. Simmons, Maximum operating temperature of the 1.3 μm strained layer multiple quantum well InGaAsP lasers, *J. Appl. Phys.* **84**, 4076–4078 (1997).
80. B. B. Elenkrig, S. Smetona, J. G. Simmons, T. Makino, and J. D. Evans, Maximum operating power of 1.3 μm strained layer multiple quantum well InGaAsP lasers, *J. Appl. Phys.* **85**, 2367–2370 (1999).
81. B. B. Elenkrig, S. Smetona, J. G. Simmons, B. Takasaki, J. D. Evans, and T. Makino, Series resistance and its effect on the maximum output power of 1.5 μm strained-layer multiple-quantum-well ridge waveguide InGaAsP lasers, *J. Appl. Phys.* **87**, 1–4 (2000).
82. D. Ban, E. H. Sargent, St. J. Dixon-Warren, K. Hinzer, A. J. SpringThorpe, R. Streater, G. Knight, and J. K. White, Scanning voltage microscopy on active semiconductor lasers: The impact of doping profile near an epitaxial growth interface on series resistance, *IEEE J. Quantum Electron.* **40**(6), 651–655 (June 2004).
83. A. A. Grinberg, Thermionic-tunneling-diffusion model of the laser current-voltage and power characteristics, *J. Appl. Phys.* **75**(12), 7669–7680 (June 1994).
84. J. Piprek, P. Abraham, and J. E. Bowers, Self-consistent analysis of high-temperature effects on strained-layer multiquantum-well InGaAsP–InP lasers, *IEEE J. Quantum Electron.* **36**(3), 366–374 (March 2000).
85. J. Piprek, J. K. White, and A. J. SpringThorpe, What limits the maximum output power of long-wavelength AlGalnAs/InP laser diodes? *IEEE J. Quantum Electron.* **38**(9), 1253–1259 (Sep. 2002).
86. D. A. Neamen, *Semiconductor Physics and Devices: Basic Principles*, 3rd ed. McGraw-Hill, Inc., New York, 2003.
87. P. W. Leech and G. K. Reeves, Effect of layer structure on the electrical properties of contacts to p-type $In_{0.53}Ga_{0.47}As$/InP, *Thin Solid Films* **298**, 9–13 (1997).
88. R. Dutta, M. A. Shahid, and P. J. Sakach, Graded band-gap ohmic contacts to n- and p-type InP, *J. Appl. Phys.* **69**(7), 3968–3974 (April 1991).
89. G. Stareev, H. Künzel, and G. Dortmann, A controllable mechanism of forming extremely low-resistance nonalloyed ohmic contacts to group III–V compound semiconductors, *J. Appl. Phys.* **74**(12), 7344–7356 (Dec. 1993).
90. G. Stareev, H. Künzel, and G. Dortmann, Erratum: 'A controllable mechanism of forming extremely low-resistance nonalloyed ohmic contacts to group III–V compound semiconductors' [*J. Appl. Phys.* **74**, 7344 (1993)], *J. Appl. Phys.,* **75**(12), 8246 (June 1994).
91. M.-H. Park, L. C. Wang, J. Y. Cheng, and C. J. Palmstrom, Low resistance ohmic contact scheme ($\sim\ \mu\Omega$ cm^2) to p-InP, *Appl. Phys. Lett.* **701**, 99–101 (Jan. 1997).
92. A. G. Baca, F. Ren, J. C. Zolper, R. D. Briggs, and S. J. Pearton, A survey of ohmic contacts to III–V compound semiconductors, *Thin Solid Films* **308–309**, 599–606 (1997).
93. J. G. Wasserbauer, J. E. Bowers, M. J. Hafich, P. Silvestre, L. M. Woods, and G. Y. Robinson, Specific contact resistivity of InGaAs/InP p-isotype heterojunctions, *Electron. Lett.* **28**(17), 1568–1569 (Aug. 1992).
94. P. W. Leech, G. K. Reeves, and M. H. Kibel, Pd/Zn/Pd/Au ohmic contacts to p-type $In_{0.53}$ $Ga_{0.47}As$/InP, *J. Appl. Phys.* **76**(8), 4713–4718 (Oct. 1994).
95. S. Richter, M. Geva, J. P. Garno, and R. N. Kleiman, Metal–insulator–semiconductor tunneling microscope: Two-dimensional dopant profiling of semiconductors with conducting atomic force microscopy, *Appl. Phys. Lett.* **77**(3), 456–458 (July 2000).
96. M. Levinshtein, S. Rumyantsev, and M. Shur, Eds., *Handbook Series on Semiconductor Parameters.* World Scientific, New Jersey, 1996.
97. R. E. Thomas and A. J. Rosa, Eds., *The Analysis and Design of Linear Circuits.* Prentice-Hall Inc., New Jersey, 1998.
98. S. B. Kuntze, D. Ban, and E. H. Sargent, Parasitic photocurrent causes scanning voltage microscopy artifacts, submitted.
99. N. Tessler and G. Eisenstein, On carrier injection and gain dynamics in quantum well lasers, *IEEE J. Quantum Electron.* **29**, 1586–1595 (1993).
100. D. Ban and E. H. Sargent, Influence of nonuniform carrier distribution on the polarization dependence of modal gain in multi-quantum-well lasers and semiconductor optical amplifiers, *IEEE J. Quantum Electron.* **36**, 1081–1088 (2000).

101. I. M. P. Aarts and E. H. Sargent, Above-threshold leakage in semiconductor lasers: An analytical physical model, *IEEE J. Quantum Electron.* **36**, 496–501 (2000).
102. M. J. Hamp, D. T. Cassidy, B. J. Robinson, Q. C. Zhao, and D. A. Thompson, Nonuniform carrier distribution in asymmetric multiple-quantum-well ingaasp laser structures with different numbers of quantum wells, *Appl. Phys. Lett.* **74**, 744–746 (1999).
103. R. Nagarajan and J. E. Bowers, Effects of carrier transport on injection efficiency and wavelength chirping in quantum-well lasers, *IEEE J. Quantum Electron.* **29**, 1601–1608 (1993).
104. R. Campi, S. Marcinkevicius, and G. Landgren, Studies on the carrier transport in InGaAlAsP–InGaAsP quantum well structures emitting at 1.3 μm, *IEEE Conf. on Lasers and Electro-Optics Europe*, 2000.
105. F. Alsina, P. V. Santos, R. Hey, A. Garcia-Cristobal, and A. Cantarero, Dynamic carrier distribution in quantum wells modulated by surface acoustic waves, *Phys. Rev. B* **64**, 041304 (2001).
106. A. Grabmaier, M. Scholthaler, A. Hangleiter, C. K. M. Blez, and A. Ougazzaden, Carrier transport limited bandwidth of 1.55 μm quantum-well lasers, *Appl. Phys. Lett.* **62**, 52–54 (1993).
107. R. Nagarajan, R. P. Mirin, T. E. Reynolds, and J. E. Bowers, Experimental evidence for hole transport limited intensity modulation response in quantum well lasers, *EL* **29**, 1688–1690 (1993).
108. D. Ban, E. H. Sargent, and S. Dixon-Warren, Scanning differential spreading resistance microscopy on actively driven buried heterostructure multiquantum-well lasers, *IEEE J. Quantum Electron.* **40**(7), 865–870 (July 2004).
109. G. L. Belenky, R. F. Kazrinov, J. Lopata, S. Luryi, T. Tanbun-Ek, and P. A. Garbinski, Direct measurement of the carrier leakage out of the active region in InGaAsP/InP laser heterostructures, *IEEE Trans. Electron Dev.* **42**, 215–218 (1995).
110. J. A. L. Holmes, R. P. Mirin, Y. J. Chiu, S. P. Denbaars, and J. E. Bowers, 1.55 μm in-plane lasers with p-AlGaAs cladding layers, *Proc. IEEE Lasers and Electro-Optics Soc.*, 1997.
111. S. M. Sze, *Physics of Semiconductor Devices.* John Wiley & Sons, Inc., New York, 1981.
112. M. J. Romero, D. Araujo, and R. Garcia, Sch laser recombination rate from ebic profiles, *Mater. Sci. Eng. B* **42**, 172–175 (1996).
113. R. F. Kazarinov and M. R. Pinto, Carrier transport in laser heterostruc-tures, *IEEE J. Quantum Electron.* **30**, 49–53 (1994).
114. B. O. Dabbousi, M. G. Bawendi, O. Onitsuka, and M. F. Rubner, Electroluminescence from CdSe quantum-dot/polymer composites, *Appl. Phys. Lett*. **66**(11), 1316–1318 (March 1995).
115. M. A. Hines and P. Guyot-Sionnest, Synthesis and characterization of strongly luminescing ZnS-capped CdSe nanocrystals, *J. Phys. Chem.* **100**, 468–471 (1996).
116. T. W. F. Chang, S. Musikhin, L. Bakueva, L. Levina, M. A. Hines, P. W. Cyr, and E. H. Sargent, Efficient of excitation transfer from polymer to nanocrystals, *Applied Physics Letters* **84**(21), 4295–4297 (May 2004).
117. D. M. Basko, V. M. Agranovich, F. Bassani, and G. C. La Rocca, Energy transfer from a semiconductor quantum dot to an organic matrix, *Eur. Phys. J. B* **13**, 653–659 (2000).
118. A. Engelmann, V. I. Yudson, and P. Reineker, Enhanced optical nonlinearity of hybrid excitons in an organic semiconducting quantum dot covered by an organic layer, *Phys. Rev. B* **57**(3), 1784–1790 (Jan. 1998).
119. L. Bakueva, S. Musikhin, E. H. Sargent, H. E. Ruda, and A. Shik, *Luminescence and Photovoltaic Effects in Polymer-Based Nanocomposites.* American Scientific Publishers, 2003, ch. 5: Nanocomposites.
120. L. Bakueva, S. Musikhin, E. H. Sargent, and S. Schulz, Fabrication and investigation of nanocomposites of conducting polymers and GaSb nanocrystals, *Surf. Sci.* **532–535**, 828–831 (June 2003).
121. N. C. Greenham, X. Peng, and A. P. Alivisatos, Charge separation and transport in conjugated-polymer/semiconductor-nanocrystal composites studied by photoluminescence quenching and photoconductivity, *Phys. Rev. B* **54**(24), 17628–17637 (Dec. 1996).
122. N. C. Greenham and R. H. Friend, Semiconductor device physics of conjugated polymers, in *Solid State Physics* H. Ehrenreich and F. Spaepen, Eds. Academic, San Diego, 1995.
123. J. J. M. Halls, C. A. Walsh, N. C. Greenham, E. A. Marseglia, R. H. Friend, S. C. Moratti, and A. B. Holmes, Efficienct photodiodes from interpenetrating polymer networks, *Nature* **376**, 498–500 (1995).
124. E. K. Miller, K. Lee, K. Hasharoni, J. C. Hummelen, F. Wudl, and A. J. Heeger, Photo-induced changes in the complex index of refraction in conjugated polymer/fullerene blends, *J. Chem. Phys.* **108**, 1390–1394, 1998.
125. Y. Lin, J. Zhang, L. Brozowski, E. H. Sargent, and E. Kumacheva, Nonlinear optical figures of merit of processible composite of poly(2-methoxy,5-(2′-ethyl)hexyloxy)-p-phenylene vinylene) and poly(methyl methacrylate), *J. Appl. Phys.* **91**, 522–524 (2002).
126. A. Gil, P. J. de Pablo, J. Colchero, J. Gómez-Herrero, and A. M. Baró, Electrostatic scanning force microscopy images of long molecules: Single-walled carbon nanotubes and DNA, *Nanotechnolgy* **13**, 309–313 (2002).
127. T. W. Ebbesen, H. J. Lezec, H. Hiura, J. W. Bennett, H. F. Ghaemi, and T. Thio, Electrical conductivity of individual carbon nanotubes, *Nature* **382**, 54–56 (1996).
128. B. I. Kim, U. H. Pi, Z. G. Khim, and S. Yoon, Lithography by tapping-mode atomic force microscopy with electrostatic force modulation, *Appl. Phys. A* **66**, S95–S98 (1998).
129. A. V. Ankudinov, E. Y. Kotel'nikov, A. A. Kantsel'son, V. P. Evtikhiev, and A. N. Titkov, Cross-sectional electrostatic force microscopy of semiconductor lasers, *Semicond.* **35**(7), 874–880 (2001).